ADVANCED MATERIALS
www.advmat.de

Photocatalytic Z-Scheme Overall Water Splitting: Recent Advances in Theory and Experiments

Jamal Abdul Nasir, Akhtar Munir, Naveed Ahmad, Tanveer ul Haq, Zaibunisa Khan, and Ziaur Rehman**

Photocatalytic water splitting is considered one of the most important and appealing approaches for the production of green H_2 to address the global energy demand. The utmost possible form of artificial photosynthesis is a two-step photoexcitation known as "Z-scheme", which mimics the natural photosystem. This process solely relies on the effective coupling and suitable band positions of semiconductors (SCs) and redox mediators for the purpose to catalyze the surface chemical reactions and significantly deter the backward reaction. In recent years, the Z-scheme strategies and their key role have been studied progressively through experimental approaches. In addition, theoretical studies based on density functional theory have provided detailed insight into the mechanistic aspects of some breathtakingly complex problems associated with hydrogen evolution reaction and oxygen evolution reaction. In this context, this critical review gives an overview of the fundamentals of Z-scheme photocatalysis, including both theoretical and experimental advancements in the field of photocatalytic water splitting, and suggests future perspectives.

1. Introduction

Solar light-assisted water splitting into hydrogen (H_2) and oxygen (O_2) using SC is one of the most promising means to address the critical energy and environmental problems.[1,2] Being environmentally benign, water splitting is considered an eye-catching process to convert and store abundant solar energy in the form of chemical species.[3–5] The overall water splitting can be achieved using SC while providing a photon of energy greater than the bandgap energy of the SC. Furthermore, it is suggested that the bottom of the conduction band (CB) edge of the SC should be more negative than the reduction potential of H^+/H_2 (–0.41 V vs NHE at pH 7) whereas the top of the valence band (VB) should be more positive than the oxidation potential of H_2O/O_2 (0.82 V vs NHE at pH 7).[6,7] In one-step photoexcitation, most SCs are unable to carry out the overall water splitting reaction[8] due to the shortfall of some of the notable requirements such as an appropriate bandgap (less than 3 eV), suitable band edge positions, and stability of the photocatalysts.[9,10] Although, a few metal oxides and chalcogenides (e.g., WO_3, CdS) have been extensively investigated as one-step photocatalysts, however, less stability and low solar-to-hydrogen conversion efficiency (STH) decline their widespread application.[6,11]

To mitigate forgoing issues, two-step photoexcitation achieved by the combination of two dissimilar SCs in series with staggered band alignment following either type-II or Z-scheme photocatalytic mechanism[12] can be employed. In type II, the electrons migrate from the higher CB photocatalyst I (PC I) to the lower CB photocatalyst II (PC II), and the holes flow in a reverse manner between the two SCs.[13] In contrast, the Z-scheme catalytic system describes the spatial distribution of charges, thus, improving the strong redox ability of the two

J. Abdul Nasir, Z. Khan, Z. Rehman
Kathleen Lonsdale Materials Chemistry
Department of Chemistry
University College London
20 Gordon Street, London WC1H 0AJ, UK
E-mail: jamal.nasir.18@ucl.ac.uk; r.ur@ucl.ac.uk

J. Abdul Nasir, Z. Rehman
Department of Chemistry
Quaid-i-Azam University
Islamabad 45320, Pakistan
E-mail: zrehman@qau.edu.pk

A. Munir
Department of Chemistry
University of Sialkot
1 Km, main Daska road, Sialkot, Punjab 51310, Pakistan

The ORCID identification number(s) for the author(s) of this article can be found under https://doi.org/10.1002/adma.202105195.

DOI: 10.1002/adma.202105195

A. Munir
Department of Chemistry & Chemical Engineering
SBA School of Science & Engineering
Lahore University of Management Sciences (LUMS)
DHA
Lahore 54792, Pakistan

N. Ahmad
Institute of Pharmaceutical Science
Faculty of Life Science and Medicine
King's College London
150 Stamford Street, London SE1 9NH, UK

N. Ahmad
University of Swat. Charbagh
Swat, Khyber Pakhtunkhwa, Pakistan

T. u. Haq
Sustainable Energy Engineering
Frank H. Dotterweich College of Engineering
Texas A&M University
Kingsville, TX 78363-8202, USA

SCs.[14] In the Z-scheme pathway, the strong reduction capability of CB electrons of PC I and the strong oxidation capability of VB holes of PC II are preserved whereas the electrons with low reduction ability in the CB of PC II and holes with low oxidation ability in the VB of PC I pair up.[15] To establish such heterojunction, two SCs with staggered band alignments are rationally selected. A typical Z-scheme mimics natural photosynthesis and can be broadly categorized into two types. In the first type, the two SCs do not necessarily need real contact and thereby need an electron shuttle mediator such as Fe^{2+}/Fe^{3+} and I^-/IO_3^- for the smooth transfer of electrons.[16] The second type is a mediator-free system composed of strong coupling of two SCs, hence, called direct Z-scheme.[17] These modules, in either case, are promising approaches to address the associated challenges with the photocatalytic system for water splitting.[15,18,19]

To deeply understand the chemistry, efficiency, and current status of this next-generation technology, it is direly needed to bring the recent facets in theory and experiments. Particularly, modeling techniques have shown considerable progress[20] in the exploration of band offset prediction, interface charge carrier flow, and mechanistic insights. The computational methodologies, in particular, are indispensable aids to predict the charge transfer and reaction mechanisms. Even though a plethora of review articles have been recently published on Z-scheme photocatalysis,[3,8,21–23] especially on the construction of the Z-scheme photocatalytic system [24] and their multi-scale applications; however, to the best of our knowledge, a comprehensive and all-inclusive review article to present Z-scheme, from the perspective of both theoretical and experimental advancements, has not been reported so far. In this review, the readers are referred to various topical textbooks and reference works along with summarized tables. As the field is very extensive, the review is necessarily selective to critically highlight the particular advancements in experimental and theoretical areas.

The review is structured as follows: First, a comprehensive overview of the fundamental insights of Z-scheme photocatalysis and the current status of the experimental efforts to unfold the Z-scheme developments for water splitting is presented followed by critical remarks to highlight the possible gaps and future development in the field. Second, an overview of modeling and computational techniques is comprehensively discussed, followed by critical comments to highlight the limitation of DFT, in particular, the generalized gradient approximation (GGA) and local density approximation (LDA)-based simulations, which are used for excited-state properties. Finally, an outlook and future perspective is provided to understand the current status and need/room to further modernize the Z-scheme module.

2. Two-Step Photoexcitation: Fundamentals, Insights, and Developments in Z-Scheme

So far, two main approaches have been established for photocatalytic overall water splitting: the first method involves using a single-component photocatalyst, called one-step photoexcitation.[9] To achieve overall water splitting, single-component photocatalysts should have a suitable band-edges position for both HER and OER, sufficiently small bandgap, as well as enough driven forces to ensure the proper separation of electron–hole pairs.[25] Although, these aspects are mutually exclusive and necessary, however, it is very difficult to meet such a stringent criterion, which drastically reduces the ability of a single-component based water splitting system.[26] Taking into account the limitations of single-component photocatalytic systems, in-depth research ventures have been dedicated over the years to customize photocatalyst architectures. As a result, heterojunction-type photocatalytic devices were designed, which increases the lifespan of photogenerated charge carriers.[27] Although type-II heterojunction can promote significant charge separation, however, the reduction capability of the CB electron is greatly compromised owing to the transfer of electrons toward relatively less negative CB.

To mitigate these constraints, the second module, known as the Z-scheme has been developed, which employs an anisotropic configuration of two photocatalysts to enhance the performance of water splitting.[3] Unlike type-II heterojunction, Z-scheme allows a specific flow of charge carriers due to the inclusion of a remarkable electron-relaying channel. For example, when the VB electrons of both PS I and PS II get excited to CBs upon photoexcitation, the photogenerated electrons in PS II can be readily transported either through an electron mediator or through Ohmic contact to re-pair it with the holes from PS I VB.[28] This unusual form of vectorial charge transfer (Z-pattern) permits electrons and holes to coexist in two different photocatalysts while maintaining strong redox properties for OER at PS II and HER at PS I. Furthermore, in comparison to one-step photocatalysts and type-II heterojunction (two-step), Z-scheme requires a lower change in Gibbs free energy to drive the photoreaction.[29]

The concept of two light reactions, the "holy grail" for photocatalysis, was initially introduced by Karl Herzfeld and James Franck in 1941.[30] Later on, the two pigment and two light reactions systems were described and explained in 1945 by Eugene Rabinowitch who hypothesized that one light undergoes oxidation reaction and another undergoes reduction reaction.[31] The breakthrough of experimental research on oxidation and reduction of cytochrome by two different wavelengths of light[32] was then followed by the work of many others. Since Rabinowitch's ground-breaking debate on two light processes and two pigment systems on James Frank's comment in 1945, great interests have been flourished to imitate the natural photosynthetic process.[33] For the first time, Bard introduced the concept of the Z-scheme photocatalytic model in 1979 using an electron mediator to transfer the charges between two photosystems.[3,34]

The first key illustration of the photocatalytic Z-scheme model was presented in 2001 when the I^-/IO_3^- shuttle redox pair was introduced as an ionic mediator to regulate the transfer of charge between the two SCs[35] marking the introduction of the first-generation Z-scheme with ionic redox pairs. However, the redox pair-aided Z-scheme process has some unavoidable disadvantages, such as backward reaction caused by the ionic mediator which imposes a heavy competition for the forward-redox reaction.[36] In addition, the redox pairs absorb light irradiations that significantly reduce the efficiency of photocatalysts.[21] With this perspective, a solid-state Z-scheme was introduced in 2006 using Au as an electron mediator, which opened a new horizon for the investigators. The key characteristic of this system is the low-resistance transfer of electrons (with the linear current–voltage curve) via strong ohmic contact.[1] Furthermore, the ingenious configuration of the all-solid-state Z-scheme approach using conductor as a mediator makes a more auspicious capacity for electron relaying. This offers an inter-particle transfer of electrons that could significantly

trim down the electron transfer from PS II to PS I.[4] The use of rare and expensive metals significantly restricts the practical usage of such a system. To replace these noble metals, the use of several promising conducting materials, that is, graphene, carbon nanotubes, and quantum dots as electron mediators are worth considering.[8,37] To this end, the range of mediators could theoretically be extended to a wider field. Wang et al. in 2009 reported that the directional electron transfer can be established in ZnO and CdS.[38] In a solid–solid interface system, a third generation known as direct Z-scheme provides a powerful medium to generate an internal electric field.[36] In addition, Sasaki et al. have expanded the definition of the PS-PS method by assembling $SrTiO_3$:Rh (PS I) and $BiVO_4$ (PS II) using pH modification.[14] The creation of the internal electric field at the solid–solid contact interface, however, depends heavily on the nature of the SCs (**Figure 1**).

Recently, a scalable Z-scheme photocatalytic sheet system gives potential scalability to increase solar water splitting.[39] Unlike the predecessor, the design of Z-scheme in the form of thin film composed of dual-layer particulate sheets with a top layer photocatalyst lying on an underlying electron mediator provides an opportunity to further expand the principle of the Z-scheme device. The photocatalyst sheets provide a promising electron transport pathway between PS I and PS II via Ohmic interaction using the underlying conductor layer.[4] In contrast to the traditional powder system, such configuration of Z-scheme using photocatalyst sheets can mitigate the effect of H^+ and OH^-concentration, overpotentials, and pH gradient, which in turn improve the Ohmic contact between PS I and PS II.[37] Based upon the above efforts and challenges, remarkable efforts and investigations have been devoted to the development of the new light-harvesting system to fully utilize solar light irradiations using this next-generation Z-scheme technology.[2,40]

3. Experimental Advances in Z-Scheme Water Splitting

The use of particulate photocatalysts is considered imperative for future practical applications of water splitting due to the focal advantages, including simplicity and cost-effectiveness. As discussed earlier, two-step photoexcitation requires the SCs that satisfy the band position criteria either for HER or OER. Therefore, such types of materials usually reduce the thermodynamic requirements and thus expand the choice of SCs, particularly toward narrow bandgap materials.

Integrated devices that couple oxygen evolution catalysts (OEC) with light-harvesting SC is an appealing technology to facilitate the direct solar to fuel production processes. However, due to the sluggish kinetics and high thermodynamic requirements, additional overpotential is being provided to proceed with the OER process. In this system, the function of OEC is to collect the holes from the SC, promote charge separation, and facilitate water oxidation by lowering the activation energy. Certain reports highlight in situ generations and self-assembling of OEC on the light absorber, even in highly acidic media.[43] On the other hand, various photocatalysts emerge as potential contenders for HER.[6,44] For instance, 2D metal oxides and chalcogenides are widely considered as hydrogen evolution catalysts (HEC).[6,23,45] To date, various types of visible-light-responsive photocatalysts have been tested in the Z-scheme strategy both in the presence and absence of redox mediators;[46–48] the experimental developments in this quest are discussed in detail in this section.

3.1. Effect of Redox Mediator

Redox shuttle mediator is the most essential component of Z-scheme water splitting which plays a key role in the transfer of electrons from OER to HER photocatalyst. The chemical and electronic behavior of the redox mediator has a significant effect on the Z-scheme water splitting process along with some other surface interactions of the catalytic part or cocatalyst. Among many, IO_3^-/I^- and Fe^{3+}/Fe^{2+} are the most commonly employed redox couple[49–52] (**Table 1**).

The activity of the Z-scheme is highly reliant on the pH of the reaction medium. In the case of Fe^{3+}/Fe^{2+}, the precipitation of Fe ions gives $Fe(OH)_x$ in both acidic and neutral conditions. However, in the presence of IO_3^-/I^- couple, the reaction

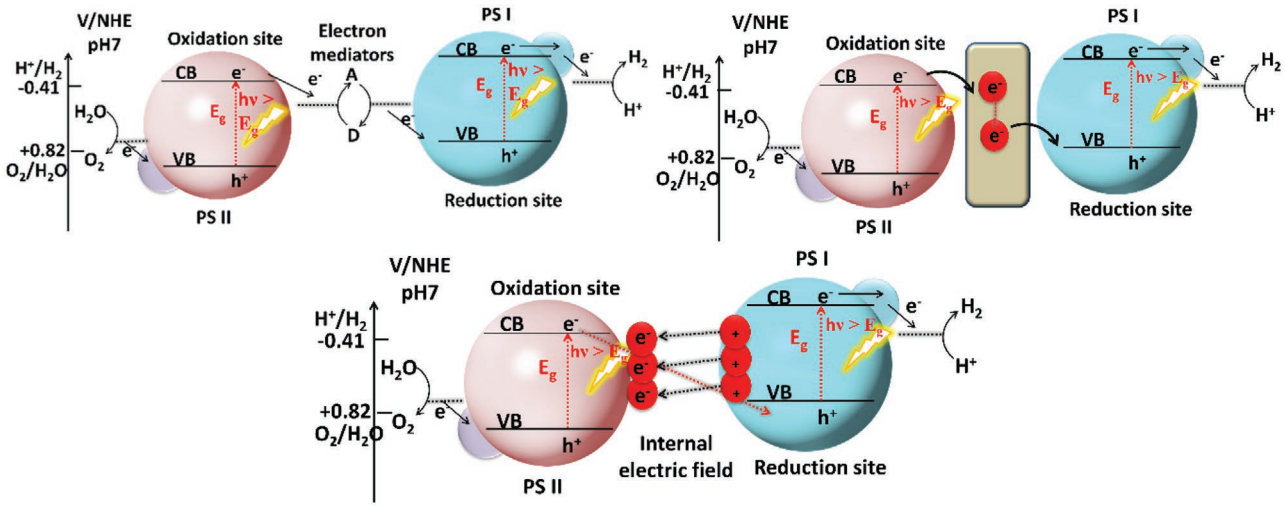

Figure 1. The schematic illustration of the band energy diagram of a) PS-A/D-PS Z-scheme system, b) PS-C-PS Z-scheme system, and c) PS-PS or direct Z-scheme system.[1,34,39,41,42]

Table 1. A representative list of some selective redox mediator-based Z-scheme systems for photocatalytic water splitting.

HEP	OEP	Mediators	pH	Efficiency/Activity	Ref.
$SrTiO_3$:Cr,Ta	WO_3	IO_3^-/I^-	7	AQY = 0.1% (λ = 420 nm)	[59]
TaON	WO_3	IO_3^-/I^-	7	AQY = 0.4% (λ = 420 nm)	[60]
TaON	RuO_2/TaON	IO_3^-/I^-	6	H_2: 2.8 μmol h^{-1}; O_2: 1.4 μmol h^{-1} (λ = 420 nm)	[61]
$HCa_2Nb_3O_{10}$ nanosheets	PtOx/H–Cs–WO_3	IO_3^-/I^-	4	H_2: 137.3 μmol/5h; O_2:72.9 μmol/5h, AQY: 2.4% (λ = 420 nm)	[62]
Pt-loaded $BaTaO_2N$	WO_3	IO_3^-/I^-	n/a	AQY:6.8%, STH: 0.24% (λ = 420 nm)	[63]
$ATaO_2N$ (A = Ca,Ba)	WO_3	IO_3^-/I^-	without control	AQY = 0.1% (λ = 420 nm)	[58]
ZrO_2/TaON	WO_3	IO_3^-/I^-	5.4	AQY = 6.3% (λ = 420 nm)	[51]
ZrO_2/TaON	Ir/TiO_2(rutile)/Ta_3N_5	IO_3^-/I^-	n/a	O_2: 34 μmol h^{-1} (λ = 420 nm)	[64]
ZrO_2/TaON	RuO_2/TaON	IO_3^-/I^-	n/a	H_2: 8 μmol h^{-1}; O_2: 3.6 μmol h^{-1} (λ = 420 nm)	[51]
$BaZrO_3$–$BaTaO_2N$	PtOx/WO_3	IO_3^-/I^-	n/a	H_2: 22.4 μmol h^{-1}; O_2: 9.4 μmol h^{-1} visible light irradiation	[50]
Pt/$Sm_2Ti_2S_2O_5$	TiO_2(rutile)	IO_3^-/I^-	11	H_2: 6 μmol h^{-1}; O_2: 3 μmol h^{-1} (λ > 300 nm)	[65]
$SrTiO_3$:Cr,Ta	PtOx/H-Cs-WO_3	IO_3^-/I^-	4	AQY = 1.5% (λ = 420 nm)	[66]
TiO_2(anatase):Cr,Ta	TiO_2(rutile):Cr,Ta	IO_3^-/I^-	without control	H_2: 0.38 μmol; O_2: 0.19 μmol for 180 h (λ = 420 nm)	[67]
NKX2677-adsorbed Pt/$H_4Nb_6O_{17}$	IrO_2/Pt/WO_3	IO_3^-/I^-	4.5	H_2: 2.6 μmol h^{-1}; O_2: 1.3 μmol h^{-1} (λ > 420 nm)	[68]
MK2-adsorbed Pt/$H_4Nb_6O_{17}$	IrO_2/Pt/WO_3	IO_3^-/I^-	4.5	H_2: 1.6 μmol h^{-1}; O_2: 0.6 μmol h^{-1} (λ > 410 nm)	[69]
g-C_3N_4	WO_3	IO_3^-/I^-	8.3	H_2: 2.1 μmol h^{-1}; O_2: 1.1 μmol h^{-1} (λ > 395 nm)	[70]
$MgTa_2O_6yNx$/TaON	PtOx/WO_3	IO_3^-/I^-	n/a	AQY = 6.8% (λ = 420 nm)	[71]
Ru/$SrTiO_3$:Rh	RuO_2/TiO_2:Ta,N	IO_3^-/I^-	n/a	H_2: 1.3 μmol h^{-1}; O_2: 0.5 μmol h^{-1} (λ > 420 nm)	[72]
$SrTiO_3$:Rh	$BiVO_4$	Fe^{3+}/Fe^{2+}	2.4	AQY = 0.3% (λ = 440 nm)	[73]
$SrTiO_3$:Rh	Bi_2MoO_6	Fe^{3+}/Fe^{2+}	2.4	AQY = 0.2% (λ = 440 nm)	[73]
$SrTiO_3$:Rh	WO_3	Fe^{3+}/Fe^{2+}	2.4	AQY = 0.2% (λ = 440 nm)	[73]
Ru/$SrTiO_3$:Rh	$BiVO_4$	Fe^{3+}/Fe^{2+}	2.4	STH = 0.02%	[74]
Au/$SrTiO_3$:Rh	WO_3	Fe^{3+}/Fe^{2+}	2.4	H_2: 140 μmol; O_2: 71 μmol for 22 h (λ > 420 nm)	[74]
Ru/$SrTiO_3$:Rh	WO_3	Fe^{3+}/Fe^{2+}	2.4	H_2: 416 μmol; O_2: 197 μmol for 22 h (λ > 420 nm)	[74]
Ru/$SrTiO_3$:Rh	$BiVO_4$	Fe^{3+}/Fe^{2+}	2.4	AQY = 4.2% (λ = 420 nm)	[75]
Ru/$SrTiO_3$:Rh	IrOx/$SrTiO_3$:Rh,Sb	Fe^{3+}/Fe^{2+}	2.4	H_2: 3 μmol h^{-1}; O_2: 1.4 μmol h^{-1} (λ > 420 nm)	[76]

Table 1. Continued.

HEP	OEP	Mediators	pH	Efficiency/Activity	Ref.
Pt/g-C_3N_4	$BiVO_4$	Fe^{3+}/Fe^{2+}	3	H_2: 0.6 μmol h^{-1}; O_2: 0.3 μmol h^{-1} ($\lambda > 395$ nm)	[70]
Ru/$SrTiO_3$:Rh	H_2WO_4	Fe^{3+}/Fe^{2+}	2.3	H_2: 4.7 μmol h^{-1}; O_2: 2.2 μmol h^{-1} ($\lambda > 400$ nm)	[77]
Ru/$SrTiO_3$:Rh	Bi_4NbO_8Cl	Fe^{3+}/Fe^{2+}	2.4	H_2: 12.4 μmol h^{-1}; O_2: 6.3 μmol h^{-1} ($\lambda > 400$ nm)	[78]
g-C_3N_4	$BiVO_4$	Fe^{2+}/Fe^{3+}	n/a	H_2: 81.6 μmol·h^{-1}; O_2: 40.4 μmol·h^{-1}, AQY: 1.8% (λ = 420 nm)	[79]
Ru/$SrTiO_3$:Rh	S-doped g-C_3N_4	$[Co(bpy)_3]^{3+/2+}$	pH = 7	H_2: 24.6 μmol h^{-1}; O_2: 24.6 μmol h^{-1}	[80]
$HCa_2Nb_3O_{10}$ nanosheets	PtO_x/H–Cs–WO_3	IO_3^-/I^-	4	H_2: 137.3 μmol/5h; O_2:72.9 μmol/5h, AQY: 2.4% (λ = 420 nm)	[62]
g-C_3N_4	C-TiO_2	Au	n/a	H_2: 129.0 mmol $g^{-1}h^{-1}$	[81]
CdS	g-C_3N_4	rGO	n/a	H_2: 676.5 mmol $g^{-1}h^{-1}$, AQE:36.5%	[82]
g-C_3N_4	Perylene diamide polymer (PDIP)	rGO	n/a	H_2: 15.8 μmol h^{-1}; O_2: 7.8 μmolg^{-1} h^{-1}, AQE: 4.94% (λ = 420 nm)	[83]

can be run in a wide range of pH (Equations (1) and (2)). It is believed that the side products produced during the reaction (due to the photooxidation of I^-) are also dependent on the pH of a reactionmedium.[52]

$$I^- + H_2O + 6h^+ \rightarrow IO_3^- + 6H^+ \quad (1)$$

$$3I^- + 2h^+ \rightarrow I_3^- \quad (2)$$

The I_3^- produced in the reaction (Equation (2)) does not act as a good electron acceptor in many reactions even if catalyzed by PtO_x/WO_3 and Rutile TiO_2, and hence, there is a need for a high pH value (for Equation (1)) to proceed with the reaction. However, the disproportion reaction takes place, which can also convert I_3^- to I^- and IO_3^- (Equation (3)).

$$3I_3^- + 3H_2O \rightarrow 8I^- + IO_3^- + 6H^+ \quad (3)$$

This disproportional reaction is more convenient at high pH which is evident from a significant enhancement in the activity with increasing the pH of the reaction medium when IO_3^-/I^- redox couple is employed. In addition, the pH-dependent activity affects the photocatalytic performance of catalysts in a basic medium as illustrated in the photo-driven one-step excitation water splitting.[53] For instance, WO_3 is unstable in the basic medium but shows high stability in acidic conditions (below pH 7.37). The pH-dependent activities of the Z-scheme system using Pt/anatase TiO_2 and rutile-TiO_2 for HER and OER, respectively, in 0.1 M NaI are shown in **Figure 2**a. The concentration of NaI is plotted against the water splitting rate to give a volcano-type plot for the Z-scheme system;[51,52,54] similar behavior is observed for the Fe^{3+}/Fe^{2+}[3] which, however, needs further investigation. A negligible production of O_2 was observed at pH 3 for rutile TiO_2. Although a considerable increase in the O_2 production was observed at a higher pH (9), however, a significant mismatch in the quantity of O_2 and H_2 was observed which might be due to the accumulation of I_3^- in the solution. Such accumulation may also adversely affect the activity by absorbing radiation around 350 nm. Further increase in the pH caused a significant increase in the stochiometric production rate of H_2 and O_2, suggesting that basic media favors efficient water splitting. By increasing the concentration of I^-, the efficiency of H_2 production can be improved; however, it decreases O_2 production due to the hole-induced oxidation of I^- on the OER side of the photocatalyst.

Recently, the dual pairs of redox mediators such as Bi^{3+}/Bi^{5+} and I_3^-/I^- are also employed to enhance charge separation by making an interfacial intimate coupling with the energy bands of the SCs.[56] As a result, the majority of the holes are scavenged leaving the electrons to be effectively utilized for the HER. Apart from the extensive use of IO_3^-/I^- and Fe^{3+}/Fe^{2+} couples, Sayama et al. studied Z-scheme water splitting in the presence of Pt-TiO_2 using NO_3^-/NO_2^- as a redox mediator. The H_2 was evolved on Pt-TiO_2 and O_2 evolution occurred through photoexcitation of NO_3^- as shown in Figure 2b.[55] Under light irradiations (below 260 nm), photoexcitation of NO_3^- occurred to generate NO_3^{-*} species followed by its decomposition to O_2 and NO_2^- and some intermediate species such as $ONOO^-$. In addition, Co^{3+}/Co^{2+} as a redox pair has also been employed to boost the water-splitting reaction; for example, $[Co(bpy)_3]^{3+/2+}$ and $[Co(phen)_3]^{3+/2+}$ (bpy = 2,2′-bipyridine; phen = 1,10-phenanthroline) mediator impressively facilitate the electron transfer from $BiVO_4$ to Ru/$SrTiO_3$:Rh (AQY of 2.1% at 420 nm).[57] The intimate interfacial contact with well-matched bands of SCs is one of the key criteria for the selection of redox mediators. A well-matched synchronization between mediators and energy bands of SCs via in-built redox mediations facilitates the charge separation. For instance, Amit et al. employed I_3^-/I^- and Bi^{3+}/Bi^{5+} as redox couples, which were not only capable to capture the electrons from the CB of $Bi_4Ti_3O_{12}$ ($C_3N_4/Bi_4Ti_3O_{12}/Bi_4O_5I_2$

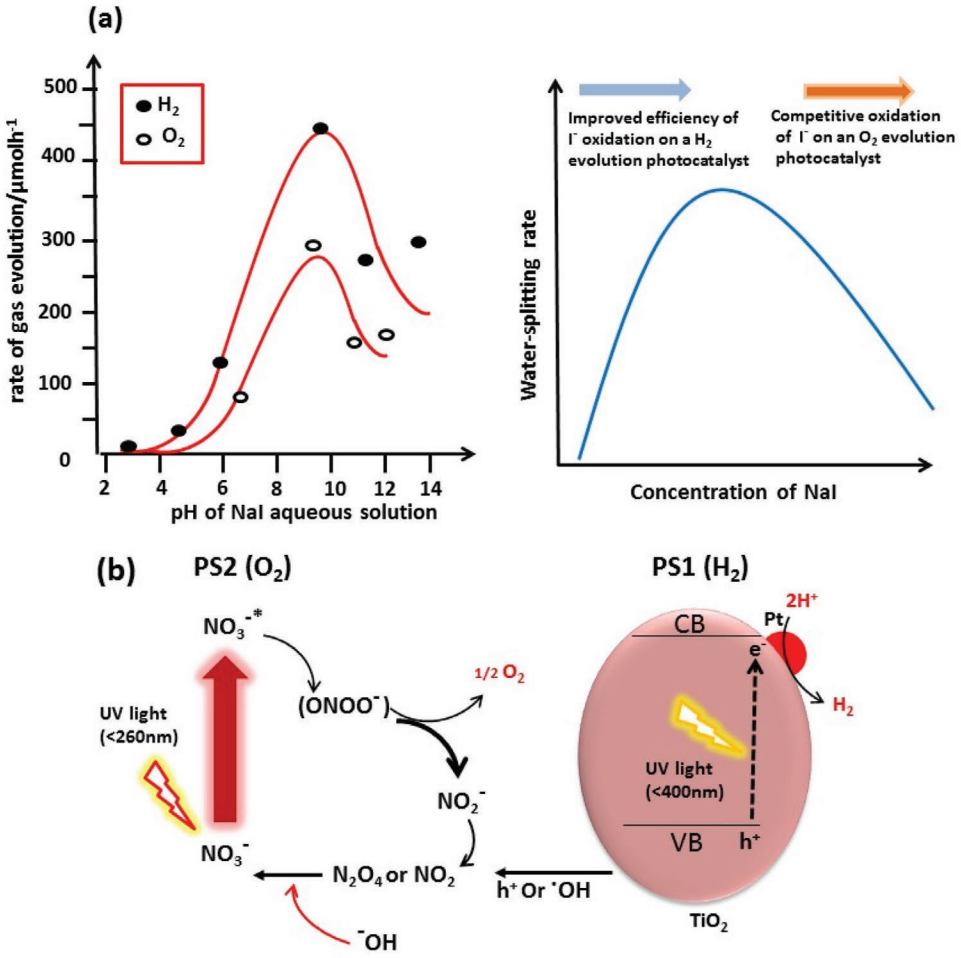

Figure 2. a) The Effect of pH on H_2 and O_2 production rate, and the activity and concentration correlation curve. Reproduced with permission.[53] Copyright 2011, Elsevier and b) schematic mechanism for water splitting over Pt/TiO_2 in suspended aqueous $NaNO_2$. Reproduced with permission.[55] Copyright 2006, Elsevier.

heterojunction) but also partially scavenge holes from the VB to hinder the charge recombination owing to the suitable matching between energy bands of the SCs and redox potentials of mediators.[56] Furthermore, the choice of the redox couple is mainly measured on how/to which extent it can deter the backward reaction and charge recombination. The backward reaction is a typical shortcoming in the 1st generation of the Z-scheme. For instance, Fe^{2+} and Fe^{3+} species compete with the water oxidation and reduction reactions, respectively, which undergo thermodynamically feasible backward reactions resulting in lowering the overall efficiency of the Z-scheme.[38] Therefore, redox mediators should be selected while taking into consideration the aforementioned issues. In addition, the pH of the reaction media has a profound effect on the Z-scheme performance, since the band edges potentials of the photocatalysts strongly depend on the pH of the media, while the redox potentials of a mediator such as $[Co(bpy)_3]^{3+/2+}$ is not susceptible to the pH.[58] However, the relative effect does matter meaning that the potential of the redox mediators is dependent on the band edges of the SCs which is in turn affected by the change in pH of the media.

3.1.1. Redox Mediator Free Z-Scheme

Although the redox mediator is a major player in the Z-scheme water splitting module, however, undesirable backward reactions, indirect pH dependency, and the shielding effect are the associated problems, which adversely affect the light absorption capacity of the photocatalysts.[8,36,51,59,84] For example, IO_3^-/I^- redox pair promotes the backward reactions due to the oxidation of I^- by photogenerated holes in the OEC,[18] thus demanding the deployment of a redox mediator free Z-scheme system. This idea, indeed, is the realization of photocatalysts that have in-built electric fields at the interface of p and n-type of SCs. In 2009, Kudo et al. developed an appealing Z-scheme module comprising $Ru/SrTiO_3$:Rh photocatalyst for HER and a wide-ranging OER photocatalyst (TiO_2:Cr/Sb, $BiVO_4$, and WO_3).[41] Such arrangement follows the Z-scheme pathway, where pH adjustment is very vital. In acidic media, the incorporation of $BiVO_4$ particles to $Ru/SrTiO_3$:Rh provides effective contact for the charge transfer through aggregation (**Figure 3**). Under light irradiations, the electron and holes are readily generated in the CB and VB of both $SrTiO_3$:Rh and $BiVO_4$, respectively. Due to

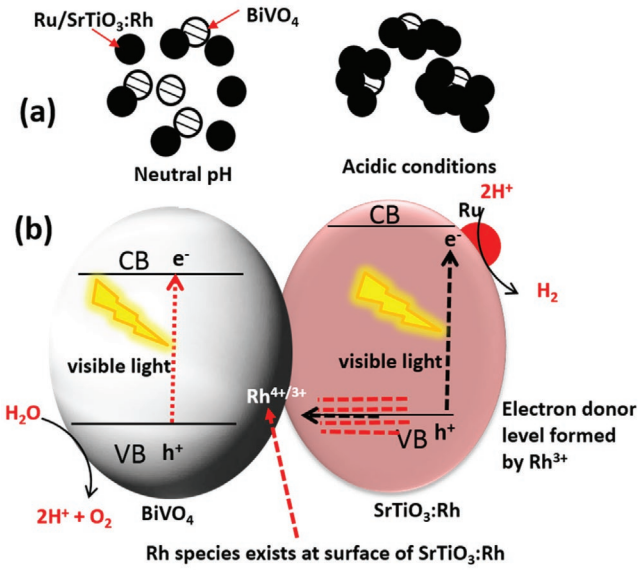

Figure 3. Schematic illustration of Z-scheme photocatalysis: a) suspension of $Ru/SrTiO_3$:Rh and $BiVO_4$ at neutral and acidic conditions and b) scheme of photocatalytic water splitting. Reproduced with permission.[41] Copyright 2009, American Chemical Society.

the intimate interaction, the electrons transfer from the CB of $BiVO_4$ to the impurity level of $SrTiO_3$:Rh, where the water is reduced to H_2, while in the VB of $BiVO_4$, the water is oxidized to O_2 thus accomplishing overall water splitting. It was found that this system, devoid of the redox mediator, can efficiently catalyze visible light-assisted water splitting, where the activity was found highly sensitive to pH, maximum activity at pH 3. From the photoluminescence data and catalytic performance, it was perceived that the transfer of electrons from the CB of water oxidation photocatalyst to an impurity level occurs via reversible oxidation of Rh (Rh^{4+}/Rh^{3+}) especially in the forbidden region of $SrTiO_3$. Based upon this approach, the overall and persistent water splitting was achieved via two-step photoexcitation with AQY of 1.7% at 420 nm and STH of 0.12%.[29] The interparticle electron transfer is the rate-determining step that can be improved by establishing strong contact between the SCs. In another study, Ta_3N_5 with CoO_x and Ir was successfully used as a mediator-free Z-scheme photocatalytic system.[85]

In a recent report, $Ru/SrTiO_3$:Rh and $BiVO_4$ catalytic system was used for water splitting in the presence of surface-reduced graphene oxide (rGO) as solid-state electron mediator.[47] From the experimental results, it was deduced that extent of graphene oxide (GO) reduction and its hydrophobicity is the main reason behind the efficient transfer of electrons. In this particular case, the $BiVO_4$ induced rGO exhibits high electronic conduction ability and low hydrophobicity thereby enhancing the catalytic process. Given the aforementioned strategies, some important direct Z-scheme-based photocatalysts are listed in **Table 2** to present an overview of some important developments in the area.

3.2. Oxy-Nitride-Based Z-Scheme

The use of oxynitrides in water splitting was first introduced in 2008[2,61] after establishing the fact that unmodified Ta-oxynitride (TaON) is unable to produce O_2 in the presence of IO_3^-; loading of either RuO_2 or IrO_2 afforded significant O_2 production. Since then, a plethora of work has been done using oxynitride material as H_2/O_2 photocatalysts in Z-scheme.[2,61] For the efficient photocatalytic system, many efforts have been made including a variety of advanced and doped materials such as various combinations of doped $SrTiO_2$ for HER and WO_3, $BiVO_3$, etc., for OER.[48,52,59] However, these materials have several limitations to be utilized in the Z-scheme including the development of the acceptor level in the forbidden band region for light-harvesting and slower migration of electron/hole pairs to the surface and bulk of the materials. These problems are originated from the discrete energy levels provided by the dopant materials.[100] The materials which have been considered as a benchmark for such a system consisting of doped-TiO_3 (e.g., $SrTiO_3$:Cr/Ta and $SrTiO_3$:Rh) which can be used for an efficient HER.[52,73] Therefore, it is necessary to address the associated challenges with the previously reported catalytic system based on the doped materials.

In comparison with the metal oxides-based photocatalytic system, metal (oxy)-nitrides were initially reported for one-step photocatalytic water splitting; since then, their inherent potential for the Z-scheme approach was realized owing to the suitable band edge position available for the redox processes.[101] The band structure of $NaTiO_3$ and oxynitride is ($BaTaO_2N$) illustrated in **Figure 4**. The O 2p orbital is available on the top of the VB of the oxides. However, after adding N (as a substituent of O), the top position is shifted toward the higher side without disturbing the minima of the VB due to the high potential of N than O. This reshuffling of position has been confirmed through the DFT study. Consequently, the bandgap of the oxynitride becomes smaller (3 eV) and shows a better response to visible light.

3.2.1. Ta-Oxynitride

TaON is an accomplished visible-light-driven photocatalyst ($\lambda < 520$ nm) to catalyze the redox reaction (HER and OER) of water splitting when coupled with a suitable electron donor and acceptor. In 2005, Abe et al. worked Pt-TaON and Pt–WO_3 catalyst as HER and OER, respectively, in an aqueous medium using NaI electron acceptor.[60] Although, the rate of H_2 evolution declined during the long-lasting process owing to the unwanted reduction of IO_3^- by photogenerated electrons, however, no evolution of O_2 and N_2 was observed which validated that photogenerated holes in the TaON effectively oxidized I^- to IO_3^-. More promisingly, these results are in accordance with previous reports using TaON as electrode materials for photoelectrochemical water splitting.[102] The same Pt-loaded TaON and PtO_x/WO_3 can also catalyze the stoichiometric water splitting (same amount of H_2 and O_2 production) using a redox mediator (I^-/IO_3^-) with AQY of 0.5% at 420 nm. From the stability point of view, it was perceived that stoichiometric water splitting was maintained for 60 h at pH 5. The efficiency of such nitride can be further improved by varying the composition and doping impurities, which are discussed in the next section.

Some recent developments using TaON in Z-scheme were introduced which contributed significant advances in the

Table 2. A representative list of some selective direct Z-scheme systems for photocatalytic water splitting.

HEP	OEP	pH	Efficiency/Activity	Ref.
$Mn_{0.25}Cd_{0.75}S$	WO_3	6.8	H_2: 1.05 mmol $h^{-1}g^{-1}$, AQE: 14.02% (λ = 470 nm)	[86]
ZnO	Cu_2O-CuO	n/a	H_2: 1092.5 μmol$g^{-1}h^{-1}$, AQY: 3%	[87]
Fe_2O_3	g-C_3N_4	n/a	H_2: 398.0 mmol $h^{-1}g^{-1}$ (λ = 420 nm)	[87]
$BiVO_4$	$BiVO_4$	n/a	H_2: 15.6 mmol h^{-1}; O_2: 7.3 mmol h^{-1}, AQE ¼ 6.4% (λ = 420 nm)	[88]
g-C_3N_4	Bi_4NbO_8Cl	n/a	H_2: 287.7 mmol g^{-1} h^{-1} AQY ¼ 2.02%, (λ = 420 nm)	[89]
MnO_2	Monolayer g-C_3N_4	n/a	H_2:60.6 mmol $h^{-1}g^{-1}$; O_2: 28.9 mmol $h^{-1}g^{-1}$ AQE: 23.33% (λ = 420 nm)	[90]
Ru/$SrTiO_3$:Rh	$BiVO_4$	3.5	AQE: 1.7% (λ = 420 nm)	[41]
Pt/CdS	ZnO	n/a	H_2:774 μmol h^{-1} (λ = 387 nm)	[91]
Ru/$SrTiO_3$:Rh	Ir/CoO*x*/Ta_3N_5	3.9	H_2:23 μmol h^{-1}; O_2:12 μmol h^{-1} (λ = 420 nm)	[85]
g-C_3N_4	WO_3	n/a	AQE: 0.9% (λ = 405 nm)	[92]
Rutile TiO_2	Anatase TiO_2	n/a	H_2:324 μmol h^{-1} (λ < 405 nm)	[93]
g-C_3N_4	C,N-TiO_2	n/a	H_2:3.918 μmol h^{-1} (λ > 420 nm)	[94]
Pt/Bi_2S_3	$Bi_2O_{2.33}$	n/a	H_2:62.61 μmol h^{-1}	[95]
Black P	Red P	n/a	H_2:0.66 μmol h^{-1}	[96]
$Zn0_{.67}Cd_{0.33}S$	ZnO	n/a	H_2:973 μmol h^{-1}	[97]
Pt/g-C_3N_4	$W_{18}O_{49}$	n/a	H_2:429.85 μmol h^{-1} AQY: 39.1% (λ = 420 nm)	[98]
$Zn0_{.2}Cd_{0.8}S$	ZnO_{1-x}	n/a	H_2:2.518 mmol h^{-1} (λ > 420 nm)	[99]

field.[103] For example, a molecular-based noble metal-free system comprising $CuGaO_2$ dye-sensitized photocathode with a TaON|CoO_x photoanode was used as a complete set-up for H_2/O_2 evolution employing the Z-scheme strategy. Very high Faradic efficiencies of 87% and 88% for H_2 and O_2, respectively, were achieved at pH 7. This led to an STH of 5.4×10^{-3}%, which is the highest efficiency for the reported system so far (**Figure 5**).[104] In this system, dye-sensitized transparent conducting oxides DS-TCO, a molecular dye (RBG-174), was used as photoelectrode that can absorb light and promote charge separation to accelerate the HER. Such molecular catalyst (CoHEC) can anchor with p-type NiO; however, enhanced activity was observed after replacing NiO with $CuGaO_2$ which opened a new window for a noble metal-free Z-scheme catalytic system.[105]

3.2.2. $ATaO_2N$ (A = Ca, Sr, and Ba)

For the effective utilization of light and efficient H_2 production, perovskite oxynitrides of ATaON (A = Ca, Sr, Ba) with absorption edge at 520, 600, and 660 nm, respectively, were evaluated as Z-scheme system for photocatalytic H_2 production.[107] These modified perovskites were observed with promoted water reduction ability in the aqueous medium in the presence of NaI electron acceptor. However, in the case of Sr, N_2 was also produced during catalysis due to the self-oxidation of oxynitride. After further investigation, it was deduced that overall water splitting can be carried out by using Pt/$CaTO_2N$ and Pt/$BaTO_2N$ for HER and PtO_x/WO_3 for OER while using I^-/IO_3^- as a redox couple. The AQY of 0.1% at 420–440 nm was observed for Ba-analogue, although the wavelength for the same sample

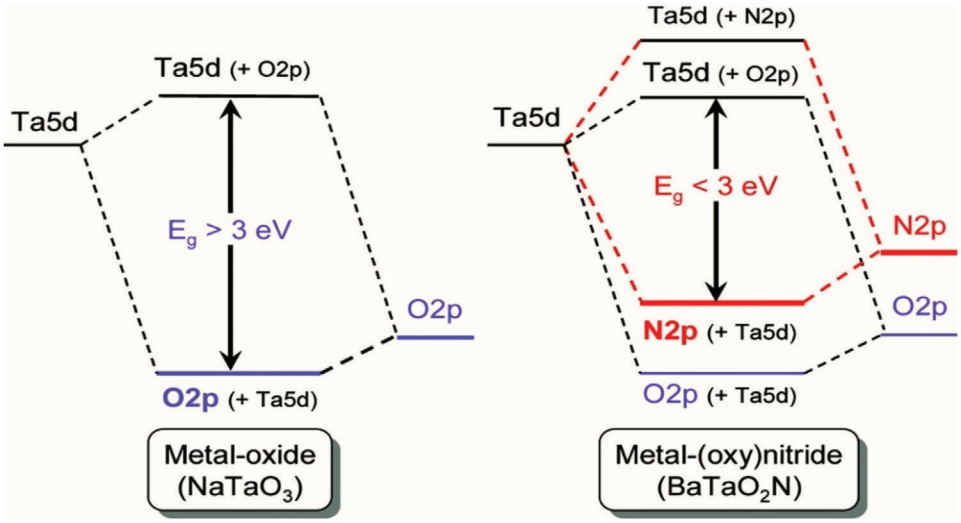

Figure 4. Schematic illustration of the band structure of metal oxide ($NaTaO_3$) and metal (oxy)nitride ($BaTaO_2N$). Reproduced with permission.[101] Copyright 2007, American Chemical Society.

was extended to 660 nm. However, a gradual decrease in the production of H_2/O_2 was observed that can be attributed to the accumulation of I_3^- in the solution during the long-term experiment which is not as efficient as IO_3^- for PtO_x/WO_3 due to its poor absorption properties.[58] The photogenerated electrons in the VB of PtO_x/WO_3 are not able to reduce I_3^-, thereby declining the O_2 production.

Although co-catalysts play a vital role in enhancing the activity of oxynitride photocatalysts, however, it also masks the surface of the catalysts, thereby blocking the light irradiations and forming aggregates that exhibit weak interaction with photocatalysts. However, enabling uniform dispersion and making intimate contact between cocatalyst and narrow band single-crystalline particulate photocatalysts can boost catalytic activity. For example, recently introduced single-crystalline particulate $BaTaO_2N$ decorated with Pt through impregnation method[63] followed by site-selective-photodeposition. This strategy enhances the performance of Pt-loaded $BaTaO_2N$ 100 times more than bare TaO_2N with an STH of 0.24% and AQY of 68% from aqueous methanol media and at 420 nm. To see the behavior of charge carriers affected by the structure of Pt nanoparticulate in $BaTaO_2N$, transient absorption spectroscopy was performed. As shown in **Figure 6**, the faster decay in the intensity curve for Pt decorated $BaTaO_2N$ at 5000 cm^{-1} (0.62 eV, 2000 nm) than the pure $BaTaO_2N$ indicated the fast charge transfer process from $BaTaO_2N$ to Pt.[108] Furthermore, the longer lifetime of photoexcited holes for Pt-$BaTaO_2N$ loaded via a two-step decoration shows a considerable reduction in electron–hole recombination.

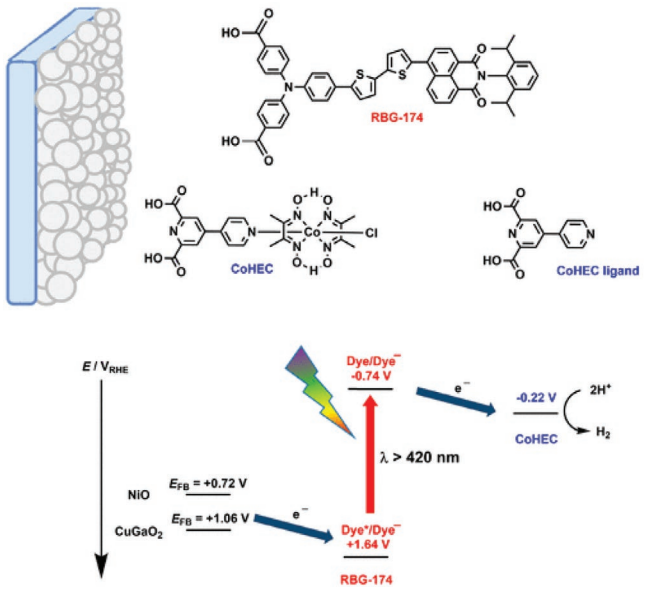

Figure 5. Photocathode illustration; the molecular structures and energy diagram. CoHEC redox potential is the onset of catalysis at pH 7. Electrochemical potentials are given versus RHE, flat band position of NiO corrected from V versus NHE (pH 7), and flat band position of $CuGaO_2$ corrected from V versus Ag/AgCl (pH 6.6).[104–106] Reproduced with permission.[104] Copyright 2019, American Chemical Society.

3.2.3. Surface Modification of Oxynitrides for HER

Surface modification is generally adopted to improve the properties and quality of the photocatalyst surface. Therefore, the presence of active sites on the surface and associated challenge with charge transport is deemed to modify the surface for improved performance.[53] As discussed in the previous section that TaON is the bottleneck contender for H_2 production. However, the overall water splitting is limited due to various factors including less thermal stability of the catalysts and the need for a post-calcination process. To overcome these problems, a novel method has been introduced to improve the surface defects by using ZrO_2 as a protector via the surface modification process.[109] Furthermore, it has been explored and observed for various oxynitrides (e.g., Ta_3N_5 and $CaTaO_2N$) that the reduction of Ta^{+5} to Ta^{+4} and Ta^{+3} in TaON leads to the generation of anionic species to balance the internal charge. Such defective generated sites (anions and cations) can promote the charge recombination process. However, the recombination process is low in the case of

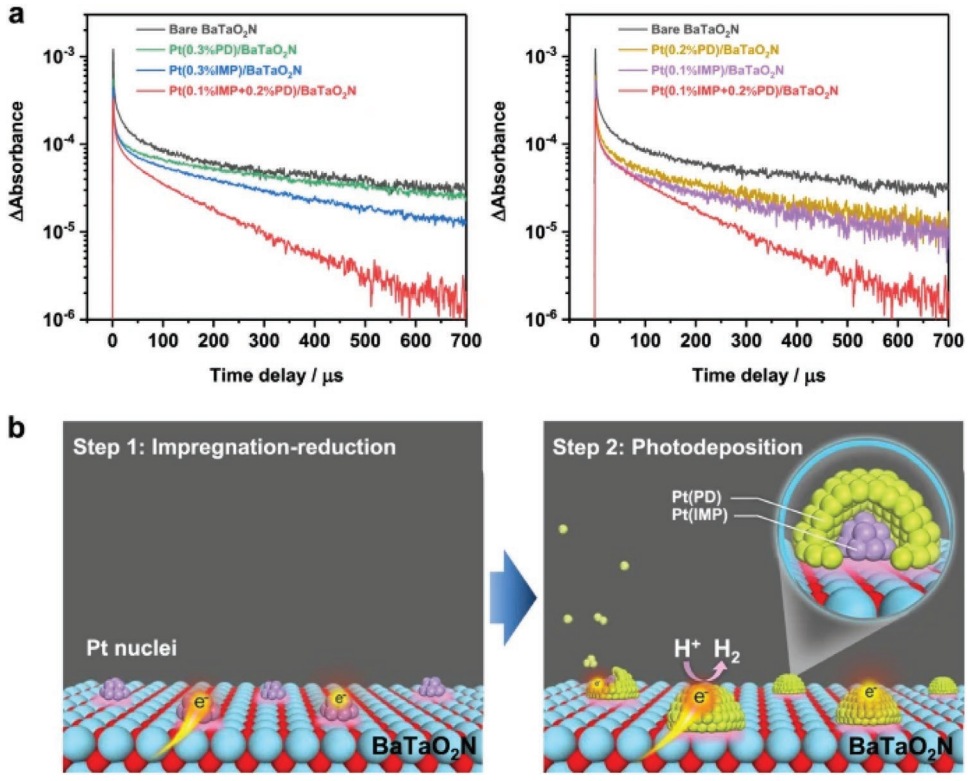

Figure 6. Interaction of Pt NPs and $BaTaO_2N$ (RbCl) photocatalyst. a) Transient absorption decays corresponding to electron dynamics in bare $BaTaO_2N$ and Pt-modified $BaTaO_2N$ photocatalysts probed at 5000 cm^{-1} (2000 nm, 0.62 eV) at 0–700 μs. b) Schematic illustration of sequential Pt cocatalyst deposition on $BaTaO_2N$. Reprinted with permission.[63] Copyright 2021, Springer Nature.

ZrO_2 which is more resistive than Ta_2O_5 in thermal ammoniacal treatment when loaded on the Ta_2O_5 surface. Consequently, the Ta^{+5} ions are assumed to interact with ZrO_2 at the interface of Ta_2O_5/TaON and ZrO_2 and hence become more cationic. In this way, the unwanted reduction of Ta^{+5} can be suppressed close to the surface of the material (**Figure 7**).

Nitridation of ZrO_2 and Ta_2O_5 and surface modification with ZrO_2 were done to suppress the unwanted reduction of Ta^{+5}. The ZrO_2-modified TaO (ZrO_2/TaON) was found to have enhanced performance in comparison with bear TaON. The performance was particularly more prominent when TaON was loaded with Pt coupled onto Pt_xO/WO_3 in the presence of

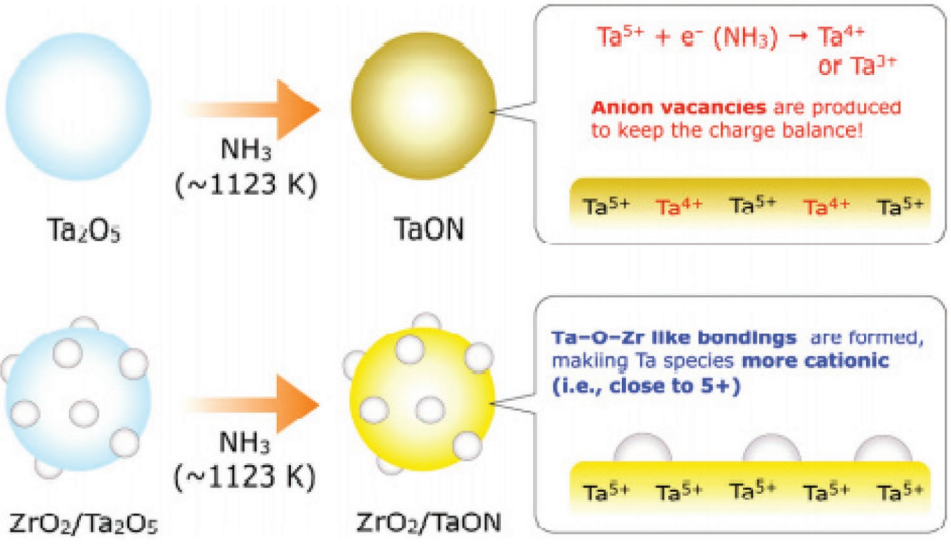

Figure 7. Synthetic protocol; ZrO_2/TaON synthesis through Nitridation of ZrO_2/Ta_2O_5, a method of reducing the creation of tantalum species (reduced) near the surface. Reproduced with permission.[109] Copyright 2008, The Chemical Society of Japan.

IO_3^-/I^- redox mediator in the visible light. The observed AQY of 6.3% (at 420 nm) is six times higher as compared to TaON.[51] This superior activity was attributed to the significant reduction in density of defective sites in ZrO_2/TaON that consequently minimizes the recombination process. This approach has been considered a promising strategy to tune the surface properties for the improved performance of TaON and alike materials.

3.3. Co-Catalyst Based Z-Scheme

The collection, separation, and transportation of photogenerated charge carriers to the active sites significantly decrease the chance of recombination and hence, the electron–hole pairs are secure. The purpose of a cocatalyst is to assist the photocatalyst rather than initiating the HER or OER.[110] It is generally believed that cocatalysts can enhance the H_2 activity by at least one order of magnitude. As discussed in the previous part, metal nanoparticles (NPs) as cocatalysts coupled with the catalytic system is one of the promising approaches to modify the surface properties and inherent capacity of materials for catalysis. In Z-scheme water splitting, the main objectives are extending the absorption range and the selectivity of the catalyst to competitively catalyze water oxidation and/-or reduction process.

Most recently, Murofushi et al. revealed the effect of FeOx, the first earth-abundant and non-noble metal cocatalyst on the Bi_4TaO_8Cl photocatalyst to assist the multielectron IO_3^- reduction process.[16] Based on the series of experimental examinations such as time-resolved spectroscopy, it is interpreted that O_2 evolution is enhanced through the facilitation of multielectron reduction of IO_3^- by FeOx. The redox capability of Fe (Fe^{3+}/Fe^{2+}) not only acts as a charge carrier capture from Bi_4TaO_8Cl but also promotes the reduction of the redox mediator.

It is often seen that the earlier oxidation and reduction of redox pairs occur prior to the reduction and oxidation of water on the catalytic part of the Z-scheme. Therefore, control over the selectivity of Z-scheme for the corresponding O_2/H_2 evolving processes is direly needed.[100] It is well established that the selectivity of catalysts is an inherent property of materials. Considering the selective water oxidation catalysts, for instance, rutile TiO_2 and WO_3 can catalyze the photocatalytic water oxidation even with Fe^{2+}, I^-, and alike electron donor species which, unfortunately, are more prone to oxidation than water under similar conditions. Although there are no solid reasons behind the selectivity of the above species, however, it can be suggested that the loading of NPs (co-catalyst) on the surface of light-harvesting materials can enhance the activity. Among these, RuO_2 can significantly boost the catalytic potential of TaON. In addition, Ru-loaded Pt/TaON can act as O_2 evolving catalysts, while in the presence of IO_3^-/I^- it acts as H_2 evolving catalysts.[61] More promisingly, this is the ever first report that consists of monoxide-type material to catalyze the overall water splitting process. It is noteworthy that TaON was not able to catalyze the oxidation of water alone in the presence of IO_3^-/I^-, most probably because of the efficient and excellent oxidation of I^-. However, after incorporating RuO_2, the water oxidation ability was significantly improved even in the presence of I^-. The role of RuO_2 was further investigated, particularly in the synthetic condition which is characterized by X-ray absorption spectroscopy (XAS) and SEM analysis.[111] During synthesis, the use of $(NH_4)_2RuCl_6$ as precursor under the optimal condition, the uniformly distributed RuO_2, was found to play as a dual cocatalyst for TaON to enhance the water oxidation and reduction of IO_3^-. However, from the experimental results, it has also been deduced that water oxidation of the Ru sensitized system is hampered due to the sidewise oxidation of I^- which is induced by the hole of VB of RuO_3/TaON. Meanwhile, the photo-assisted reduction of O_2 taking place on the surface of RuO_2/TaON also suppresses the catalytic performance. Similar to this concept, the Z-scheme efficiency was considerably improved by replacing Pt/TaON with Pt/ZrO_2/TaON.[112]

The prominent role of cocatalysts incorporated on photocatalyst is to offer an excess of active sites for catalysis and capture the electron/holes to minimize the recombination process.[29,53] Therefore, those cocatalysts which can participate in the multielectron reduction processes are much needed in Z-scheme water splitting. In particular, the cocatalysts which can catalyze the 2-electron water reduction process are essential in all kinds of the Z-scheme module. It is noteworthy to mention that the most suitable cocatalysts to show the best performance are highly dependent upon the electron donor species. As discussed already, the case of ZrO_2 NPs loaded TaON, which was employed as HEC in combination with PtO_3/TaON while OEC in the presence of IO_3^-/I^-. Among cocatalysts, better activity was observed for Pt-loaded ZrO_2/TaON.[51] Although, excellent performance was observed for Ru-loaded ZrO_2/TaON as OEC than Pt loaded ZrO_2/TaON in aqueous/methanol medium, however, less activity for the H_2 production than Pt analogous was observed using IO_3^-/I^-.[109,113] It is also important to mention that the effect size and shape of the co-catalyst can play a key role to ameliorate the catalytic performance. In the Pt-loaded ZrO_2/TaON Z-scheme module, it was revealed that the small size and uniform surface distribution of Pt NPs are primarily credible for the enhanced catalytic activity.[51] In the Z-scheme system, cocatalyst can facilitate the reduction of IO_3^- (6 electron process) that are necessary to perform the water oxidation process. However, rutile TiO_2 is an exceptional case that does not require any cocatalyst for the oxidation process in the presence of aqueous $NaIO_3$. The activity of RuO_2 loaded TaON is most probably due to the facilitation of IO_3^- reduction that in turn drives the water oxidation catalysis. By comparing the activity of RuO_2/TaON with IrO_2 loaded TaON, less activity was observed for the IrO_2/TaON under similar conditions.[61] Similarly, Ir-loaded Ta_3N_5 is another exciting example to efficiently catalyze water oxidation under visible light irradiations in the presence of IO_3^-.[64] From the electrochemical experiments, a little current has been observed for the reduction of IO_3^- on the surface of Ta_5N_5. However, a remarkable increase in the current for Ir-modified Ta_3N_5 was observed with the addition of IO_3^- (**Figure 8**). The high performance can be attributed to the enhanced reduction capability of IO_3^- after loading Ir NPs. Moreover, the bare Ta_3N_5 did not show any significant activity for H_2 production in the presence of aqueous/methanol solution; however, the H_2 production was markedly improved after loading Ir NPs indicating that cocatalyst can assist the multielectron reduction process in Z- scheme system.

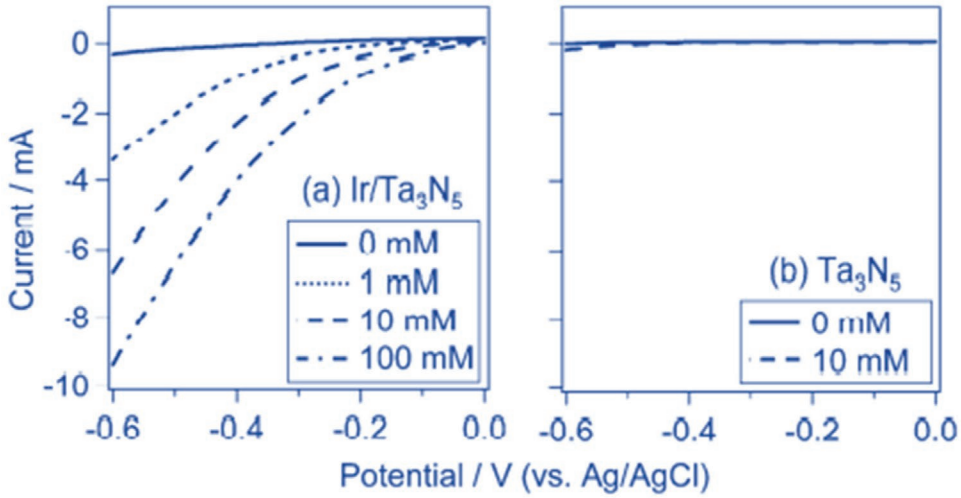

Figure 8. Comparison of currently produced from water splitting process by using Ta_3N_5 and Ir-Ta_3N_5 as electrode materials. Reproduced with permission.[64] Copyright 2010, American Chemical Society.

3.4. GO-Based Z-Scheme

The valance and conduction band of graphene comprising π bonding and π^* antibonding states, respectively, tap at the Brillouin zone corners, which endorsed the single sheet features with zero bandgaps. The intensive electronic band overlapping in graphene is due to the close carbon–carbon skeleton where holes and electrons act as mess-free charges. Incorporating heteroatoms or functionalities tunes graphene's electronic structure and elongates its application for the photochemical process. The physiochemical linkage of oxygen with graphene carbon makes a C-O covalent bond and eliminates the equivalence of the two carbon that distorts the actual orbital structure and orientations.[14] The introduction of these defects leads to the separation of π bonding and π^* antibonding orbitals and builds a bandgap in graphene. This bandgap can be further amplified by introducing more oxygen to the carbon skeleton that progressively shifts the valence band maximum (VBM) from graphene π bonding orbitals to the O 2p orbital while the π^* antibonding orbitals persist as conduction band minimum. rGO can be used as conducting support and as an electron mediator in the Z-scheme water splitting system.[114] Furthermore, it is more advantageous than the traditional redox couple (IO_3^- and Fe^{+2}/Fe^{+3}) owing to its easy recovery from the reaction medium and sufficient inherent electron delay properties during photocatalysis.

Recently Shi and his co-worker developed a ternary composite of rGO-Cu_2O/Bi_2WO_6 where rGO acts as a solid-state mediator that combines the photogenerated holes in Cu_2O and electrons in Bi_2WO_6 during the photochemical process.[115] It was experimentally observed that the HER photocatalytic activity of ternary composite is multifold higher than the simple Cu_2O/Bi_2WO_6. The solid-state Z-scheme due to rGO was responsible for the effectual desperation of holes and electrons pair.

Samal et al. developed various $AgPO_4$ composites with rGO via photo-induced reduction method by varying the amount of the rGO.[116] The photocatalytic activity was performed in the presence of 10 vol% aqueous-methanol solution under visible light (≥400 nm). The highest activity was found for rGO/$AgPO_4$ with an H_2 production rate of 3690 μmol h^{-1} g^{-1} which is 6.15 times greater than rGO. Based on the VB position of rGO (2.6 V, pH = 0), it was stated that the water reduction process is solely taking place on the rGO. Since electrons are excited in $AgPO_4$, migrated to the VB of rGO and then transferred to the CB of rGO for the reduction process. For further justification, the in situ Pt photoreduction (Pt^{+4} to Pt^0) experiment was carried under the same conditions. From the X-ray photoelectron spectroscopy (XPS) and TEM analysis, it was found that Pt NPs are reduced over the rGO sheets rather than the Ag-PO_4 surface. The photoreduction method developed for GO can be utilized for more advanced materials. Recently, Awase et al.[47] developed rGO-based new material via the photoreduction of rGO on $BiViO_4$ (rGO$BiVO_4$) and Ru/Sr/TiO_3:Rh (rGO/Ru/TiO_3:Rh) to improve the water-splitting ability owing to the high conductivity and electron mediating properties of rGO. From the experimental results, it was perceived that no H_2 and O_2 were observed when $BiVO_4$ and Ru/Sr/TiO_3:Rh were tested separately with and without a non-sacrificial reagent. However, by the combination of these two in the presence of rGO, a threefold time increase in the H_2/O_2 production was observed at pH 3.5. This increase in the activity can be attributed to the presence of an optimum amount of rGO that can capture electrons from the CB of $BiVO_4$ (OEC) and then transfer to the CB of Ru/Sr/TiO_3:Rh (HEC). This mechanism of electron transfer increases the charge separation in photocatalyst and keeps the holes in $BiVO_4$ and electrons in Ru/Sr/TiO_3: Rh and thus can convert the OEC to HEC.

As discussed in the previous section, OEC can be converted into HEC via the Z-scheme approach. Similarly, the HEC can also be modified for the overall water splitting process. For instance, metal sulfides are considered as HEC which may not be used for water oxidation due to the self-corrosion property. In this regard, the rGO was used as an electron mediator by coupling metal sulfides (various Cu doped metal sulfides as

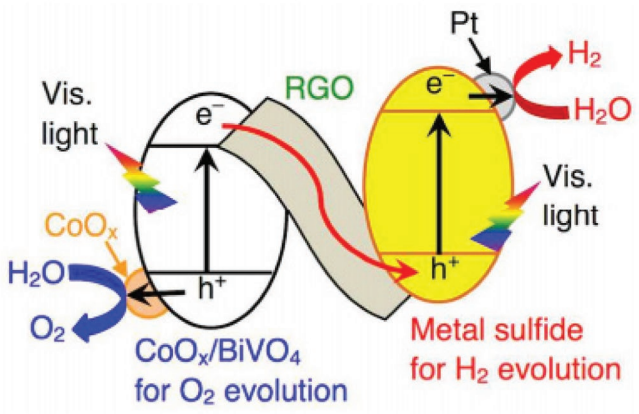

Figure 9. rGO induced Z-scheme water splitting by using CoO-loaded $BiVO_4$ as OEC and metals sulfides as HEC in the presence of Pt. Reproduced with permission.[117] Copyright 2016, American Chemical Society.

HEC) and CoO_x loaded $BiVO_4$ (OEC) instead of TiO_2.[117] For the photoelectrochemical water splitting, CoO-loaded $BiVO_4$ and $CuGaS_2$ were sprinkled with Pt; otherwise, no activity was found in the absence of Pt. A stoichiometric amount of H_2 and O_2 was observed under visible light when a proper Z-scheme was established; however, a negligible amount of H_2 was detected in the absence of CoO_x due to the photocorrosion. It means that the presence of CoO_x cocatalyst is the key factor to ameliorate the Z-scheme for water splitting (**Figure 9**). To further justify the role of CoO_x, various photoelectrochemical experiments were carried out. It was established in the previous study that there is no overlapped range of potential between pristine-$BiVO_4$ and $CuGaS_2$ for oxidation and reduction process, respectively, because of their onset potential around 0.1 V versus Ag/AgCl.[117] However, the potential of $BiVO_4$ is negatively shifted when an optimum amount of CoO was loaded. To this end, it is concluded that photoexcited electrons in $BiVO_4$ are shifted to rGO and then to $CuGaS_2$ without any external bias. Thus, pushing an electron from the $BiVO_4$ to $CuGaS_2$ through rGO endorse the Z-scheme water splitting.

Taking into account the above concept, Yushino et al. further explored the Z-scheme by controlling the size of the metal sulfides $(CuGa)_{0.5}ZnS_2$ as HEC while maintaining the same OEC (CoO-loaded $BiVO_4$).[118] By controlling the size and composition of HEC $(CuGa)_{0.5}ZnS_2$, the H_2 production activity was significantly enhanced by the easy interparticle transfer of electrons with the O_2 evolving counterpart. The developed Z-scheme gives AQY of 0.81% at 440 nm and STH of 0.024% for water splitting catalysis. In a similar work, Wang et al. developed a ternary hybrid material comprising $ZnIn_2S_4$ (ZIS), CoO_x loaded Bi_2MoO_6 (CoO_x/BMO), and rGO as OEC, HEC, and EM, respectively. Various amounts of Pt and CoO_x were used as cocatalyst with an optimum quantity of 0.5%.[119] It was perceived that less amount of H_2 and O_2 was observed in the absence of cocatalyst. However, the stoichiometric amount of H_2 and O_2 was significantly enhanced to 740.4 and 376.7 $\mu molg^{-1}$ in 24 h in the presence of cocatalyst as active sites for O_2 and H_2 production, respectively. In addition, the amount of electron mediator was also optimized and the highest activity was achieved by 3% rGO to fulfill the need of hole and electron for the stoichiometric amount of H_2 and O_2 production. The decrease in the activity by increasing the amount of rGO can be ascribed to the shading effect of rGO to block the penetration of light to the light-harvesting part (photocatalyst). From the above discussion, it can be assumed that rGO can be effectively used as an electron mediator and support in the Z-scheme water splitting module. In this regard, the amount of rGO is indeed worth considering for the competent production of H_2 with high conversion efficiency.

3.5. Graphitic Carbon Nitride (g-C_3N_4) Based Z-Scheme

Recently, highly exfoliated g-C_3N_4 nanosheets have revealed a prodigious potential for photocatalytic water splitting due to available active sites and surface defects allied with the enhanced active surface area which can efficiently induce the charge separation of photoexcited electron–hole pair.[120] In addition, g-C_3N_4, a non-toxic material shows high mechanical and chemical stability and appropriate band edge for H_2 generation. However, the moderate absorption capacity of the pristine g-C_3N_4 in the visible domain and charge recombination problems severely hamper the photocatalytic activity. Also, its oxidation potential is not adequate for water oxidation (OER), and therefore, the development of an appropriate Z-scheme photocatalyst is highly needed to attain overall water splitting capacity.[121]

g-C_3N_4 can be used either in direct Z-scheme heterojunction or in Z-scheme with the assistance of an electron mediator as shown in **Figure 10**.[122] In the direct Z-scheme heterojunction, the excited electrons of the negative CB of SC 2 connect with the positive VB edge of SC 1, creating holes and leaving electrons in the VB of SC 2 and CB of SC 1, respectively. In contrast, a conductor as an intermediate is sandwiched between two SCs increasing the rate of electronic transportation from SC 2 to SC 1.[123]

Recently, many reports on g-C_3N_4 based Z-scheme have been published such as WO_3/g-C_3N_4, TiO_2 /g-C_3N_4, MoO_3/ g-C_3N_4, and $BiVO_4$/ g-C_3N_4 for photocatalytic water splitting.[124,125] These types of material parade dual functions: i) an extraordinary high redox potential by maintaining a highly positive VB edge and negative CB edge and ii) high charge (electron–holes) separation efficiency. In this regard, Xia Tao and his co-workers proposed a mechanism for $CoTiO_3$ loaded g-C_3N_4. Both photosensitizers (g-C_3N_4 and $CoTiO_3$) absorb the photon and generate exciton from their respective VB to the CB. The solid–solid interface of composite material possesses many defects that owe similar conductor properties, such as electrical conductivity and comparable energy levels. These inherent properties offer the edge to act as a recombination center for electron–hole pairs so that the electrons produced from the $CoTiO_3$ CB could drift to VB of g-C_3N_4 via an interface and then recombine with the local holes, thereby stimulating the separation of photogenerated electrons from the CB of g-C_3N_4. The separated electrons are then transferred to Pt NPs and participate in the surface reduction for H_2-evolution. Meanwhile, the sacrificial agent quickly consumes the photogenerated holes on the $CoTiO_3$ surface easing the charge separation process and improving photocatalytic performance.[126]

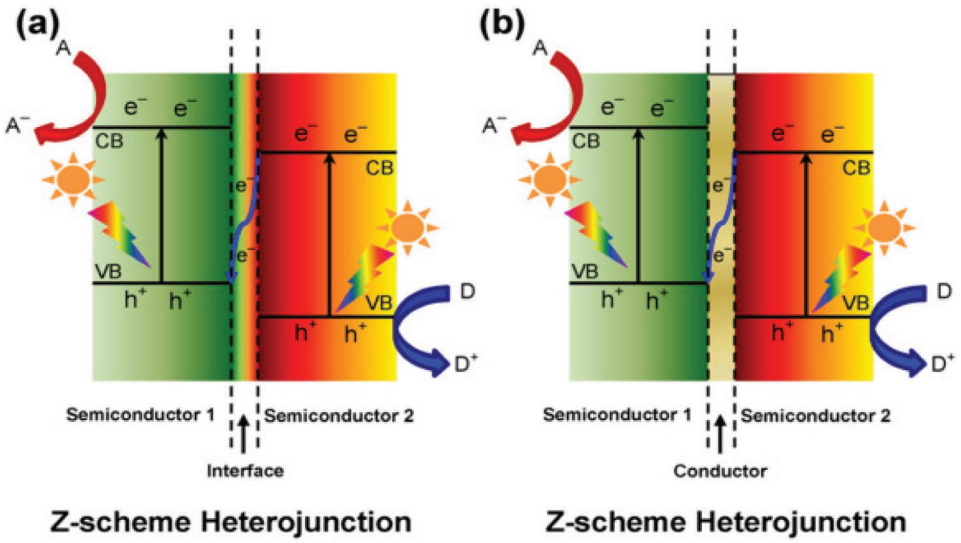

Figure 10. Systematic representation of two g-C_3N_4-based Z-scheme mechanisms. Reproduced with permission.[122] Copyright 2014, Wiley-VCH.

As mentioned earlier, a conductor is used to connect two SCs for providing a relatively easy pathway for electron migration from SC II to SC I.[127] The following criteria must be fulfilled while designing a highly effective g-C_3N_4-based photocatalyst: 1) maximum solar light absorption capacity, 2) high rate of charge transfer and the ability to prevent charge recombination, 3) high mechanical stability of composite material and its resistance against chemical transformation.[14] Usually, hybrid nanocomposite materials possess different unique merits, that is: i) maximum exposure to visible light, ii) cocatalyst to decrease the redox overpotential at the active sites, iii) accelerate the charge separation and migration, and iv) increase the overall composite material's chemical and mechanical stability by shielding the active sites and functional group through proper surface passivation.[128]

In this scenario, nanocomposite-based interface formation has become a feasible and fascinating approach to overcome the above-mentioned challenges to improve the photocatalytic behavior of g-C_3N_4. The 2D flat and flexible morphology of g-C_3N_4 nominates it as an ideal candidate for heterojunction with various other materials. Zhang and his co-worker developed a heterojunction using a simple hydrothermal strategy, that is, in situ growth of $CuInS_2$ on g-C_3N_4.[129] The composite catalyst exploits the Z-scheme system for the charge transfer pathway, which ensures the separation of photogenerated holes and electrons and increases the reaction rate. Under visible light illumination, hybrid structure enhanced the hydrogen evolution up to 1290 $\mu molg^{-1}h^{-1}$, which is 6.1 and 3.3 times higher than that of $CuInS_2$ and bare g-C_3N_4 nanosheets, respectively. A suitable selection of SCs at the nanoscale can efficiently trigger the charge transfer kinetics of light-induced carriers for proper exploitation of absorbed energy (photons).

Ultrasmall nanomaterials and g-C_3N_4 composite can provide a large number of active sites and enhance the interfacial charge separation and migration for photocatalytic water splitting. Dong Liu et al. reported 2D/2D hybrid material composed of H_2 treated WO_3 sheets, and Pt decorated g-C_3N_4 with a sheet thickness of 2.6 and 4.0 nm, respectively.[130] They observed that the hybrid nanomaterials demonstrate substantial activity for H_2 generation compared to a single counterpart. Using XPS, EPR, and energy band structure analysis, they found that the hybrid material follows a direct Z-scheme mechanism in which electrons move from WO_3 nanosheets to g-C_3N_4 nanosheets and then to Pt co-catalyst for H_2 generation. The significant enhancement in the charge carrier's extraction and utilization (holes from WO_3 and electrons from g-C_3N_4) was due to the strong interfacial interaction between two 2D sheets that led to the Z-scheme configuration and ameliorate the photocatalytic activity of the hybrid material. The strong interfacial interaction between thin nanosheets supports the Z-scheme mechanism to preserve the high oxidation ability of WO_3 and reduction ability of g-C_3N_4 and thus alleviates the charge recombination to significantly increase the photocatalytic performance.

Coupling two well-suited SCs to work as a bifunctional catalyst for both HER and OER is always open for further improvement. In this regard, boron-doped, nitrogen-deficient g-C_3N_4 nanosheets (BDCNN) are considered potential contenders for overall water splitting. Recently, Zhao et al. fabricated ultrathin g-C_3N_4 doped with various contents of the boron and nitrogen defects that can use either O_2 or H_2-evolving photocatalysts.[131] A well channelized Z-scheme has been established owing to the ultrathin structure that staggered band alignment and strong interfacial interaction. The prepared material showed significant performance with STH of 1.16% under visible light irradiations. The 2D/2D CNN/BDCNN was prepared via an electrostatic self-assembly technique, as shown in **Figure 11**a,b. The surfaces of both CNN and BDCNN are negatively charged with a zeta potential of −21.7 and −24.1 mV, respectively. It has been considered that g-C_3N_4 can be easily protonated by HCl in the presence of multi -C-N- motifs,[132] making the CNN surface positively charged. This led to the spontaneous electrostatic interaction between the acidified CNN and the BDCNN that construct the CNN/BDCNN 2D/2D heterojunction as evident from the TEM image (Figure 11c). Further, the structural examination is intuitively explored by the XPS and the X-ray absorption

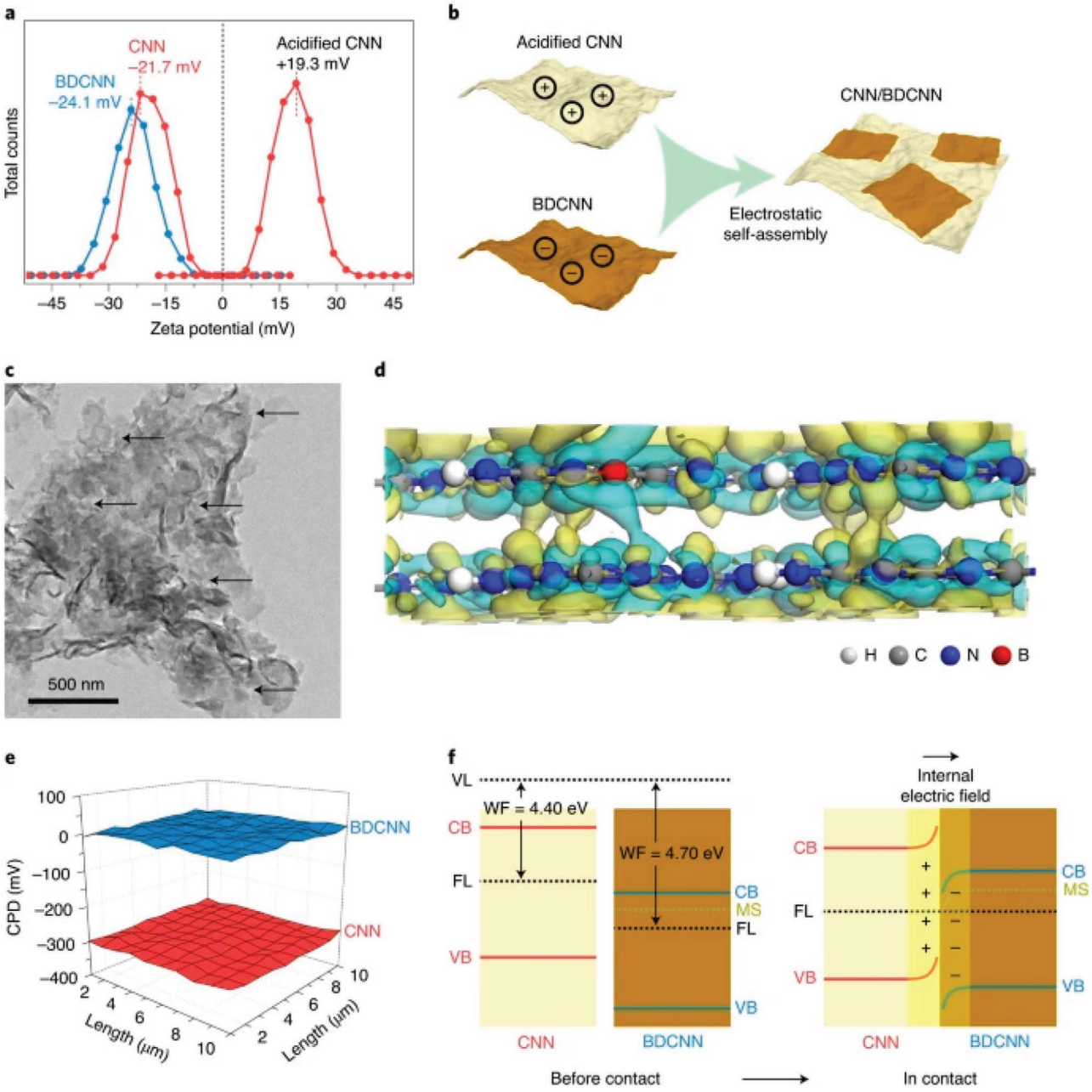

Figure 11. Construction of Z-scheme heterostructures, a) Zeta potential of the BDCNN, CNN, and acidified CNN dispersed in deionized water at pH 7; b) schematic of the synthesis of the CNN/BDCNN heterostructure; c) TEM image of CNN/BDCNN. The arrows indicate the overlapped interfaces. d) Side-view differential charge density map of CNN and BDCNN. The iso-surface value is 0.012 e Å^{-3}. The yellow and blue regions represent net electron accumulation and depletion, respectively. e) Contact potential differences of CNN and BDCNN relative to a gold reference; f) the energy band offsets diagram and interfacial charge properties for the CNN/BDCNN heterostructure. VL, vacuum level; FL, Fermi level. Reproduced with permission.[131] Copyright 2021, Springer Nature.

near-edge spectroscopy (XANES) (Figure 11d), where clear charge transfer channeling is detected between the CNN and the BDCNN. The work function was calculated using a Kelvin probe to investigate the electron transfer between the CNN and the BDCNN. It is considered that the interfacial charge is closely interrelated with the work function. As shown in Figure 11e, the contact potential between the BDCNN and the gold probe is 0 V, while –0.3 V is in between the CNN and gold probe. Therefore, the work function of the CNN and the BDCNN are measured which are 4.7 and 4.4 eV, respectively (Figure 11f).[133] This infers that when the contact between the CNN and the BDCNN is made, the electrons tend to move from the CNN to the BDCNN via intimate contact generated until the Fermi level is equilibrated.[134] Due to the internal electric field, electrons in the CNN observe repulsion which lifts the bands upward and vice versa for the BDCNN.

The nanomaterial incorporation can also increase the reaction rate and extend the absorption of pristine g-C_3N_4 to the visible region. Recently, researchers have observed that $Pd(OH)_2$ and $Co(OH)_2$ embeddedness in the g-C_3N_4 sheet create a unique separation of active sites for O_2 and H_2 production that conquers the reversal water splitting and also improves the charge separation.[135] The g-C_3N_4 sheets ensure fast charge transfer between the Co fragment and Pd fragment after photoexcitation. Co and Pd fragment remarkably reduce the overpotential for water splitting from 0.82 to 0.02 eV. The integration of two different SCs with different bandgaps provides significant catalytic performance with excellent charge separation and good light absorption. Chemical modification of g-C_3N_4 through doping creates a proper staggered band alignment, and photo-excited electron/hole paired with weak oxidation/reduction potential efficiently catalyzes photoelectrochemical water splitting.[135] The high redox properties of transition metal oxides increase the charge transfer ability of composite material and enhance photocatalytic performance. A recent report presented that the interface of Fe_2O_3/g-C_3N_4 exhibits high TOF for H_2 evolution (398.0 $\mu molh^{-1}g^{-1}$) which is 13 times greater than pristine g-C_3N_4 (30.1 $\mu molh^{-1}g^{-1}$). The interfacial boundary between Fe_2O_3 and g-C_3N_4 is favorable for charge transfer and separation. The Fe_2O_3/g-C_3N_4 composites can sustain both the high reduction ability of g-C_3N_4 and the high oxidation ability of Fe_2O_3, providing a significant driving force for the water-splitting reaction.[136]

The chemical and electronic properties of g-C_3N_4 impart a substantial impact on photochemical water splitting. Jiang and his co-workers reported different composites of g-C_3N_4/Ag_3PO_4 for photochemically driven OER. In composite, metallic Ag acts as a recombination center for holes of g-C_3N_4 and photogenerated electrons of Ag_3PO_4, so active holes are available in the VB of Ag_3PO_4 for OER.[137] In a recent report, $Bi_2O_2CO_3$ and g-C_3N_4 based heterojunction was employed for photochemical water splitting. Thermally reduced $Bi_2O_2CO_3$ NPs were loaded on the different positions of g-C_3N_4, namely, interlayer, edges, and surfaces that notably spread the interlayer distance and increase the active surface area. The experimental results deduced that $Bi_2O_2CO_3$ NPs have a substantial impact on adjusting the bandgap, enhancing absorption efficiency of visible light, and preventing photogenerated recombination electron-hole pair that remarkably improve the photocatalytic activity of g-C_3N_4 for HER.

The photocatalytic activity of $Bi_2O_2CO_3$/g-C_3N_4 composite reaches up to 965 $\mu molg^{-1}h^{-1}$ for 5 h; considerably higher than that of pristine g-C_3N_4 (337 $\mu molg^{-1}h^{-1}$).[138] Similarly, a heterojunction comprising of g-C_3N_4/Bi_4NbO_8Cl was developed via the facile ball milling method to create an intimate interface between two faces. These results demonstrate that strong interfacial interaction between g-C_3N_4 and Bi_4NbO_8Cl extends the photoabsorption to the visible range (over 500 nm) and increases the number of captured photons. The g-C_3N_4/Bi_4NbO_8Cl Z-scheme significantly enhances the H_2 production rate with TOF of 67.2 which is 6.9 times higher than that of bare Bi_4NbO_8Cl and g-C_3N_4. Electron spin resonance spectroscopy (ESR) and time-resolved photoluminescence decay-based data unveiled that this improvement is primarily owing to the development of a Z-scheme junction to endorse the separation and migration of excited charges that obstruct the recombination process effectively.[89]

It is well established that the efficient separation of photogenerated holes and electrons is responsible for high activity. The hydrogen evolution rate for Cd_xZn_{1-x} S/Au/ g-C_3N_4 is found much higher than Au/ g-C_3N_4 and CdS /Au/ g-C_3N_4 attributed to the efficient separation of the photogenerated carrier.[139] The strong interfacial interaction between NPs and g-C_3N_4 increases the lifetime of photoexcited charges and, therefore, increases the catalyst durability. Usually, metal/metal oxide NPs tend to aggregate due to their high surface energy, and therefore, can easily leaching out from the substrate. The C-N network in g-C_3N_4 decreases the surface energy of NPs and enhances the number and activity of the available active sites by altering the charge density of the interface. g-C_3N_4 supported $W_{18}O_{49}$ is an exciting example of a highly dynamic and durable photocatalyst. For instance, Yang and his co-workers successfully loaded the g-C_3N_4 quantum dots inside $W_{18}O_{49}$ nanoflowers to form a heterojunction.[140] The positively charged g-C_3N_{4-x} QDs in the vicinity of N heteroatom and negatively charged $W_{18}O_{49}$ nanoflowers create an intimate contact due to the Coulombic attraction. This firm contact increases the kinetics of photochemical reaction (H_2 production activity; 4278 $\mu molh^{-1}g^{-1}$), which prevents the NPs from aggregation, and meanwhile, increases the charge carrier transportation. Surface engineering by introducing metal ion vacancy into target catalyst is another promising strategy to boost photocatalytic water splitting activity. Such surface modification optimizes the material's electronic structure to ensure an optimum binding with the reaction intermediate and increase the adsorption/desorption kinetics. A Z-scheme system that included monolayer g-C_3N_4 and 2D MnO_2 recently reported by Li and his co-worker[90] shows high photochemical water splitting activity. The Mn^{3+} defects act as active sites that promote water adsorption and interfacial charge transfer by persuading Z-scheme charge transfer via the redox cycle between Mn^{3+} and Mn^{4+} (**Figure 12**). Notably, controlling the specific stoichiometry of Mn significantly boosted the HER under visible light irradiations.

3.6. Perovskite-Based Z-Scheme

Metal oxides are promising electrodes in photoelectrochemical water splitting and are widely explored due to their high redox potential, superior stability, low cost, and easy nanostructuring capability. For an efficient photochemical process, the catalyst should have high light absorption capability and inherent potential, which cannot be easily attained by simple metal oxide due to its fixed atomic structure. Perovskite oxide (ABO_3) is a more potential candidate than simple oxide due to its excellent structural and compositional flexibility that offers several properties such as high activity, durability, precise control of band edges and bandgap, excellent visible light absorption capacity, and an appropriate redox capability.[141] More precisely, alkali metals (Li, Na, K, etc.), alkaline earth metals (Ba, Sr, etc.), and rare earth metals (Ce, La, etc.) can lodge the A site, while many transition metals (Ti, Mn, Fe, Co, Ta, etc.) can be used as B site elements of perovskite. The flexible surface component of perovskite oxide and its chemical and physical

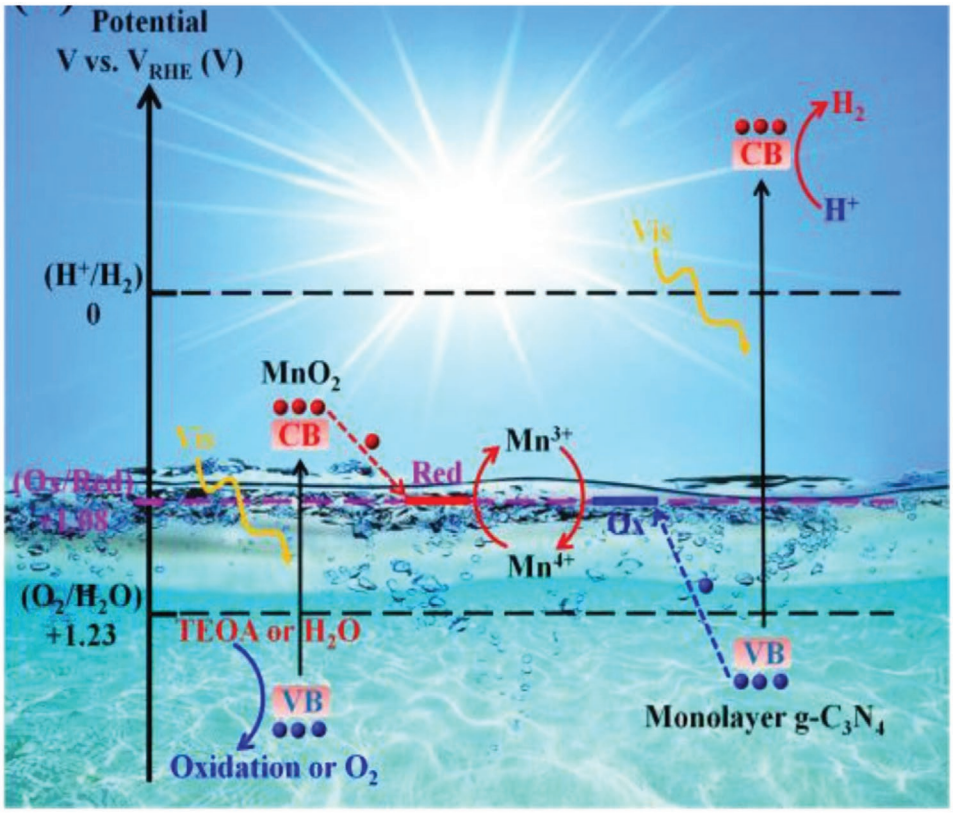

Figure 12. Z-Scheme charge transfer mechanism diagram of MnO_2/Monolayer g-C_3N_4. Reproduced with permission.[90] Copyright 2019, Elsevier.

properties make it a potential candidate to tune the water activation process.[142]

The surface chemistry and structural arrangement of perovskite have played a key role in Z scheme photocatalysis. For example, $BaTaO_2N$ (having an adsorption edge around 660 nm with an E_g of 1.9 eV) was synthesized through the flux method by nitridation of barium enriched $LiBa_4Ta_3O_{12}$ as a precursor using a solid-state approach. The further modification of the catalyst surface was carried out by nitration of equimolar ratios of Ta and Ba-containing compounds at a high temperature in ammonia to create dense defect sites. After a controlled experiment, they found that crystalline BTON-flux ($BaTaO_2N$, prepared by flux method) exhibited a magnificent surface area and reduced defect density than that of the BTON-SSR sample (synthesized by solid-state reaction). The BTON-flux sample's performance is much better than BTONSSR during Z-scheme complete water splitting for HER because of structural differences.[143] Similarly, $CaTiO_3$ has played a vital role in increasing $CoTiO_3$/g-C_3N_4 (CT-U) nanocomposite performance because of electronic band strength, high mobility of carriers, and effective absorption coefficient.[126] It has played the best part in OER because of the suitable band edges ECB = 0.1 eV, EVB = 2.35 eV, which align favorably with g-C_3N_4 (ECB = −1.3 eV, EVB = 1.4 eV) to create Z-scheme photocatalytic system. The 2D nature of g-C_3N_4 and ID characteristics of $CoTiO_3$ make a firm contact at the interface. This interaction boosted the catalytic activity (optimum catalyst 0.15%) with maximum quantum efficiency and H_2 production rate of 858 $\mu molh^{-1}g^{-1}$. This enhanced activity is because of the Z-scheme process for charge separation which mitigates the photoexcited electrons and holes recombination efficiently, while it has also a strong redox ability as compared to traditional type-II heterojunction (**Figure 13**).

The heterojunction interaction and intimate interfacial contact of perovskite with g-C_3N_4 have been anticipated to boost the photocatalytic performance of g-C_3N_4. A recent report showed that $LaCoO_3$/g-C_3N_4 demonstrates high performance because of promising characteristics of g-C_3N_4 (owing to the pyridinic and pyrrolic N), sp^2 hybridized carbon, high stability, and efficient charge transfer capacity of $LaCoO_3$.[144] The use of $LaCoO_3$/g-C_3N_4 photocatalyst reduced the electrons/holes recombination and increased the catalytic activity. The interconnected junction and high bonding strength between g-C_3N_4 nanosheets and $LaCoO_3$ NPs produced H_2 at a high rate, that is, 1046.15 $\mu molh^{-1}g^{-1}$, and this rate of H_2 production is many times higher than the individual substrates. It indicated the high charge transfer capability because of the available electron–hole pair domains.

Rhodium-doped $SrTiO_3$ also shows high efficiency for visible light photocatalysis when used in combination with electron shuttle reagents, also called electron donors like $Co^{3+/2+}$ complexes, Fe $(CN)_6]^{3-/4-}$, and $Fe^{3+/2+}$. The mechanical approach depends on electronic conductive layers and interparticle electron transfer rates. The combination of $SrTiO_3$:Rh OEC like $BiVO_4$ further enhances the activity. The photogenerated holes in $BiVO_4$ and excited electrons in $SrTiO_3$:Rh increase HER and OER kinetics. The $BiVO_4$, because of its suitable CB, facilitates

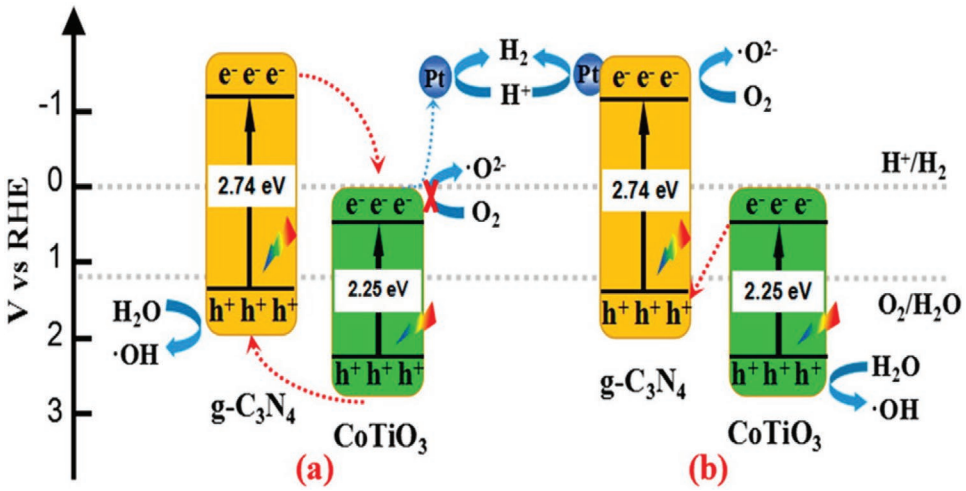

Figure 13. Schematic illustration for charge separation by traditional heterojunction-type (a) and direct Z-scheme (b) mechanisms. Reproduced with permission.[126] Copyright 2016, American Chemical Society.

the redox electron shuttle from the CB to Rh^{3+} holes of Rh^{3+} and reduces $SrTiO_3$: Rh level. Physical contact development between $BiVO_3$ and $SrTiO_3$: Rh by depositing rGO mediates electron transfer between two SCs and increases the reaction rate at the electrode–electrolyte interface. Similarly, rhodium-doped $SrTiO_3$ micro-spherical particles of 1–2 µm in size prepared through the spray drying (SD) method reveal the Z-scheme mechanism for water splitting employing electron shuttles such as $[Co(bpy)_3]^{3+/2+}$ and $Fe^{3+/2+}$ and its activity is higher than the same samples synthesized by solid-state reaction (SSR). This enhancement is in line with the high rate of interparticle electron transfer. More promisingly, by decreasing the concentration of $SrTiO_3$: Rh and $Fe^{3+/2+}$, the SD sample well preserved its activity compared to PC and SSR samples. The new results demonstrate that physical contact between perovskite and support imparts a substantial impact on catalysis.[145]

Several other bismuth-based perovskites like Bi_2WO_6, $BiVO_4$, Bi_4NbO_8Cl, and BiOX have been regarded as fabulous photocatalysts with extensive stability and high-water splitting activity.[146] The primary reason behind the performance is the compact hybridization of p orbital of oxygen in junction with 6s orbital of bismuth both in CB and VB. This hybridization between O 2p and Bi 6s orbitals is rendered by raising the VB to a maximum negative value, narrowing the bandgap, and extending the optical absorption to a more extended wavelength region. Similarly, a series of bismuth tantalum oxyhalides, that is, Bi_4TaO_8X where X = Cl, Br, having a CB at –0.70 eV and VB at 1.80 eV positions versus the reversible hydrogen electrode (RHE) demonstrated the capability for overall water splitting under visible light irradiation. Bi_4TaO_8X, where X = Cl, Br, manifested a quantum efficiency of 20% for water oxidation (at 420 nm). A Z-scheme system coupled with Bi_4TaO_8Br and Ru/$SrTiO_3$:Rh also revealed a remarkable performance for complete HER and OER with fast kinetics.[147] Hierarchical core–shell infrastructure has been designed through the in situ fabrication of $BiVO_4$ @$ZnIn_2S_4$/Ti_3C_2 MXene quantum dots that follows a direct Z-scheme mechanism. Ti_3C_2 MXene QDs were applied as cocatalysts which can accelerate the redox reaction kinetics. Further, the energy barrier for an electron at SC- metal junction is also known as Schottky barrier formation which occurred at the interphase of the $ZnIn_2S_4$ to promote charge separation. $BiVO_4$@$ZnIn_2S_4$/Ti_3C_2 MXene QDs attain efficient visible light-driving activity used for overall water splitting (having O_2 and H_2 rates of 50.83 µmol$g^{-1}h^{-1}$, 102.67 µmol$g^{-1}h^{-1}$, respectively) with ≈96.4% efficiency. Ti_3C_2 MXene participated as cocatalysts and promoted the reduction of the proton, while hierarchical core–shell infrastructure offered more active sites and assembled Z-scheme.[148]

Along with dual-core shelled structures, oxyhalides materials, like Bi_4MO_8X where M = Ta and Nb, and X = Br and Cl, are also considered as promising catalysts with exceptional bandgap. Series of double-layered analogs $AA'M_2O_{11}Cl$ where A/A′ = Sr, Ba, Pb, and Bi, and M is Ti, Nb, and Ta have also been synthesized through precursors of oxyhalides and preliminary synthesized oxides of multiple metals. On changing composition, both CB minimum and VB maximum of $A_4A'M_2O_{11}X$ are tunable to some extent compared to Bi_4MO_8X having unvaried VBM and CBM. Ba and Pb doping in $Sr_2Bi_3M_2O_{11}Cl$ narrows the bandgap of VB and CB edges. DFT calculations using modeling techniques and structural characterizations through state-of-the-art spectroscopic techniques revealed the primary reason for band edges position (further comprehensive discussion is given in the following section). It is mainly due to the interaction of oxygen 2p, Pb/Bi lone pairs of $6s^2$, and Madelung potential sites of Bi^{3+} cations. The maximum occupancy of Bi^{3+} inside the fluorite layer indicated enhanced conductivity and activity of various excited electrons improving photochemical water oxidation under visible light.[149]

Photocatalytic activity of specific 3D composites like Bi_2WO_6 is not satisfactory because of electron–hole pair recombination, limited active site exposure, lower specific area, and the narrow response to visible light. Thus, surface and morphological modifications of such composites are surmounted by their interaction with 2D system heterojunctions. These junctions assist in separating electron–hole combinations as well as electron transfer. Various 2D composites have been designed like Bi_2WO_6/TiO_2, rGO/g-C_3N_4, BP/bismuth vanadate, and a-Fe_2O_3/g-C_3N_4. Star-shaped 2D black phosphorous integrated

with Bi_2WO_6 monolayer has proven itself as a favorable candidate for photocatalytic water splitting, owing to its unique optical, physical, and chemical characteristics.[150] The heterojunction of 2D/2D BP/monolayer Bi_2WO_6 (BP/MBWO) also revealed enhanced catalytic activity performance to evolve N_2 and H_2 to purify the air.[149] The maximum rate of hydrogen evolution is 21 042 μmolg^{-1}, which is 9.15 times greater than that of pristine MBWO. The ratio of NO removal was found around 67%. The mechanical approach in this setup has been monitored based on the environmental pollutants of daily life.[151]

N-doped SCs are considered promising photocatalysts with an absorption band of a broad spectrum,[152] although thermal instability and the worst charge separation of these catalysts hinder its large-scale viability. However, its heterojunction with perovskite material increases the absorption spectrum and charge separation dynamics.[153] Such as $BaMg_1/3Ta_{2/3}O_{3x}N_y$ exhibits superior transfer capability and maximum charge separation because of intimate interfacial contact and suitable bandgap alignment.[154] Furthermore, certain perovskites enormously stimulate $NaNbO_3$ due to their chemical stability, maximum resistance toward photo-corrosion in aqueous solution, abundant availability, lower environmental impact, and cost-effective nature.[155] On the other hand, $NaNbO_3$ has a broader bandgap (3.4 eV) and is therefore highly active in the UV region, usually combined with the material having a lower bandgap with perfect alignment resulting in nanostructured architecture.[155,156] The double core heterostructure morphology of $NaNbO_3$ exhibits a wide bandgap as compared to $CuInS_2$ and In_2S_3. This structure has many defects and revealed a current density of 6.7 mA cm^{-2} at –1.0 V and a lower overpotential of –110 mV than the type 2 system with a current density of 16 mA cm^{-2} and onset potential of –180 mV versus Ag/AgCl. The Mott Schottky confirmed the n-p-n heterojunction formation in $NaNbO_3$-$CuInS_2$-In_2S_3, which further reduced the recombination of charged carriers (**Figure 14**).). This system also exhibited tremendous degradation for organic pollutants with an efficiency of around 99.6%. Researchers found that this pathway provides a more efficient charge separation mechanism in heterostructures of $NaNbO_3/CuInS_2/In_2S_3$ than Type II, that is, $NaNbO_3/In_2S_3/CuInS_2$.[157]

3.7. Metal Sulfide-Based Z-Scheme

The metal sulfides working as an H_2- evolving photocatalyst in the Z-scheme system give cathodic photocurrents. For metal sulfides, photo corrosion is a key issue and that limits their practical application in photocatalysis.[158] Therefore, a suitable Z-scheme heterojunction that effectively prevents the photo corrosion of metal sulfides should be designed.[23]

CdS seem to be a superb photocatalyst for HER because of its appropriate bandgap around 2.0 eV. However, the low activity and charge separation problems associated with CdS can be tuned either by morphological changes in its micro/nanostructures or by coupling with other SC. For example, CdS/WO_3 heterojunction has been developed by Zhang et al. for photocatalytic water splitting.[159] Although WO_3 alone cannot catalyze water splitting, however, it does play a considerable role when coupled with CdS to establish Z-scheme while using lactose as an electron source. They have used different combinations of CdS/WO_3 by varying the amount of CdS. Interestingly, 369 μmol $h^{-1}g^{-1}$ of H_2 was produced using 20% CdS with lactic acid as an electron donor which is six times greater than a single WO_3. More recently, a ternary Z-scheme ($CdS/rGO/g\text{-}C_3N_4$) was developed as an H_2 evolving catalyst.[82] This Z-scheme was constructed with a hydrothermal process by exfoliating $g\text{-}C_3N_4$ and its subsequent coupling with two SCs. By comparing the photocatalytic activity, a significant increase in the ternary-based Z-scheme was observed owing to their high conductivity, better charge separation, and stability. The high conductivity of rGO plays a major role in channeling the electron at the interface of two SCs and thus can strengthen the Z-scheme pathway. The proficient role is evident from the H_2 production rate of 676.5 μmol $h^{-1}g^{-1}$ and AQE (36.5% and 1980.2 μmol g^{-1}) while using a ternary hybrid system with an optimum 50 wt% $g\text{-}C_3N_4$. By increasing the amount of $g\text{-}C_3N_4$ (≥70%), a decrease in the activity was observed which reveals the possible blocking of surface available for catalysis. The proposed mechanism for the charge transport between CdS and $g\text{-}C_3N_4$ through rGO was designed based on the band position of the two SCs and the electron migration ability of rGO (**Figure 15**). The electrons under light irradiations readily excite from the VB to the CB of each SC and consequently generate holes in VB. The oxidation potential of the VB of CdS (1.88 eV) can effectively oxidize

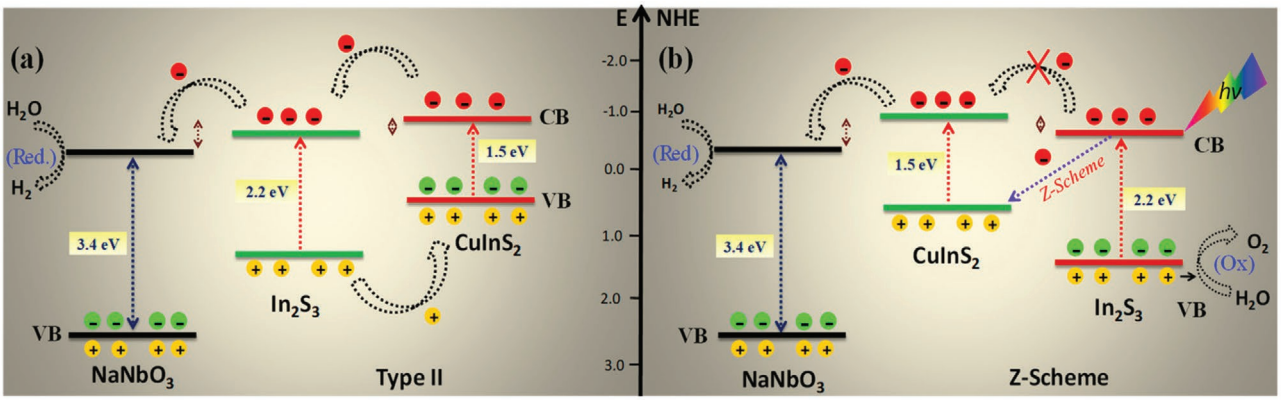

Figure 14. Z-Scheme Band alignment between $NaNbO_3/In_2S_3/CuInS_2$ and $NaNbO_3/CuInS_2/In_2S_3$ core/shell heterostructures, respectively. Reproduced with permission.[157] Copyright 2018, American Chemical Society.

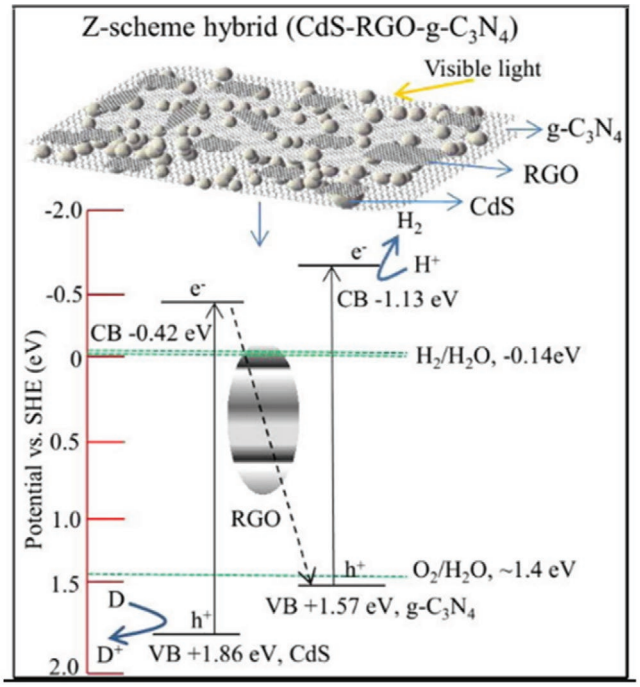

Figure 15. Z-scheme electron transfer mechanism; a) Schematic illustration of charge transfer mechanism in CdS-rGO-g-C_3N_4.Reproduced with permission.[82] Copyright 2017, Elsevier.

sacrificial reagent in the solution.[6] Meanwhile, the electrons in the CB of CdS transfer to rGO and then to g-C_3N_3 mediated by rGO due to the strong internal contact with CdS. Thus, the excess electrons in the CB of g-C_3N_4 are utilized in the reduction of the H^+ for H_2 production.

The solid–solid contact plays an important role to facilitate electron transfer from one SC to another SC. However, such a type of contact also creates several defects which can be addressed by reducing the solid–solid interfacial contact. For example, CdS/WO_3/rGO was organized by Huang et al.[160] where the function of rGO was not only to mediate but also enhance the transport of electrons. After illumination of the two SCs, the electrons present in the CB of CdS directly relocate to the VB of WO_3 without mediator owing to the strong electrostatic interaction of two SCs.[1] Such a direct coupling of SCs not only minimizes the recombination process but also improves the reaction conversion efficiency.

The quantum dots illustrated their capabilities related to surface effect, bandgap adjustment, spectral responses, the size effect of quantum, and maximum quantum efficiency. The composite CdS/Pt/$NNaNbO_3$ (18% CdS and 2% of Pt/N-$NaNbO_3$ nanorods) is reported as an active catalyst with hydrogen evolution rates of 14218 and 29297 $\mu molg^{-1}h^{-1}$ under visible light and simulated sunlight irradiation, respectively.[161,162] Platinum facilitates maintaining a bridge toward the electronic transfer pathway acting as a photo-induced charge carrier. The activity of $NNaNbO_3$ nanorods is 134 and 28 times greater than bare nanorods of $NaNbO_3$ and CdS quantum rods, respectively, under visible light (λ >420 nm).[155]

Recently, photocatalytic HER together with selective oxidation of organic compounds to produce high-value chemicals has attracted significant attention. Li et al. have used CdS-decorated MOF composites (CdS/MIL-53-Fe) and coupled oxidation of organic benzyl alcohol and H_2 production steps in a single reaction to achieve overall redox cycle simultaneously, without employing any sacrificial reagent and noble metals.[163] The as-prepared material showed excellent activity of H_2 production rate of 2334 $\mu molg^{-1}h^{-1}$ under visible light irradiations. Similarly, they have generated the same reactions (H_2 production and oxidation of benzyl alcohol) over CdS@MoS_2 heterostructures and have achieved 4233 $\mu mol\ g^{-1}\ h^{-1}$ without the need for a noble metal or sacrificial reagent. This is considered to be a very good strategy to obtain valuable chemicals in a single step via a Z-scheme strategy.[41]

Co_9S_8 has been considered a tremendous photoelectrochemical catalyst based on its performance in specific contexts because of maximum flat band potential, narrow bandgap, and efficient charge carrier capability through sulfur atoms at the interfacial surface metal.[164] Hollow structures with the controlled design of cubes of cobalt sulfide embedded in CdS quantum dots have also been explored. The hollow $Co(OH)_2$ was used as a template utilizing the one-pot hydrothermal method. The hollow cubes of CdS/Co_9S_8 employ multiple light reflections in cubic infrastructure to accomplish the improved photocatalytic activity. Significant separation of photoexcited charge carriers might be achieved by constructing a Z-scheme system free of the redox mediator. The hollow CdS/Co_9S_8 shows a hydrogen evolution rate (1061.3 $\mu molg^{-1}h^{-1}$) that is 9.1, and 134 times greater than CdS QDs (116.3 $\mu molg^{-1}h^{-1}$), and pure hollow Co_9S_8 (7.9 $\mu molg^{-1}h^{-1}$), respectively, under simulated solar light irradiation. Hollow cubes Co_9S_8 SCs are ideal electron donors for constructing a redox mediator-free Z-scheme system with photocatalytic water splitting application (**Figure 16**).[165]

Zhang et al. have recently reported Co_9S_8/Cd/CdS Z-scheme type heterojunctions with hierarchical tubular structure using inexpensive transition metallic electronic bridge between two different SCs by in situ reduction strategy.[166] The intended heterostructure significantly propagates redox activity because of highly dense catalytic sites and visible light-capturing capability owing to a suitable bandgap of Co_9S_8/CdS. The other prime essential factors are the hollow framework which is in conjunction with faster charge separation and smooth transfer with conductive Cd. The hydrogen evolution rate is 10.42 μ $molh^{-1}g^{-1}$ with optimized protocols, without any drop in performance after multiple cycles. The higher flatter band of more negative potential for water reduction and narrower bandgap qualify Co_9S_8 as the promising counterpart of the CdS. The sulfur atom shared between two SCs helps to boost intermolecular interactions during the effective charge transfer process. Such charge separation and migration can also be improved by metallic redox mediator insertion.

The primary reason for the construction of heterostructure using metal sulfide-based photocatalysts is to reduce charge e^-/h^+ pair recombination. Using metal sulfides, various Z-scheme heterojunctions can be established depending on the mechanism of charge carriers.[167] It is categorized as a reduction photosystem because of the energy position of the ion band which is used for hydrogen production and carbon dioxide reduction.[168]

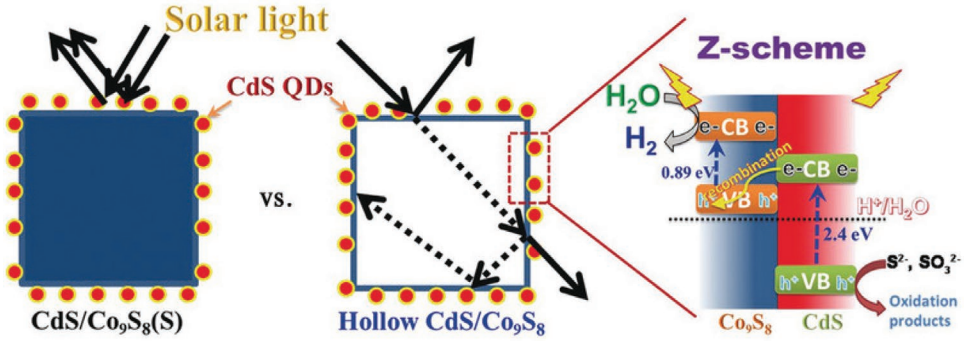

Figure 16. Systematic Illustration of multiple reflections within the CdS/Co_9S_8 hollow structure and the photoexcited charge-carrier distribution. Reproduced with permission.[165] Copyright 2017, Wiley-VCH.

3.8. Unexplored Z-Scheme

The applications of the Z-scheme approach are not only limited to water splitting but also extended in other catalytic processes to address the challenges associated with traditional photocatalytic materials. In this section, we will discuss powder-based catalytic system, particularly solid-state, plasmonic-based, and complex hybrid-based Z-schemes which are employed in various catalysis processes, and has the potential to be used in photocatalytic water splitting.

3.8.1. Solid-State Z-Scheme

For the efficient and selective designing of the new catalytic system, Tada and his co-workers have synthesized a CdS/Au/TiO_2 heterojunction, where CdS acts as a reducing site, while TiO_2 as an oxidizing site, and both are especially interconnected via Au to facilitate the electron transfer.[1] From the photocatalytic performance, it was deduced that by inserting Au, the activity can be enhanced as compared to individual SCs or their combination. This can be attributed to the anisotropic electronic moment between two SCs. Consequently, the engineered energy band of the ternary compound ($\lambda > 400$ nm) (**Figure 17**a) can reduce the methylviologen (MV^{2+}) instead of the electron transfer to Au attributable to the nanosizing of CdS.[169] The holes in the VB of CdS are occupied by the electron transfer from the Au (electron transfer I, Au → CdS). The holes present in the VB of TiO_2 oxidize the solvent, while electrons present in the CB of TiO_2 transfer to Au (electron transfer II, TiO_2 → Au). The instantaneous electron transfer via paths I and II probably happens due to the electronic excitation of two SCs under the MV^{+2} reduction condition.

3.8.2. Plasmonic Z-Scheme

A surface plasmonic phenomenon in NPs has recently attracted much attention in photocatalysis and is progressively extended toward photocatalysis employing Z-scheme.[170] Recently, $H_2WO_4 \cdot H_2O$/Ag/AgCl nanocomposite has been established by Ye et al. to degrade methylene blue.[171] They have observed an excellent performance which might be due to the two-step excitation caused by surface plasmon resonance (SPR) of Ag NPs and bandgap of $H_2WO_4 \cdot H_2O$. Similarly, Ye et al. prepared a composite material comprised of three components (Ag/AgX/BiOX (X = Cl, Br).[172] This composite was evaluated for photocatalytic degradation of Rhodamine B, which exhibited better

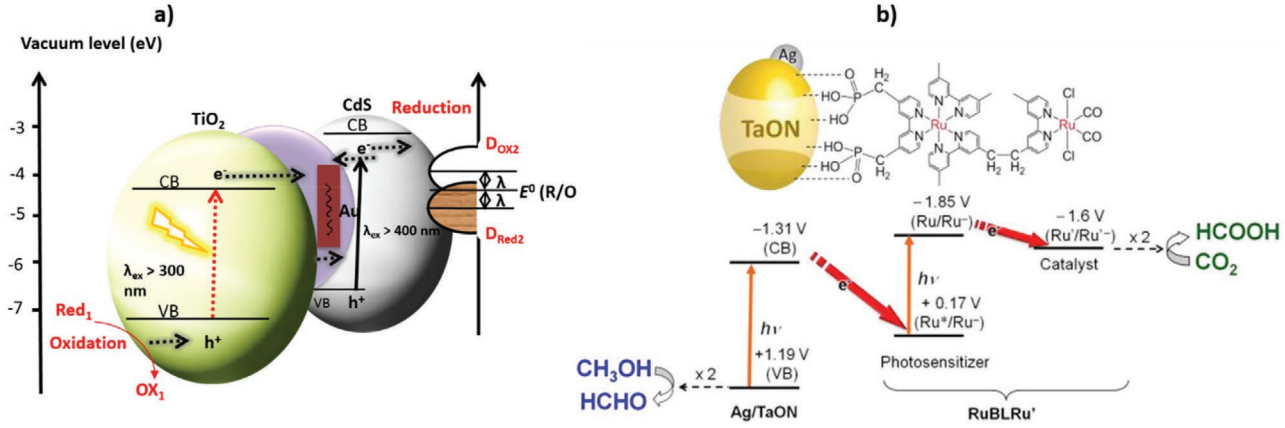

Figure 17. a) The band alignment illustration of CdS–Au–TiO_2 Z-system where the standard electrode potential of MV^+/MV^{2+} is represented by E^0 (R/O) while the occupied and unoccupied states are denoted as D_{Red2} and D_{Ox2}, respectively. Reproduced with permission.[169] Copyright 1991, American Chemical Society. b) Artificial Z-scheme for the catalysis of CO_2 and methanol. Reproduced with permission.[173] Copyright 2013, American Chemical Society.

performance than individual components of the composite under similar conditions where the nature of halogen has a profound role. For instance, in the presence of Cl, the SPR phenomenon is pronounced while in the case of Br, it can abridge the whole system to endorse the Z-scheme catalysis process.

3.8.3. SC/metal Complex Hybrid System as Z-Scheme for CO_2 Reduction

CO_2 reduction is a fundamental reaction in artificial photosynthesis and energy conversion processes. Recently, Ag-loaded TaON has been developed by Ishitani et al. for the reduction of CO_2 using Ru(II) complex.[173] During this reaction, formic acid is produced as a reduction product while formaldehyde is an oxidation product from the reaction of CO_2 and methanol, respectively. In the excitation process, both the molecular sensitizer and Ag-TaON are participating under visible light ($\lambda > 400$ nm) where the electron from CB of Ag-TaON are readily migrated to the excited state of the sensitizer to produce one-electron reduced species. This electron is rearranged in the sensitizer and shifted to the catalyst, which is a thermodynamically feasible process. The remaining hole in the Ag-TaON can catalyze methanol to formaldehyde while the catalyst unit with extra electron under reduction process converts CO_2 to formic acid (Figure 17b). From the above-aforementioned examples, it can be deduced that various approaches have been exercised to develop a new hybrid system employing the Z-scheme pathway for photo-assisted catalysis processes; however, several Z-scheme systems have not yet been explored for HER from water; more information on them need urgent attention to extend their role towards water splitting.

3.9. Critical Remarks

The Z-scheme photocatalytic module offers a sustainable solution to address the associated issues with photocatalysis owing to the special vector electron transport pathway.[174] Nevertheless, the strong dependency upon pH, backward reaction as well as shielding effect caused by redox mediators, substantially restrict the practical application of this technology.[21] The advancement in Z-scheme heterojunction has been progressively leading to enhanced photoactivity. Certain aspects of such a system still need in-depth understanding. These enhancements in such activity are often ascribed to the better charge carrier separation and/or the alternative charge pathway between two different materials; however, it is inevident to justify such claims. Rather than considering the complex nature of the photocatalytic system, for example, the presence of multiple pathways for the formation of reactive species, it is not uncommon to see different mechanistic explanations for the same kind of heterojunction photoactive system. Such proposed mechanism should be supported by independent techniques such as VB-XPS, ultraviolet photoelectron spectroscopy (UPS), XANES, XAS, and electron paramagnetic resonance (EPR) for the detection of radical formation.[93,175,176] Notably, adsorption plays a vital role in surface photocatalysis,[14,131,177] provided that its properties and surface charge (zeta potential values) could be different from the single-component system, hence, such study deserves considerable attention.

Taking into account the selectivity, the other major challenge is how to suppress the backward reactions while separating the O_2 and H_2.[178] To this end, the key role can be played by redox couples however, unique merits such as suitable redox potential, that is, between the oxidation (1.23 V vs NHE; pH = 0) and reduction potential (0 V vs NHE; pH = 0) of water, high redox cyclability without any precipitations and excellent transparency to UV–vis irradiations are required in this quest. It is quite challenging to construct an effective Z-scheme water splitting system while employing a redox couple mediation strategy. For example, the reduction of oxidant to reductant is thermodynamically more favorable over HER.[179] Similarly, the oxidation of reductant to oxidant is also preferred over OER. The two reactions need different redox concentrations; hence, it is challenging to selectively attain the HER and OER simultaneously. In most cases, a high concentration of oxidant is needed for OER and reductant for HER, which ultimately suppresses the corresponding half-cell reactions. Therefore, it is required to develop efficient redox couples and highly selective photocatalysts for forward reactions. In addition, mediators should be evaluated based on redox ability as well as their mechanistic role with the bound SCs. For example, Li et al. believe that the charge transfer in Z-scheme can be facilitated by the interfacial energy band bendings considering that the potentials of the used electron mediator should position well between the Fermi level of PS II and PS I.[180]

There are still some of the facets pertaining to the experimental challenges such as exploring the possible approaches to decrease structural defects, controlling topology, and lowering the energy barrier to effectively utilize the photogenerated charge carriers especially in narrow bandgap materials used in Z-scheme heterojunctions.[181] For instance, the addition of carbonaceous materials such as graphene and carbon nitrides as a redox mediator and the use of nanocluster instead of NPs are emerging potential contenders to the family of Z-scheme,[83] yet, the conductive carbon is not as prevalent (compared to the conventional metallic conductor) when constructing the PS-C-PS system. However, much attention is needed for the preparation of carbon-based Z-scheme to prevent defects during the fabrication process to enhance the efficiency of the system.

Particulate photocatalyst sheets are a new promising approach that has significant scalability in overall water splitting.[182] The charge transfer dynamics is an open challenge for both HEP and OEP using the Z-scheme module.[183] A remarkable outcome in this quest has been achieved by Wang et al., who prepared a sheet of La- and Rh-codoped $SrTiO_3$ ($SrTiO_3$:La, Rh) and Mo-doped $BiVO_4$ ($BiVO_4$:Mo) powders wrapped in an Au layer. Such surface modification split water with an STH efficiency of 1.1% at pH 6.8 and achieves an AQY of over 30% under visible light irradiations.[39] Finally, there are still many uncertainties, for example, the concept of recombination of electrons and holes is still unsure. It is broadly said that recombination is what determines the rate of photocatalysis: A high recombination rate means lower will be the reaction rate; however, more research is needed to get further insights. It is still very difficult to precisely quantify the recombination process. Although Z-scheme photocatalysis is a research domain that

provides extensive solutions for energy and environmental concerns but still requires considerable experimental attention to tackle the remaining uncertainties and misconceptions.

4. Theoretical Modeling of Photocatalytic Z-Scheme Water Splitting

Theoretical approaches can be used to investigate various aspects of the photocatalytic Z-scheme water splitting system, in particular, the electronic structures of the SCs, the charges separations and transportation, the band edge alignments of the heterojunction, and the photo-redox chemistry.[184–186] Specifically, the effect of the Z-scheme on the charge separation, the relative positions of CB and VB edges of the SCs, and the band offsets of the connected materials need to be carefully understood. The mobility of charge carriers can be modulated by establishing the band offsets, and therefore, when such a junction is developed, the electrons always move to the lowest CB edge. The conductivity of heterojunction is weighted by the positions of the fermi levels that create an interfacial electric field at the interface.[98] Owing to the difference in the Fermi levels and work functions of SCs, the charge carriers are redistributed at the junctions between SCs.

4.1. Computational Modeling and Methods

The study of complex interfaces through first-principles methods are well suited as such simulation do not require any feedback from experiments and are even not limited to a particular group of materials. Most of the first-principles methods are used in photocatalytic water splitting studies based on DFT,[186–188] whose practical applications depend on approximations for the exchange-correlation potentials V_{xc} and are referred to as electron–electron interactions. Among several approximations, the GGA[189] and LDA are the most popular ones. GGA mostly gives an accurate ground-state property of solids, even though some better approximations are needed when dealing with some complex problems including a description of response functions to external electromagnetic fields.[190] Furthermore, molecular dynamics (MD) can be combined with DFT known as first-principles molecular dynamics (FPMD) that can provide an ideal tool to deal with dynamics and thermodynamics properties of heterojunction interfaces.[191] Recently, a wide variety of complex chemical processes has been investigated at heterojunction/water interfaces, such as dissociation of water, surface HER, and OER, the spectroscopic signatures of important intermediates species including vibration,[40,192] and X-ray spectroscopic evidence.[193]

Many-body perturbation theory also called the GW approximation offers a promising mean due to its characteristics to tackle the interfaces, the electronic structures, and the interactive solvent such as water on the same footing.[194] In addition, with the recent advances in algorithms, GW calculations have enabled us to deal with the thousands of valence electrons, therefore, making it possible to compute the realistic electronic properties of photocatalysts/water interfaces. Coupling of large-scale GW calculations with the FPMD is a promising technique to study the electronic states of complex heterojunction structure and water molecules that are mutually altered at the interface and, therefore, can investigate the crucial role played by specific local intermediate species that are useful in determining the interfacial charge flow. The combination of such coupling explains the obvious effect of solvent and consequently, allows the researcher to deal with the general approximation used in the literature such as the calculation of photocatalytic reactions on dry surfaces.

The redistributions of charges at the interface and their particular transfer to the respective bands can be predicted from the calculated work function. While in the real junction, the Fermi levels always tend to be aligned when the two materials are in equilibrium. In contrast, when different Fermi levels of two different materials are connected, the electrons from the higher Fermi level move to the lower one. To understand the charge transfer within the junction and to the surfaces, the theory can be extended to model a system for the purpose to predict the behavior of electron flow, the thermodynamics requirements that help in the prediction of the band offsets, and the nature of junctions that provide an understanding of the charge separation abilities in an inclusive Z-scheme setup. To deal with such a system, the section explores the applications of computational techniques, their challenges especially the DFT-based calculations to comprehend the role of Z-scheme in photocatalytic water splitting.

Apart from a predictive perspective, computational and theoretical understanding advanced our approaches to various aspects of states. For example, the comprehensive study conducted on $BiVO_4$ investigated the density states, band structures, electron-hole generation, and migration to the surface chemical reaction.[195] It has been explored that electrons and holes are shifted to different crystal facets of $BiVO_4$ which are studied through comprehensive computational methodologies.[196] Commensurate with these studies, a more detailed discussion follows in the following sections.

4.2. Simulation of Internal Electric-Field and Interface Charge Carrier Flow

Both the interface formation energy and surface energy contribute substantially to the performance of the Z-scheme photocatalytic system. For example, it has been evident from the Liu et al. findings that the internal electric field (IEF) formation between the two components, TiO_2 and g-C_3N_4, is necessary to facilitate the charge transfer efficiency in direct Z-scheme.[197] They have chosen the TiO_2 (100) surface to construct TiO_2/g-C_3N_4 heterojunction owing to its highly reactive nature. They have synthesized the first 4×2 monolayer component of g-C_3N_4 and 4×1 of the TiO_2, shaped the heterojunction layers, and then simulated the whole structure of TiO_2 and g-C_3N_4. The formation energy of the TiO_2/g-C_3N_4 interface was found to be –1.16 eV, which indicates a stable interface formation for efficient charge transfer between g-C_3N_4 and TiO_2. The difference of the charge density has been calculated to get a clear picture of charge transfer in TiO_2/g-C_3N_4 heterojunction. The charge carrier redistributes at the interface between TiO_2 and g-C_3N_4. However, a negligible change in the charge density has

been observed in TiO_2, which might be because of the feeble interface energy between TiO_2 and g-C_3N_4.

Although Z-scheme heterojunction has the unique potential of charge-carrier transfer pathway, however, the charge-carrier migrations at the nanometric heterojunction interface remain an open challenge. For example, the ln-O-Cd bond has been introduced at the interface between CdS and $ZnIn_2S_4$ nanosheets via a cation exchange method.[198] As a result, the type-II band structure was successfully converted to Z-scheme. To confirm the role of ln-O-Cd in the Z-scheme formation, the DFT calculation has been performed.[199] The calculated work functions of CdS (002) and $Znln_2S_4$ (008) without ln-O-Cd bond are found to be 5.125 and 5.338 eV, respectively. Consequently, the Fermi level of CdS(002) is relatively more positive than the $Znln_2S_4$ (008) surface, and therefore, at the Fermi equilibrium, the charge carriers follow the traditional type-II charge transfer pathway. After the introduction of oxygen atoms into the $ZnIn_2S_4$/CdS heterojunction, the work function of $ZnIn_2S_4$-xOx/CdSOx dramatically decreases to 4.868 and 5.096 eV, respectively, which might be due to the stable ln-O-Cd bonds formation (**Figure 18**a,b). In the end, the work function of the $ZnIn_2S_4$-xOx (008) surface becomes more positive than the CdSOx (002) surface, and when the surfaces get into contact, the electrons readily transfer from $ZnIn_2S_4$-xOx (008) to CdSOx (002) surface to establish the Fermi level equilibrium. The region at the interface between $ZnIn_2S_4$/CdS heterojunction is charged, generating an internal electric field directing from $ZnIn_2S_4$ to CdS (Figure 17c), which significantly enhances the charge migration at the interface. Furthermore, the energy bands edge with high Fermi level bend upward in $ZnIn_2S_4$, and those in CdS with low Fermi level bend downward in the interface. Hence, the study suggests that the photogenerated charge carriers follow the direct Z-scheme pathway.

The observed charge-density difference of planar-averaged in Z-direction suggested that the charge carriers follow the Z-scheme route.[197,200] The electrons from g-C_3N_4 tend to shift to TiO_2 through the interface and leave the holes in the VB of g-C_3N_4. The process of charge diffusion between TiO_2 and g-C_3N_4 progressively continues until equilibrium is established. The charge carrier accumulation leads to the development of an internal electric field at the interface of heterojunction, which can push the photogenerated charges towards the g-C_3N_4. The creation of the IEF, in turn, speeds up the disconnection of charge carriers across all the TiO_2/g-C_3N_4 interfaces.

To demonstrate the direct Z-scheme, the description of the work function difference between the two SCs is a prerequisite to probe the distribution of the charges at the interface and create a built-in electric field.[197,201] For example, Ren et al. explored the properties of PtS_2/Arsenene(Are) van der Waals heterostructure for HER and OER of water splitting (**Figure 19**).[186] The work function of PtS_2 (W1 6.996 eV) and Are (W2 5.783 eV) have been calculated before the PtS_2 and Are were in contact. As the W1 is larger than W2, the electron moves from Are to PtS2 until equilibrium is established with the proper alignment of the Fermi level following Anderson's rules.[202] The electrostatic induction effect is created which generates negative and positive charged effects on PtS_2 and Are, respectively. This leads to the formation of a built-in electric field at the interface of the PtS_2 and Are. The negative charges in the Are sheet are repelled by the electron in the PtS_2 causing the upward band bending in the Are and the downward band bending in the PtS_2.[98,202] Only those electrons in the Are which have acquired sufficient energy, can cross over the potential barrier and migrate to PtS_2. However, the presence of a potential barrier in combination with the built-in-electric field can hinder the relocation of photoinduced electrons commencing from the Are and moving towards PtS_2. The same mechanism is followed for the migration of photoinduced holes from the VB of PtS_2 to the VB of Are. Further to the potential barrier, the electron (CB of Are) and hole (VB of PtS_2) recombination are highly suppressed because of the built-in electric field and the spatial separation of charges. Other system such as TiO_2/g-C_3N_4 can also form Z-scheme heterojunction due to built-in-electric field.[197] The DFT results indicated that due to interfacial interactions between TiO_2 and g-C_3N_4 surface, a built-in-electric field is generated which caused the charges to redistribute between the SCs, whereas under the light irradiations, the formation of such an electric field promotes the electron transfer from the CB of TiO_2 to the VB of g-C_3N_4, establishing the Z-scheme system.

The characterization of the Z-scheme is still a challenging task, both experimentally and theoretically. Especially, in theory, the band edge potentials and the built-in-electric field are not enough to understand the complete picture of charge transfer mode at the interface. For example, the heterostructure between $BiVO_4$ and phosphorus is established to be a direct Z-scheme via experimental technique; however, the

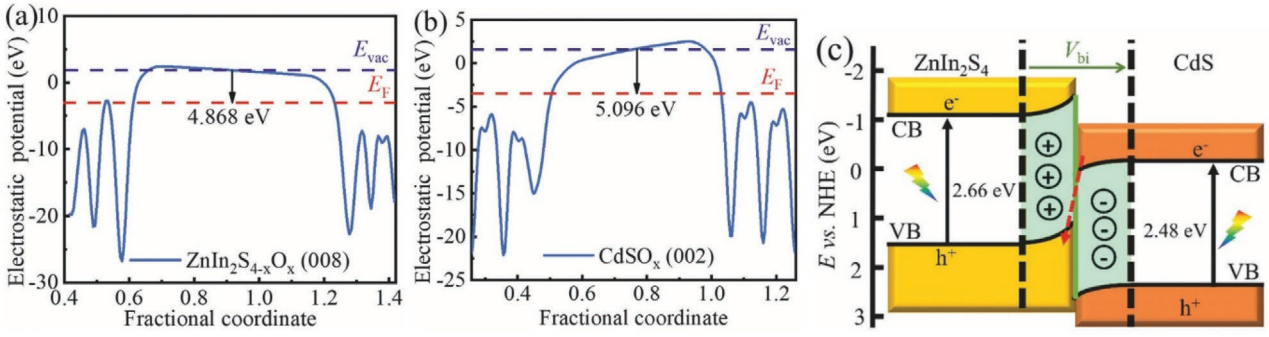

Figure 18. a) Electrostatic potential illustration computed through DFT for $ZnIn_2S_4$–xOx (008) surface and b) CdSOx (002) surface, and c) the charge carrier migration schematic illustration in Z-scheme $ZnIn_2S_4$/CdS heterojunction. Reproduced with permission.[199] Copyright 2019, Wiley-VCH.

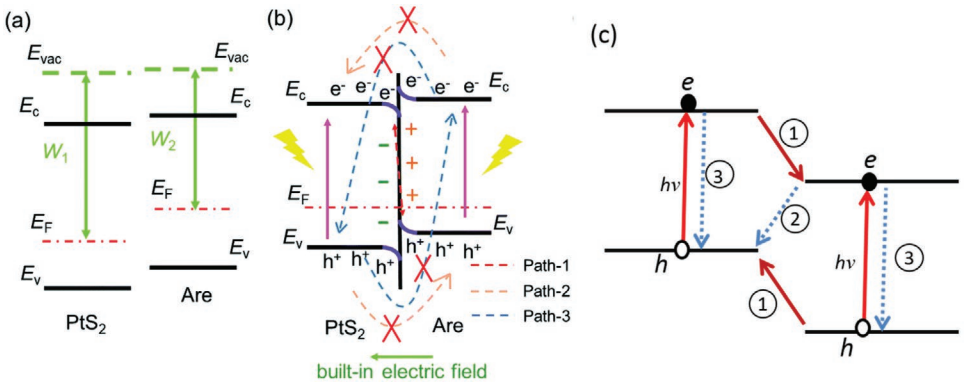

Figure 19. Schematic illustration of direct Z-scheme PtS_2/Are vdW heterostructure: a) before contact, b) photoinduced charge carrier illustration after contact. Reproduced with permission.[186] Copyright c) Schematic diagram of photoexcitation and charge transfer dynamics 1) between heterostructure, 2) interlayer e–h recombination, and 3) intralayer e–h recombination. Reproduced with permission.[40] Copyright 2018, American Chemical Society.

same heterojunction is identified as a type-II via theoretical analysis.[203] This opens a new window to explore another way such as nonadiabatic molecular dynamics (NAMD) to understand the dynamic behavior of photogenerated charge carriers at the interface. The NAMD can effectively predict the charge transfer dynamics of 2D direct Z-scheme such as PtS_2/Are and TiO_2/g-C_3N_4 which, however, cannot be studied through the traditional DFT method. In particular, such simulation can be used to investigate the charge transfer pathway to predict the mechanism; whether it follows the traditional type-II or Z-scheme pathway. For example, based on the charge transfer route, Zhao et al. performed NAMD simulation and reported that 2D BCN/C_2N follows direct Z-scheme owing to its ultrafast interlayer charge recombination (process 2) as compared to the interlayer charge recombination (process 3)[40] (Figure 18b). To this end, if the lifetime of process 2 is shorter than process 1 and 3, the probable route would be the Z-scheme pathway, otherwise, it follows the type-II phenomenon.

For example, Niu et al. have determined the dynamic of charge carriers at the interface of C_3N/C_3B heterojunction.[204] It is necessary to quantify the nature of the transportation of charge carriers in the Z-scheme. Their study revealed the NAMD calculations based on the reside charges on the respective bands, for example, holes in VBM of C_3N and electrons in CBM of C_3B. The calculated lifetime of photogenerated charges was defined for which the electrons of the CBM of C_3N recombine with VBM of C_3B. In contrast, as the charges of the respective bands (strong redox ability with weak redox ability) were relaxed to allow the transfer of electrons from the CBM of C_3N to the CBM of C_3B, but, no such transport was observed, suggested that the process follow Z-scheme pathway. They have also simulated relaxation time and observed that the lifetime (0.5 ps) of C_3B electrons recombination with the C_3N holes was relatively faster than the electron of C_3N with the C_3B holes, which further validated the Z-scheme idea.

It is noteworthy that the dynamics of the excited state not merely confirm the Z-scheme pathway developed on the ground state theoretical approach but also attain the time span of photogenerated charge carriers' recombination.

4.3. Effective Mass Calculation

To investigate the charge generation and charge migration of a particular photocatalytic system, the analysis of the effective masses of charge carriers through first principles simulation using DFT is considered an effective modeling technique. According to Yu et al., the simulation of connected materials gives insight into the formation of the Z-scheme system.[176] Based on DFT, the study at first reveals the attainment of the electronic band structure of the ZnO/g-C_3N_4 and second, it calculates the effective masses of the charge carrier of both SCs through the parabolic fitting of their CB and VB maximum (Equations (4) and (5)).

$$m^* = \hbar^2 \left(\frac{d^2E}{dk^2} \right)^{-1} \tag{4}$$

$$v = \hbar k / m^* \tag{5}$$

where $\hbar$ represents the reduced Planck constant, d^2E/dk^2describes the coefficient of the second-order term for the quadratic fit of $E(k)$ curves of the band edge, k denotes the wave vector, m^* signifies the effective mass of charge carrier, and v represents the transfer rate of charge carriers.

Notably, the transfer of the charge carrier is indirectly proportional to its effective mass. It implies that the lesser the effective mass of the charge carrier, the quicker is the charge carrier transfer. In addition, to the above equations, the separation rate of the charge carrier can be calculated by using Equation (6).

$$D = m_h^* / m_e^* \tag{6}$$

From the estimated effective masses of charges, the separation rate in both D-F and G-Z directions can be easily predicted (**Table 3**). The effective mass of electron in the G-Z direction of ZnO (0.034) is notably less than g-C_3N_4 (3.9), suggesting that the transfer of electrons of ZnO have much tendency in the G-Z direction than the g-C_3N_4 at the interface of the heterojunction, which infers the intrinsically feasible movement of the charge carriers that follow the Z-scheme pathway.[21]

Table 3. The calculated effective masses of the photogenerated electron and holes through the parabolic fitting of the CB and VB minimum for ZnO and g-C_3N_4, where, m_e*, m_h*, *and D* denotes the effective mass of electron and holes and m_h*/m_h*, respectively.

Species	Effective mass	G-Z direction	G-F direction
ZnO	m_h*	0.72	10.3
	m_e*	0.034	0.9
	D	20.9	11.5
g-C_3N_4	m_h*	29	0.64
	m_e*	3.9	0.41
	D	7.4	1.6

The determination of the charge transfer pathway through the calculation of effective masses is crucial to understand the type of mechanism. For example, Yu et al. performed a DFT calculation on g-C_3N_4/WO_3 to calculate the effective masses of charge carriers for the purpose to understand the charge transfer mechanism.[121] Their findings indicate that charge carriers move only via the 2D plane of g-C_3N_4 due to the delocalization of the π electrons. As compared to the g-C_3N_4, the excited electrons in WO_3 first migrate to the bulk and then transfer to the g-C_3N_4 through the interface which is strong evidence for the Z-scheme pathway.

As has been evident from the previous studies that the hole transfer is very important for OER in CdS-based photocatalysts.[205] The effective mass calculation of holes can provide quantitative evidence of their transfer along a specific direction. Particularly in photocatalysis, the transfer of holes to active sites is easy with smaller masses. Ju et al. studied such behavior in CdS and calculated the effective mass of holes (m_h*), fitting parabolic function to the VBM of CdS nanotubes.[206] The effective mass of the planar CdS has also been calculated along with the specific direction and compared with CdS nanotubes. The effective mass of the holes m_h* in the CdS nanotubes was found smaller than the planar one which reveals higher efficiency of the hole transport for the OER in the Z-scheme system. Furthermore, the effective masses of the electrons (m_e*) for these two systems have also been compared, whereas m_e* of CdS nanotubes is found to be larger than planar. This can be rationalized by the fact that CdS nanotubes have large proportions of the s and p orbitals in their lowest CB, whereas for the planar CdS, the s and p orbitals (in the lowest CB) are very less. It indicates that CdS nanotubes with larger electron effective mass have probably poor HER photocatalytic activity than the planar CdS monolayer.

4.4. Natural Band Offsets Theoretical Predictions

The computational technique using DFT has gained a substantial addition in modeling science due to its highly accurate prediction of the band offsets of some important materials at a relatively low cost.[207] The use of this technique[184] has gained a prominent position in photocatalysis; therefore, the Z-scheme photocatalytic water splitting has been considerably investigated through DFT in recent years,[184,187,208] whereas the accurate description of the band offsets of interacted materials is crucial to understand the complex inner electronic chemistry. For instance, Chao et al. have studied the band offset of In_2O_3 and $ZnIn_2Se_4$ by DFT.[209] The corresponding molecular structures of In_2O_3 and $ZnIn_2Se_4$ are shown in **Figure 20**. The calculation predicts that the bottom of CB of the In_2O_3 mainly consists of the ln 5s and O 2p state while the uppermost of the VB consists of the O 2p state. In $Znln_2Se_4$, both the CB and VB bottom consist of ln 5s and Se 4p states. Owing to the difference in electronic states, the VB of $Znln_2Se_4$ is relatively more positive than the In_2O_3. It suggests that the ln_2O_3 possesses a strong oxidizing ability in the water-splitting reaction. While the location of the CB of both materials are nearly positioned in the same region, however, it can be inferred that in the In_2O_3-$ZnIn_2Se_4$, the In_2O_3, and $ZnIn_2Se_4$ act as oxidizing and reducing sites, respectively.

The g-C_3N_4/TiO_2 heterostructure and its band structure have been calculated to investigate its significant photocatalytic performance following the Z-scheme pathway[197] with a special focus on a deep exploration of the band charge densities of the heterostructure. The CB minimum of this heterostructure revealed favorable occupation by Ti orbital, whereas the VB minimum is occupied by the C and N orbitals. Hence, both bands were found to be occupied by different constituents in the g-C_3N_4/TiO_2 heterostructure.

Shen et al. studied the band structure of CeO_2/$W_{18}O_{49}$ heterojunction to understand the metal types and bonding strength.[210] The bandgap of CeO_2 and $W_{18}O_{49}$ has been estimated as 1.85 and 0.59 eV, respectively, although the theoretical bandgap calculated by DFT is often narrower than the actual bandgap. Based on their results, the s, p, and d orbital of O and Ce almost overlap with each other which indicates the strong bonding effect between them. Also, some covalent bond behavior has been observed between W-O which may be due to the pseudogap between the atoms. From these observations, occupied orbital by the particular band in each material has also been calculated. Specifically, the VB of CeO_2 is mainly occupied by the p and d orbitals, whereas the contribution from the s orbital was more to the CB, while, in $W_{18}O_{49}$, the VB and CB were found to be occupied by both d and s orbital, respectively.

To find a suitable 2D structure with an energy band that is compatible with the CdS to attain proficient H_2 production from water is widely investigated.To this end, Bi_2MoO_6 is used as a potential contender for visible driven photocatalysis which is a layer Aurivillius oxide SC composed of $Bi_2O_2^{2+}$ and MoO_4^{2-} layers with a relatively narrow bandgap (2.60 eV).[211] Lv et al. has calculated the density of states as well as the energy band structure of the CdS and Bi_2MoO_6 using the DFT method.[212] CdS is listed as direct bandgap SC as both the CBM and VBM are present at the same high symmetry point G, while Bi_2MoO_6 is an indirect bandgap material whose VBM has been observed at G point whereas the CBM at P point along SX direction.[213] They have calculated the bandgap of CdS and Bi_2MoO_6 as 1.30 and 1.90 eV, respectively. It should be noted that the calculated bandgap is much narrower than the experimental value (2.62 eV for Bi_2MoO_6 and 2.34 eV for CdS) due to the limitation of the GGA function.[214] According to the density of states, VB and CB of CdS are mainly occupied by 4s 3p, with a little content of Cd 5s, 4p orbitals.[212,215] Furthermore, the 4s 3p orbitals enable the positioning of the CB edges and narrowing

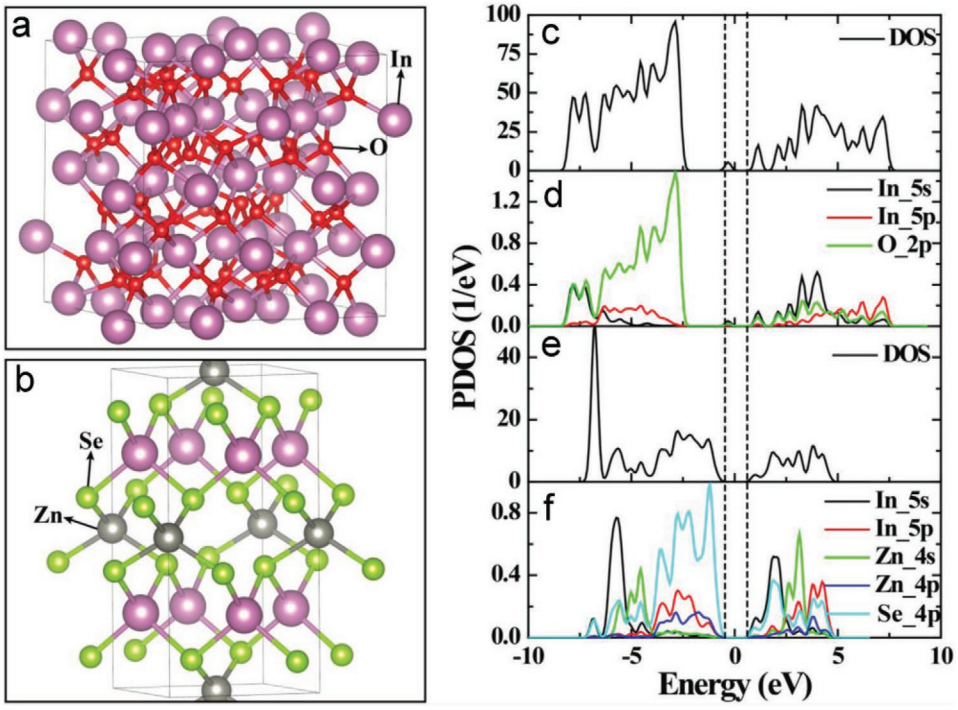

Figure 20. Optimized geometry structures of a) In_2O_3 and b) $ZnIn_2Se_4$, and c–f) the corresponding density of state (DOS) plots. The dashed line represents the Fermi level. All electronic states were normalized by the deep In 4d states. Reproduced with permission.[209] Copyright 2019, Wiley-VCH.

the bandgap. The VB and CB of Bi_2MoO_6 are composed of O 2p and a Mo 4d, Bi 6s, 6p.[212]

4.5. Mechanistic Investigation of the Water-Splitting Process

As it has been demonstrated earlier, strongly built-in-electric field and non-adiabatic coupling occurring at interface efficiently hinder the charge separation and backward reactions.[204] To effectively drive such a redox mechanism, the charge carriers ought to straddle with the water redox potentials. Furthermore, to establish the complete redox process, the compatibility of the band edge potential of the heterostructure to the redox potential of H_2O/O_2 and H^+/H_2 is crucial.[216] Both the O-O bond formation and the proton-coupled-electron-transfer mainly depends on the participating-transition metal[217] and reaction media[218] and hence, it is very difficult to predict the mechanism due to ambiguity in the thermodynamics and kinetics of the process. Unfortunately, O-O bond formation is highly affected by the small fluctuation of the local environment and very little by the electrical potentials.[219] A detailed discussion follows in the following sections.

4.5.1. Modelling Thermodynamics Overview and Surface Chemical Processes

Water splitting reaction is not a concerted process; however, it proceeds through several intermediate species.[96,219] To enumerate the intermediates, a mechanism is needed to be proposed. To know the relative stability of these proposed intermediates, the thermodynamics stability needs to be calculated, which in turn depends on both catalytic mechanism and nature of the catalyst surface. Although the overall water splitting requires a potential of 1.23 eV per electron transferred, [220] individual steps may precede a potential thermodynamically uphill that has a high energy barrier. Such steps determine the kinetics of the reaction where the largest barrier determines the rate-determining step of the entire cycle. If, however, we ignore the activation energy (assuming it is small), then the overpotential of the mechanism is entirely determined by thermodynamics. In such a case, the overpotential is often underestimated but still, it provides enough estimation without reviewing the kinetics of the reaction.

Static calculations based on DFT are extensively performed to study the interaction between water molecule and photocatalyst, specifically at the low convergence limit. Although, for a few adsorbed water molecules, it is possible to optimize several configurations; however, this strategy is not suitable for complex heterojunction structures where water has multisite for adsorption. These limitations may considerably affect the results obtained for a system such as Z-scheme heterojunction which needs theoretical feedback from the heterojunction band edges water interfaces, requiring various water adsorption sites for convergence.

As discussed earlier, the consumption of photoexcited carriers for the HER and OER at the surface of the catalyst ends the water-splitting reaction. The kinetics of the HER and OER processes has a profound effect on the performance of the photocatalyst.[19] In particular, the thermodynamically uphill water-splitting reaction requires a high activation barrier which often results in low activity. The OER reaction is considered

kinetically slow-moving owing to the multistep proton-coupled electron transfer procedure.[221] The transient absorption study shows that OER is much slower (second-time scale) than the HER (microsecond scale).[222] The mechanism of the OER reaction proceeds with the consumption of four electrons as illustrated below (Equations (7)–(10)):

$$H_2O(l) + * \rightleftharpoons HO* + H^+ + e^- \quad (7)$$

$$HO* \rightleftharpoons O* + H^+ + e^- \quad (8)$$

$$O* + H_2O \rightleftharpoons HOO* + H^+ + e^- \quad (9)$$

$$HOO* \rightleftharpoons * + O_2(g) + H^+ + e^- \quad (10)$$

Here, the * denotes active sites where the catalytic reaction occurs, and OOH*, OH*, and O* represent the chemisorbed species located at active sites. First-principles DFT calculation has confirmed that the lowermost theoretical overpotentials for the OER process are described by a constant difference between binding energies of OOH* and OH*.[223] The binding of these species to the surface through a single bond via O atom defines the origin of their scaling relationships, whereas, the corresponding binding energies generally show a slope of 2 on a linear scale that is because of the formation of two bonds by O* with the surface.

Some catalysts are capable to work at this minimum theoretical overpotential, but most of the catalysts such as rutile, spinel, perovskite, bixbyite oxides require an extra overpotential created by the O* binding energy, which is potentially considered to be a rate-determining step. Consequently, the overpotential of OER is calculated as ΔGO* –ΔGHO*.[224,225] The HER is proceeding either through Valmer–Tafel or Volmer Heyrovsky mechanism via hydronium ion reduction as shown in Equations (11)–(13).[226]

$$(\text{Volmer})\, H_3O^+ + e^- + * \rightleftharpoons H* + H_2O(l) \quad (11)$$

and

$$(\text{Heyrovsky})\, H* + H_3O^+ + e^- \rightleftharpoons H_2(g) + H_2O(l) + * \quad (12)$$

Together with

$$(\text{Tafel})\, 2H* \rightleftharpoons H_2 + 2* \quad (13)$$

Considering the HER, the M-H bond strength is often treated as an atomic-level activity descriptor where M represents transition metal.[227] The free energy diagram for the HER and OER indicated that for the HER the rate-determining step is the generation of H*, while for the OER the formation of OOH* state is considered the key step in the case of Volmer–Heyrovsky mechanism (**Figure 21**).[225] However, there are contradictory reports regarding the rate-determining step of the HER in literature,[228] suggesting that different active sites of the metal catalysts pursue different reactions.

The adsorption of reactant species on the catalyst surface is the key step of any catalytic process. Niu et al. studied the mechanism of water splitting on C_3N/C_3B heterostructure and investigated the adsorption capability of the heterostructure for water molecules.[204] The adsorbed water molecule on the surface of such heterostructure is depicted by **Figure 22**a which shows a distance of 1.78 Å between B and O. This ruled out the physisorption of a water molecule (≈3 Å) on the catalyst. In addition, the calculated binding energy between the C_3N/C_3B and water is found to be –0.6 eV, as derived from the attraction between empty orbitals (Lewis acid sites) and the lone pair (water). This attraction eventually causes a substantial charge migration in the system. As depicted in Figure 22b, the charge density difference caused by the adsorbed water C_3N/C_3B system indicates that the empty orbital of B can trap the lone pair electrons of water which justifies the Z-scheme system in C_3N/C_3B. In addition, the adsorption of water molecules on the C_3N sub-layer of C_3N/C_3B has been performed where the distance between N and H was found to be 2.56 Å. The binding energy of –0.07 eV is noted which is less favorable than H_2O

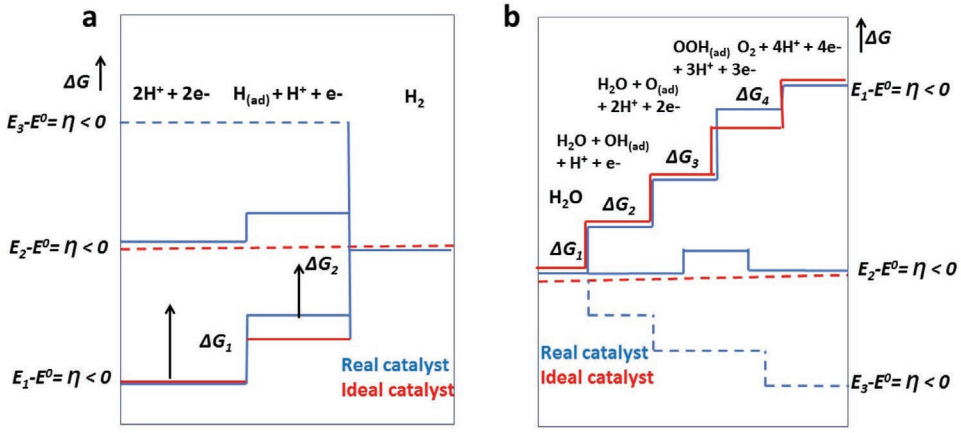

Figure 21. Plots of Gibbs free energies of reactive species and the chemisorptions of intermediates (horizontal lines) versus the reaction coordinate of a) the HER and b) OER. Blue lines and red lines indicate energetics of a typical (real) catalyst and ideal catalyst at three different electrode potentials (E_1, E_2, E_3), respectively. Dashed lines indicate energetics at the electrode potential at which all thermochemical barriers disappear. ΔG notes the free reaction energy of the two elementary reaction steps. The red case corresponds to an overpotential-free catalyst. E° denotes the standard reversible electrode potential of the HER, η is the overpotential. Reproduced with permission.[225] Copyright 2010, Wiley-VCH.

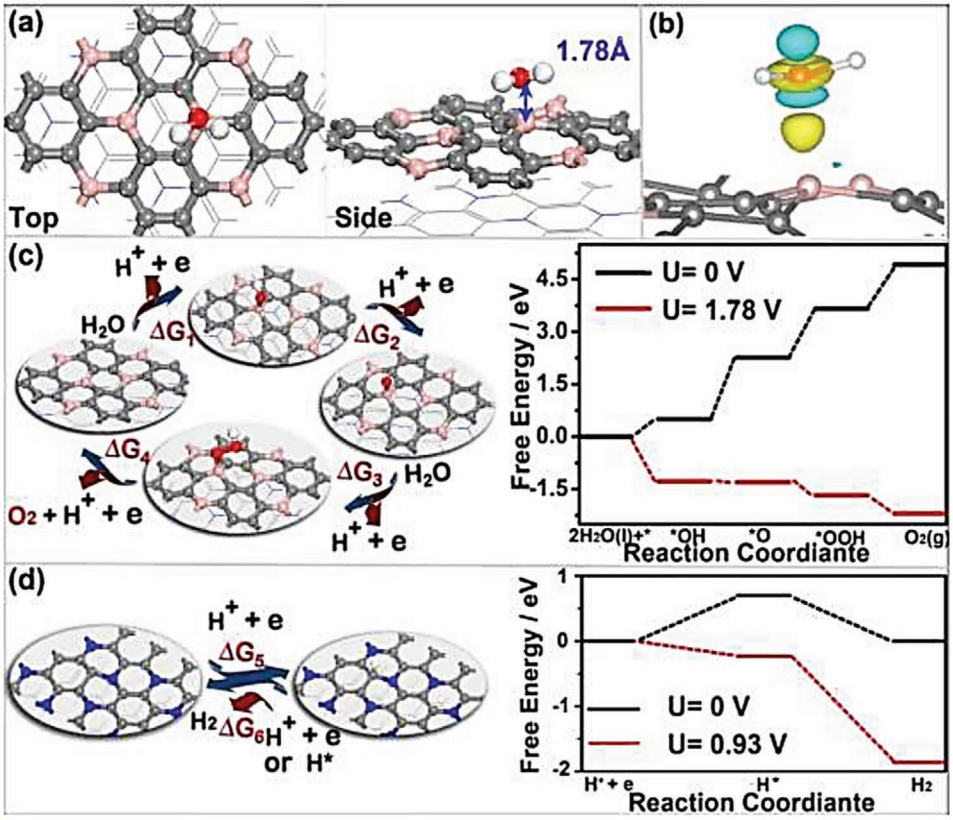

Figure 22. a) Water adsorption on the C_3B sublayer of C_3N/C_3B heterostructure from the top and side views. b) The charge density difference with the iso value is 0.008 e/Bohr^3; blue and yellow regions represent the *e* depletion and accumulation, respectively. c) The reaction steps of water dissociations and free energy diagram denoted water oxidation (four-electron process) and hydrogen reduction (two-electron process). d) The adsorption states of each species such as *OH, H*, *O, and *OOH with the corresponding reactions. The photogenerated electron/provide external potentials U = 1.78 (0.93) V for water oxidation (hydrogen reduction) reaction. Reproduced with permission.[204] Copyright 2020, American Chemical Society.

adsorb on the C_3B site. This may be due to the weak interaction between the vacant N orbital and the lone pair electron of water.

To further validate the redox process of H_2O through effective consumption of photogenerated charge carriers, the H_2O oxidation and hydrogen reduction half-reactions are systemically investigated. First, the complex OER process is studied as shown in Figure 22C. The H_2O molecule dissociates into OH and resides as adsorbed species on the surface as *OH of the photocatalyst. Further, dissociation of *OH into *O occur followed by reaction with additional H_2O molecule and produces OOH* species, eventually leading to the O_2 evolution. Based on the calculated Gibbs free energy (ΔG: the sum of the difference between chemical potentials of product and reactants) for every elementary step, the essential overpotential for the OER can be calculated.[223,225] The dissociation of the adsorbed OH* species into *O on the surface of the C_3N/C_3B is the rate-determining step (ΔG_2 = –1.76 V), which is depicted as a black line. This suggests that the OER process is energetically not feasible without light irradiations. Notably, when taking into account the external potential of photo-generated holes, the dramatic downtrend in the four elementary steps of the OER in the free energy diagram is observed, which shifted the energy of $-eU$ (U_e = 1.78 V). This verified that C_3N/C_3B heterostructure can catalyze the water oxidation process under light irradiations. On the other hand, the HER reaction occurs on the C sites of the C_3N, and therefore, can infer that the photocatalytic efficiency can be improved this way due to different sites for the HER and OER processes. As shown in Figure 22d, the H* generation in the absence of light (U = 0 V) is also energetically unfavorable (ΔG = 0.7 eV). However, once the effect of photogenerated electrons is added, the trend again shifts towards a lower value for the corresponding elementary steps of HER suggesting a potential of U_h = 0.93 V. Therefore, the overall photocatalytic water splitting process on C_3N/C_3B heterostructure is deemed feasible.

4.5.2. Interplay of Charge Transfer and Chemical Reactions

$BiVO_4$ is an excellent photocatalyst used for water oxidation owing to its suitable band edge position; however, the charge recombination issue hampers its effective charge transportation.[229] Recently, the heterojunction of a $BiVO_4$ with other SCs has been studied through DFT;[230] the efficiency of such materials can be further improved in the presence of metal-doped materials such as Cr and B codoped g-C_3N_4/$BiVO_4$.[231] A systematic theoretical study such as the hybrid DFT approach can explore the photocatalytic mechanism as performed by Wang

et al.[231] The authors have first developed face-to-face g-C_3N_4/$BiVO_4$ heterojunction which comprised g-C_3N_4 and $BiVO_4$ (010) surface, since this junction can incorporate a built-in-electric field that can promote charge transportation at the interface. Under light irradiation, the CB electrons of $BiVO_4$ are readily excited and are utilized in HER, while the holes in the VBM of g-C_3N_4 undergo OER. A typical Z-scheme is established as the band edge potentials of $BiVO_4$ (010) are greater than those of g-C_3N_4 ensuring the transferral of electrons from the CBM of g-C_3N_4 to the VBM of g-$BiVO_4$. The existence of such a system has also been reported by other groups.[232] Moreover, the addition of Cr and B doping induces the Cr-3d and B-2p states which can lower the bandgap and in turn improve the light absorption capability of the hybrid system. The bandgap of B and Cr co-doped g-C_3N_4/$BiVO_4$ is relatively smaller than that of pure Cr-doped and B-doped g-C_3N_4/$BiVO_4$ heterojunction. The built-in-electric field is directed from the Cr-doped $BiVO_4$ to B-doped g-C_3N_4 since the electron from the CB of B-doped g-C_3N_4 transfers to Cr-doped $BiVO_4$. Conversely, the photogenerated holes on the VBM of the Cr-doped $BiVO_4$ surface tend to combine with the B-doped g-C_3N_4. In this way, the photoexcited electrons undergo a reduction of a proton to H_2 on the CBM of Cr-doped $BiVO_4$, whereas the holes in the VBM of B-doped g-C_3N_4 favor the OER. The incorporation of metal such as B to C_3N_4/$MoSe_2$ can not only change the undesirable type-I heterojunction into direct Z-scheme as reported by Ai et al.[233] but also effectively impede the charge recombination very effectively. The detailed analysis of the state density and charge density distribution along with the work functions of the B-doped C_3N_4/$MoSe_2$ shows proper built-in-electric field at the interface; whereas the tendency of the built-in-electric field pointing towards $MoSe_2$, suggesting a direct Z-scheme heterostructure.

Xu et al. developed a 2D/2D direct Z-scheme system that utilized the junction between Fe_2O_3 and g-C_3N_4.[136] The intimate contact between these two SCs with successful uniform deposition of Pt can be seen in **Figure 23**a,b. Such intrinsic contact is also confirmed through DFT calculation that revealed g-C_3N_4 with a higher Fermi level and lowers WF (4.18 eV) as compared to Fe_2O_3 (WF = 4.34 eV). Subsequently, a band alignment having a configuration of direct Z-scheme is created within heterostructure; where electron resides in the CB of g-C_3N_4 and holes accumulated in the VB of Fe_2O_3. Taking into consideration the band structures of Fe_2O_3 and g-C_3N_4 and there are two possible pathways for the charge carrier transport; the type-II heterojunction and the direct Z-scheme as shown in Figure 23c–e. Both CB and VB of g-C_3N_4 are positioned at 1.10 and 1.70 eV, respectively.[234] Consequently, as the Pt is doped on the g-C_3N_4 surface, the electrons probably move toward Pt. The bandgap energies of the Fe_2O_3 are 0.3 and 2.4 eV for the CB and VB, respectively, which can be computed through empirical formula.[235] Based on the low level of CB of Fe_2O_3, the CB electrons are thermodynamically incapable to reduce protons. Considering the photogenerated charges followed the traditional type-II mechanism. In such a case, the electrons from the CB

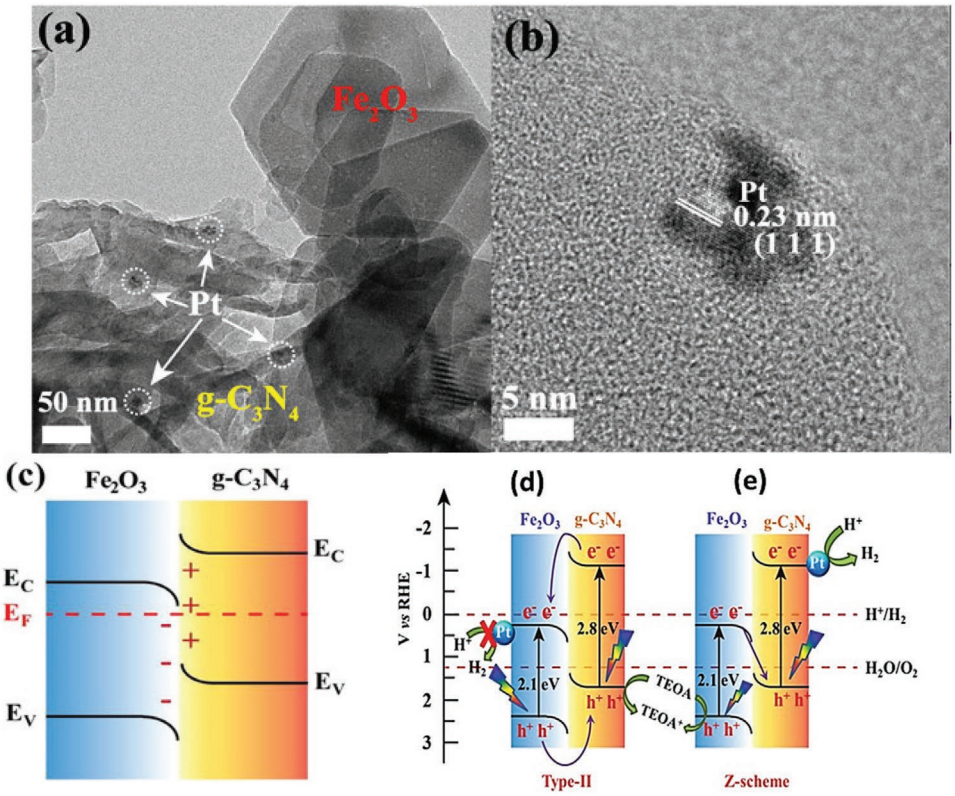

Figure 23. The a) TEM and HRTEM images of 10% Fe_2O_3/g-C_3N_4 composite loaded with 1wt% Pt, and b) the schematic illustration of the energy band offsets, the interface charge transportation, and the structural features of Fe_2O_3/g-C_3N_4 heterojunction: a) traditional type-II heterojunction and b) direct Z-scheme systems. Reproduced with permission.[136] Copyright 2018, Wiley-VCH.

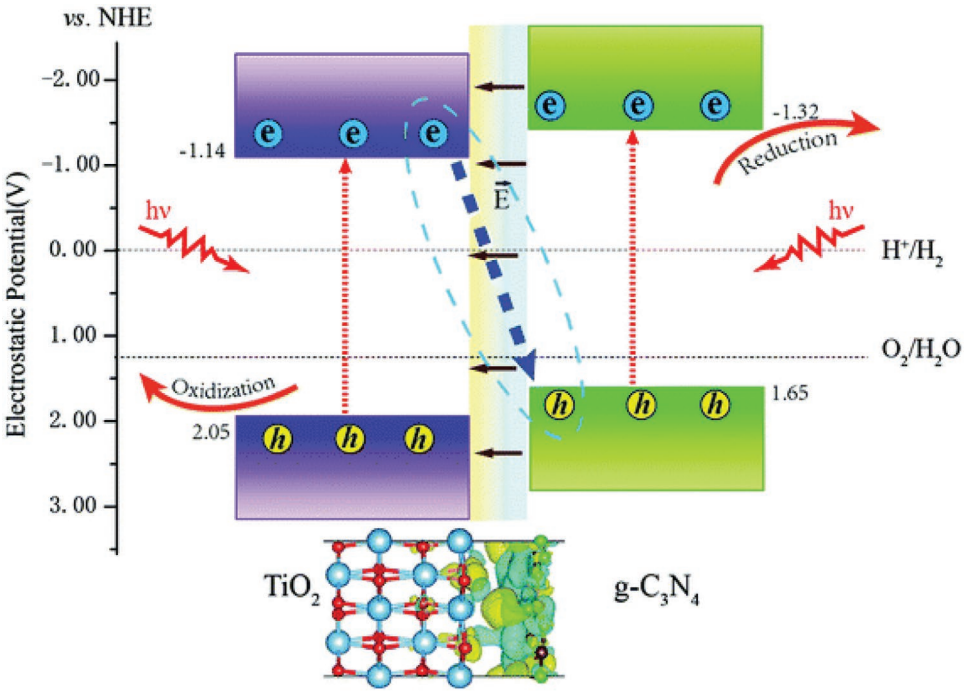

Figure 24. Proposed direct Z-scheme photocatalytic mechanism for the g-C_3N_4/TiO_2 heterostructure. Reproduced with permission.[197] Copyright 2016, The Royal Society of Chemistry.

of g-C_3N_4 would move to the CB of Fe_2O_3, while the holes from the Fe_2O_3 would transfer to the VB of g-C_3N_4. To this end, the photoactivity of the composite needs to be inevitably declined compared to the pristine g-C_3N_4. However, the case is opposite from the actual experimental results[136] that show enhanced photoactivity response for the composite, suggesting that the charge transportation follows the Z-scheme pathway.

Ju et al. explored the redox ability of GeS/WS_2 for the overall water splitting through DFT calculation.[187] They first calculated the CBM of GeS (1.32 eV), higher than the reduction potential of H^+/H_2, therefore, suitable for the HER. However, the VBM of GeS did not seem lower than the oxidation potential of H_2O/O_2 hence, not suitable for OER. On the other hand, the VBM of WS_2 (0.29 eV) is sufficiently found lower than the oxidation potential of H_2O/O_2, while CBM was found to be 0.37 eV, demonstrating its practicality for both OER and HER. Notably, the CBM of WS_2 1.31 eV is higher than the VBM of GeS which infers the prospect of charge migration between the CB of WS_2 and the VB of GeS which ultimately manifests the Z-scheme pathway.

Similarly, the g-C_3N_4 and TiO_2 heterostructure display a direct Z-scheme photocatalyst pathway as confirmed from the recent experimental findings.[125,236] Theoretical study also shows the interface charge flow and the mechanistic insight into the water-splitting process using g-C_3N_4/TiO_2.[197] Following the Z-scheme approach, the holes and electrons that reside in the VBM and the CBM respectively, exhibit strong redox ability as compared to traditional type-I and type-II heterostructure.[8,161] The electrons occupy the CBM of g-C_3N_4, whose CB edge potential is 1.32 V (vs NHE), negative enough than the reduction potential of a proton (H^+/H_2 (0 V). The photoexcited holes were collected in the VBM of TiO_2, and the calculated VB edge potential of TiO_2 is 2.05 V, which is sufficiently positive to oxidize the water molecule O_2/H_2O (1.23 V) to produce O_2 (**Figure 24**).

4.6. Advances in Machine Learning

Machine learning (ML), a subdivision of artificial intelligence (AI) is an emerging technology and promising tool to assist the resource-demanding experiments and computations in the material sciences through statistical models and algorithmic systems.[237] ML models the information based on provided data and offers a possible solution to address these tasks. The significance of AI has been recognized decades ago; however, one of the recent breakthroughs has been introduced through Dendral and Meta-Dendral programs, which provide an artificial level model to predict the structural elucidation of unknown materials based on the data from mass spectrometry.[238] Recent advancement in ML is the designing of materials/drugs,[239] which enables further developments in light-harvesting materials.[240] This is important as future studies would deeply investigate the hybrid materials such as heterojunctions materials, and the effect of doping on the reactivity of catalysts where ML can play a significant role to predict the performance of materials without performing DFT calculations.

One of the key applications of ML is the prediction of materials characteristics for water splitting. In this regard, the key methods are supervised learning and unsupervised learning. Through supervised learning, the targets are predicted from a set of inputs through a mapping strategy that projects the provided information to associated targets. For example, the prediction of charge-transfer excitation energies from the given molecular structures can be achieved through this method. To

this end, the ML model learns to envisage the possible targeted properties such as charge transfer excitations, if provided with the structures of materials and the local environment around the structures. On the other hand, unsupervised learning does not aim to predict the features, rather its focus is on assuming the probability distribution, reveal the pattern in the given data set, which can further be examined by the researchers. Indeed, an unsupervised approach has been recently employed for the optimization of multi-junction solar cells. In addition, the clustering strategies have been used to develop and design organic SCs, which assisted the in silico finding of some potential molecular structures with better charge-transfer mechanisms.[241]

4.6.1. Machine Learning for Predicting Water Splitting Materials

One of the important applications of ML is the predictions of excited states to investigate the dynamic of excitons in light-harvesting complexes, particularly novel materials for water splitting.[242] For example, Greeley and Norskov [243] performed large-scale DFT based screening of binary transition-metal alloys of around 750 samples for the HER, where they found several bulks and surfaces alloys that have comparable performance as Pt, and, hence, established the implementation of the DFT method for high-throughput screening.[244] Castelli et al. screened different cubic perovskite materials such as oxides, oxynitrides, oxysulfides, oxyfluoronitrides, and oxyfluorides employing DFT-RPBE to examine their stability for water splitting.[245] To this aim, the authors first calculated the band edges of these materials based on their bandgap and electronegativities. Secondly, they assumed that all materials have a cubic perovskite phase. The thermodynamics factor was not included in the stability study. Based on this assumption and analysis, a total of 15, 12, and 20 likely perovskite materials were selected from the oxyfluoride, oxynitride, and oxides families, respectively, owing to their maximum absorption capability of solar radiation and high charge mobility. To this end, they employed computational materials repository approach to search materials of desired properties.[246] Taking into account the accuracy and selection of the potential materials, future work could be more envision through combining various search repositories with DFT calculations.

To understand the effect of materials properties on water splitting, statistical regression methods have been widely performed. By employing factor analysis and linear regression approaches, Hong et al. established a statistical framework to envisage the OER activity of transition-metal oxides. They have grouped five categories as TM-ion electron occupancy, exchange interaction, metal-oxygen covalency, geometrical structure, and electro-statics which were based on the 14 physical descriptors.[247]

Recently, several efforts have been made to understand the activity of the materials for water splitting. For instance, Wexler et al. employed a regularized-random-forest-based machine learning method to investigate the significance of DFT-derived charge descriptors and structure to determine the HER activity of surface-non-metal-doped $Ni_2P(0001)$[248] (**Figure 25**a). They envisage the effect of surface non-metal doping on the HER activity over Ni_3P_2 termination of $Ni_2P(0001)$ using DFT calculations and found that both heavier chalcogens and 2p nonmetals offer nearly thermoneutral H_2 adsorption. Furthermore, chalcogen substitution for surface P is found to be exergonic. The relative importance and their description are depicted in Figure 25b, which indicates that the Ni-Ni bond length is an important descriptor to predict the HER activity over $Ni_2P(0001)$. In addition, the authors found a direct correlation between the average Ni-Ni bond length and energies of adsorbed H atoms. They concluded that the dopant-induced geometry changes for $Ni_2P(0001)$ are more vital as compared to the dopant's electronic character.[248] Tran and Ulissi established a strategy that combines automatic machine-learning-based optimization with DFT-RPBE calculations to selectively screen desired materials for HER.[249] They utilized this framework approach to investigate 258 contenders from 102 intermetallic surfaces which is suitable for HER. To be conclusive, each element was labeled by a vector comprising four numbers: Pauling electronegativity, atomic number, the adsorption energy, and the coordination number. Based on the adsorption energy of H, the activity of the chosen surfaces for the HER was quantified,[249] which suggested the potential of the machine learning stratagems to discover novel water-splitting materials. Recently, Back et al. studied the OER activity over different polymorphs and their facets via the automated high-throughput DFT-PBE method[250] as shown in Figure 25c. The authors used the recently established crystal graph convolutional neural network (CNN) strategy which is developed by Xie and Grossman.[251] Through this approach, the atomic structures along with their bonding information can be stored by a graph representation. They have identified several active sites on very low-index surfaces of IrO_2 and IrO_3 which have low overpotential (by 0.2 V) than the stable-rutile(110) surface of IrO_2.[250] In the future, other intermediates than the usual ones could be taken into consideration, along with focusing on both kinetics and thermodynamics e of the OER process.

4.7. Critical Remarks

Although computational studies have been widely used to assess the Z-scheme capabilities as an efficient route for the HER and OER of water splitting, yet these studies cannot completely capture all the aspects that can oversee the performance of the complex heterostructure system. Therefore, considerable assumptions are made to review this protocol for the purpose to minimize the loss of accuracy. The common assumptions include neglecting atom-atom interaction within heterostructure and its impact on the study of energetics bottlenecks. Through the development of efficient algorithms and the availability of large computational resources, more realistic calculations can be possibly made. The use of hybrid DFT studies has proven to be an important technique to get insight into the nature of the complex heterostructure, which can help to differentiate between type-II and Z-scheme pathways. However, the lack of uniformity in methodology for the construction of such a complex system and the simulation parameters can lead to hazardous ramifications such as the unrealistic representation of heterojunction and its host-guest relation with the reactant species such as H_2O which is not necessarily illustrative of the real system. Furthermore, some other limitations such as derivative

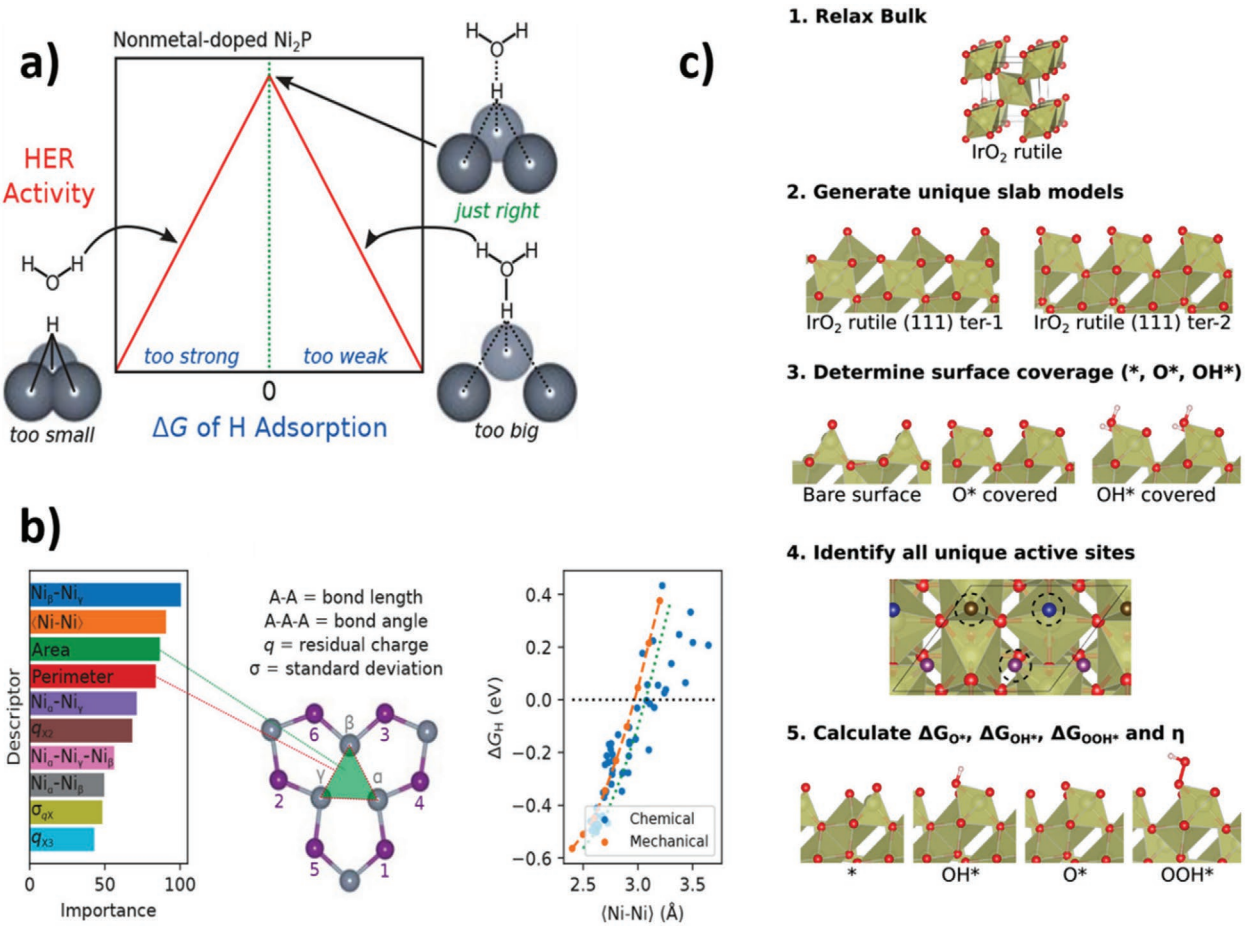

Figure 25. Machine learning: a) Effect of surface non-metal doping on the HER activity over Ni_3P_2 termination of $Ni_2P(0001)$, b) relative importance of descriptors calculated from RRF model. Only the top ten features whose definition of descriptors are shown in the inset. The three Ni atoms α, β, and γ are labeled based on their distance from the first doping site. The effect of average Ni–Ni bond length on ΔG_H as induced by chemical pressure and mechanical pressure. Green dotted line adjusts for Ni–Ni bond contraction upon H adsorption in the mechanical case, and c) workflow and atomic structure examples associated with each step to systematically investigate the OER activity of oxide materials. The (111) facet of rutile IrO_2 is shown as an example. Three different colors of oxygen atoms (gray, blue, and purple) in (4) indicate three unique active sites. Each unique oxygen atom is removed to generate bare surfaces, or H and OH were attached to the oxygen atom to generate OH* and OOH* adsorbed surfaces, respectively. Reproduced with permission.[248] Copyright 2018, American Chemical Society.

discontinuity V_{xc}, the self-interaction effect, and the long-range exchange and dispersion interactions error are needed to be overcome.[252] These limitations lead to several disagreements between experiments and simulations; the notable discrepancy found in the GGA based on FPMD simulations that over structuring the liquid water.[253] Furthermore, the GGA and LDA-based simulations are not well known to be used for excited-state properties due to their poor description for bandgaps and band edge predictions, and important properties of photocatalyst.[254] In most cases, the bandgap energy is underestimated; for example, Nashed et al. using different hybrid DFT functionals such as GGA and LDA to study the band structure of β-, δ-Ta_2O_5, and β-Ta_2O_5.[255] The bandgap energy of all structures is not only found to be different among different functionals but also underestimated when compared to the experimental value. Comparable results have been reported by Wu et al. for the bandgap study of the Ta_2O_5.[256]

The inaccuracies of GGA in the description of liquid water (at ambient conditions) could be mitigated by carrying out the simulation at high temperatures.[257] To reduce the self-interaction error, the simulation can be performed with the hybrid exchange-correlation functional[187,258] while the introduction of van der Waals interaction can add certain important factors to aqueous-based simulation such as water density,[259] as well as the description of several classes of SCs.[40,187,260,261] Notably, the simulation of interfaces under finite temperature employ hybrid functional is rare due to prohibited computational cost. Since some simulations are only limited to a very short timescale (few picoseconds) which are insufficient to extract meaningful data such as kinetic barriers and some other useful thermodynamic quantities important for the Z-scheme mechanistic investigations.[262]

There is still an open theoretical challenge to exploit the charge transfer mechanism but crucial to get insight into the charge migration pathway that can differentiate between type-II and Z-scheme heterojunction systems. The evaluation of the charge transfer mechanism through first-principles, still depends on approximate theories, therefore, a unified approach

can effectively describe the band transport. Also, hopping (polaron) on the same footing is much needed in application to the real system, which is a major challenge in predicting catalytic efficiency for a solar-to-fuel generation. Though many recent studies have been performed on electron transfer rate[263] composed of simulations, based on Fermi's golden rule and transition state theory that often predicts only a single process at a time.

Furthermore, DFT with semi-functional is unable to give an accurate description of the excited-state properties of the interfaces relevant to photocatalysis. The bandgap is often underestimated which leads to misinterpretation of the charge transfer at interfaces. This error can be minimized by using hybrid functionals[264] known as DFT+U where U represents the Hubbard correction.[265] However, it can only be used for single materials; therefore, it is unable to describe the complex system such as heterojunction between two SCs where each SC has a different bandgap.[266,267]

Although DFT has no doubt play a key role in computational catalysis, it is, however, important to note that as an approximate method there are inaccuracies in calculating the energies using standard functionals.[268] Although it is inevitable in applications where we need trends, the inaccuracies may be unimportant, but for qualitative information, better-sophisticated functionals are needed such as hybrid functionals, which provided improved accuracy at the cost of very high computation expenses. The most feasible and alternative methodology is to take the hybrid quantum mechanical/molecular mechanical (QM/MM) approach.

Despite the significant developments in machine learning, its use for organic solar cells is still not as efficient as for inorganic materials owing to the complex nature of organic materials; which mainly rely on the processing solvent, crystallinity, solvent additive, and molecular orientations of the active materials. Further work is, therefore, vital for the efficient use of ML for photo/electro-catalytic materials. Finally, the research efforts that are devoted towards understanding the materials chemistry implying machine learning and data science should not rely on each other; each aspect is critical and researchers, therefore, should be capable to have expertise on both sides in a concerted fashion. This may allow researchers to predict the corresponding materials using lower-level theory while refine the selective materials with higher-level theory.

5. Conclusion and Outlook

Photocatalytic water splitting is a fascinating, appealing, and green technology to fulfill global energy demand. To carry out water splitting in an efficient and facile way, the designing of suitable heterostructure catalysts is the need of the hour. So a comprehensive understanding of the electronic structure and reactivity of these heterostructures is of prime significance. This review is an effort to consolidate major experimental and theoretical progress and developments in the Z-scheme photocatalytic water splitting to better understand and explore the interfacial chemistry of the heterojunction.

In the last few years, several SCs such as sulfides, oxysulfides, metal oxides, nitrides, oxynitrides, carbon-based nitrides, and polymer-based sulfides, have been used to develop Z-scheme module using several redox mediators. To address problems associated with 1st generation Z-scheme, a surface modification strategy has been devised, though with little success. Since then, the use of 2nd and 3rd generation strategies has become more prevalent owing to the efficient suppression of shielding effect and backward process. Carbonaceous materials such as graphene and CNTs, also referred to as second-generation catalysts, are considered potential emerging materials in the Z-scheme family.[47,269] However, to avoid the creation of defects (a serious problem) during the synthesis of the carbon-based Z-scheme, the construction needs careful monitoring. In a direct Z-scheme system (3rd generation); however, the selection of SCs is pivotal, as the creation of the internal electric field strongly relies on the nature of SCs.[21]

The introduction of non-oxides SCs as the Z-scheme system has caused the extension of the visible absorption range up to 700 nm, a notable advantage over conventional one-step photocatalytic water splitting. Although, all three Z-scheme systems have associated advantages and disadvantages, yet the efficiency in each case can be improved to the desired level of solar to fuel conversion efficiency by the optimization of components. For example, the dramatic decline in the STH efficiency (1.1%) beyond 10 KPa in $SrTiO_3$:La, Rh/Au nanoparticle/$BiVO_4$:Mo Sheets (due to the backward reaction) has been increased up to 1.00% when the Au mediator was replaced with carbon film, suggesting that a suitable mediator can suppress the backward reaction.[270] Some other promising aspects to trigger the light absorption capability and catalytic efficiency of the Z-scheme module include the exploration of novel *p-n* junctions materials, exposed crystal facets, and the development of novel SC materials and their surface modification. In this context, polymer-based photocatalysts, for example, g-C_3N_4, having a tunable bandgap, band edge positions, and excellent stability can be a nice option. Furthermore, some metal complexes and polyoxometalates emerge as new auspicious mediators for Z-scheme; however, most Z-scheme systems still rely on Fe^{3+}/Fe^{2+} or IO_3^-/I^- redox couple. These redox couples, however, are problematic in terms of improving the total efficiency of water-splitting reaction.

Theoretical simulations based on DFT calculations, combined with several experimental techniques such as radical-species trapping tests, photocatalytic testing, XAS, XANES, XPS, and DRIFTS, are the efforts being made to explore the mechanistic pathway. DFT calculations based on theoretical studies are used to explore reactivity trends, mechanisms, quantification, and experimental verification of chemical reactivity descriptors.

The interaction of water with the catalyst cannot be ignored and thus needs considerable attention. The way water interacts with the heterojunction defines the type of contact at the catalyst-water interfaces. Indeed, other factors such as the reaction media, band edge potentials of the heterojunction, and catalyst morphology as well as dimension may be responsible for direct contact with one or both the SCs. The mechanistic investigation of important redox reactions in water splitting through DFT is crucial to explain the nature of water adsorption on active sites, which in turn helps to predict the kind of intermediate formed as well as the energetics of reaction profile. However, the

precise determination of band edge potentials of the complex heterojunction and their correlation with the water redox potentials is a challenging task. Although many-body perturbation theory so-called GW calculation can compute the energy of a system containing thousands of electrons, yet challenging due to prohibitive computational cost.To this aim, the only promising solution is to develop novel hybrid functionals that can validate the many-body perturbation theory.[266,271]

Several important pieces of information gathered from the first-principles simulation can be used as inputs for continuum approaches and classical simulations. Furthermore, interfacial simulations can be combined with high-throughput testing methods. For example, photocatalyst materials determined from high-throughput simulations are often based on bulk properties which can be used further as inputs for more refined interfacial simulations to understand the behavior of materials in more realistic environments. With the start of another decade, the attention has been diverted to the expansion of technologies, specifically on particulate Z-scheme photocatalyst sheets with potential scalability in overall water splitting. Though there is growing reliance of experimental research on state-of-the-art analytical techniques, yet the use of theory and experiment in a concerted manner would be of particular importance to further explore the Z-scheme. Such tight integration between simulations and experimental approaches would be critical to design a proficient Z-scheme system. Since the reported solar-to-fuel efficiency till this time is very modest (e.g., μmol h^{-1} g_{cat}^{-1}), there is a need for a scale-up process to compete for benchmarking. In the hopeful future, a highly efficient Z-scheme module can be methodically realized to drive large-scale photocatalytic water splitting for viable H_2 production.

Acknowledgements

The authors acknowledge the financial support from the Higher Education Commission of Pakistan.

Conflict of Interest

The authors declare no conflict of interest.

Keywords

computational modeling, hydrogen evolution reaction, photocatalysis, water splitting, Z-scheme

Received: July 6, 2021
Revised: August 23, 2021
Published online:

[1] H. Tada, T. Mitsui, T. Kiyonaga, T. Akita, K. Tanaka, *Nat. Mater.* **2006**, *5*, 782.
[2] Y. Wang, H. Suzuki, J. Xie, O. Tomita, D. J. Martin, M. Higashi, D. Kong, R. Abe, J. Tang, *Chem. Rev.* **2018**, *118*, 5201.
[3] K. Maeda, *ACS Catal.* **2013**, *3*, 1486.
[4] Q. Wang, Y. Li, T. Hisatomi, M. Nakabayashi, N. Shibata, J. Kubota, K. Domen, *J. Catal.* **2015**, *328*, 308.
[5] A. Fujishima, K. Honda, *Nature* **1972**, *238*, 37.
[6] J. A. Nasir, Z. Rehman, S. N. A. Shah, A. Khan, I. S. Butler, C. R. A. Catlow, *J. Mater. Chem. A* **2020**, *8*, 20752.
[7] A. Hezam, K. Namratha, Q. Drmosh, D. Ponnamma, A. M. N. Saeed, V. Ganesh, B. Neppolian, K. Byrappa, *J. Mater. Chem. A* **2018**, *6*, 21379.
[8] P. Zhou, J. Yu, M. Jaroniec, *Adv. Mater.* **2014**, *26*, 4920.
[9] S. Chen, T. Takata, K. Domen, *Nat. Rev. Mater.* **2017**, *2*, 17050.
[10] T. Hisatomi, J. Kubota, K. Domen, *Chem. Soc. Rev.* **2014**, *43*, 7520.
[11] a) Y.-J. Yuan, D. Chen, Z.-T. Yu, Z.-G. Zou, *J. Mater. Chem. A* **2018**, *6*, 11606; b) L. Cheng, Q. Xiang, Y. Liao, H. Zhang, *Energy Environ. Sci.* **2018**, *11*, 1362; c) P. Dong, G. Hou, X. Xi, R. Shao, F. Dong, *Environ. Sci.: Nano* **2017**, *4*, 539; d) Y. Tachibana, L. Vayssieres, J. R. Durrant, *Nat. Photonics* **2012**, *6*, 511; e) S. J. Moniz, S. A. Shevlin, D. J. Martin, Z.-X. Guo, J. Tang, *Energy Environ. Sci.* **2015**, *8*, 731; f) H. Ahmad, S. Kamarudin, L. Minggu, M. Kassim, *Renewable Sustainable Energy Rev.* **2015**, *43*, 599.
[12] Y. Wang, Q. Wang, X. Zhan, F. Wang, M. Safdar, J. He, *Nanoscale* **2013**, *5*, 8326.
[13] J. Zeng, L. Xu, X. Luo, B. Peng, Z. Ma, L.-L. Wang, Y. Yang, C. Shuai, *Phys. Chem. Chem. Phys.* **2021**, *23*, 2812.
[14] B. J. Ng, L. K. Putri, X. Y. Kong, Y. W. Teh, P. Pasbakhsh, S. P. Chai, *Adv. Sci.* **2020**, *7*, 1903171.
[15] Y. Wang, X. Shang, J. Shen, Z. Zhang, D. Wang, J. Lin, J. C. Wu, X. Fu, X. Wang, C. Li, *Nat. Commun.* **2020**, *11*, 3043.
[16] K. Murofushi, K. Ogawa, H. Suzuki, R. Sakamoto, O. Tomita, K. Kato, A. Yamakata, A. Saeki, R. Abe, *J. Mater. Chem. A* **2021**, *9*, 11718.
[17] K. Iwashina, A. Iwase, Y. H. Ng, R. Amal, A. Kudo, *J. Am. Chem. Soc.* **2015**, *137*, 604.
[18] X. Liu, Q. Zhang, D. Ma, *Sol. RRL* **2021**, *5*, 2000397.
[19] R. B. Chandran, S. Breen, Y. Shao, S. Ardo, A. Z. Weber, *Energy Environ. Sci.* **2018**, *11*, 115.
[20] S. Haussener, C. Xiang, J. M. Spurgeon, S. Ardo, N. S. Lewis, A. Z. Weber, *Energy Environ. Sci.* **2012**, *5*, 9922.
[21] J. Low, C. Jiang, B. Cheng, S. Wageh, A. A. Al-Ghamdi, J. Yu, *Small Methods* **2017**, *1*, 1700080.
[22] a) K. Qi, B. Cheng, J. Yu, W. Ho, *Chin. J. Catal.* **2017**, *38*, 1936; b) D. Huang, S. Chen, G. Zeng, X. Gong, C. Zhou, M. Cheng, W. Xue, X. Yan, J. Li, *Coord. Chem. Rev.* **2019**, *385*, 44.
[23] T. Di, Q. Xu, W. Ho, H. Tang, Q. Xiang, J. Yu, *ChemCatChem* **2019**, *11*, 1394.
[24] a) L. Jiang, X. Yuan, G. Zeng, J. Liang, Z. Wu, H. Wang, *Environ. Sci.: Nano* **2018**, *5*, 599; b) X. Xia, M. Song, H. Wang, X. Zhang, N. Sui, Q. Zhang, V. L. Colvin, W. Y. William, *Nanoscale* **2019**, *11*, 11071.
[25] L. Lin, T. Hisatomi, S. Chen, T. Takata, K. Domen, *Trends in Chemistry* **2020**, *2*, 813.
[26] L. Zhang, W. Wang, S. Sun, D. Jiang, E. Gao, *Appl. Catal., B* **2015**, *162*, 470.
[27] A. Deshpande, P. Shah, R. Gholap, N. M. Gupta, *J. Colloid Interface Sci.* **2009**, *333*, 263.
[28] Y. Wen Teh, Y. Wei Goh, X. Ying Kong, B. J. Ng, S. T. Yong, S. P. Chai, *ChemCatChem* **2019**, *11*, 6431.
[29] K. Maeda, K. Domen, *J. Phys. Chem. Lett.* **2010**, *1*, 2655.
[30] J. Franck, K. F. Herzfeld, *J. Phys. Chem.* **1941**, *45*, 978.
[31] E. Rabinowitch, *Annu. Rev. Phys. Chem.* **1951**, *2*, 361.
[32] C. Raut, W. L. Simpson, *Arch. Biochem. Biophys.* **1955**, *57*, 218.
[33] D. Shevela, L. O. Björn, *Photosynth. Res.* **2017**, *133*, 5.
[34] A. J. Bard, *J. Photochem.* **1979**, *10*, 59.
[35] R. Abe, K. Sayama, K. Domen, H. Arakawa, *Chem. Phys. Lett.* **2001**, *344*, 339.
[36] H. Li, W. Tu, Y. Zhou, Z. Zou, *Adv. Sci.* **2016**, *3*, 1500389.
[37] Z. Pan, T. Hisatomi, Q. Wang, M. Nakabayashi, N. Shibata, C. Pan, T. Takata, K. Domen, *Appl. Catal., A* **2016**, *521*, 26.

[38] J. Low, J. Yu, M. Jaroniec, S. Wageh, A. A. Al-Ghamdi, *Adv. Mater.* **2017**, *29*, 1601694.
[39] Q. Wang, T. Hisatomi, Q. Jia, H. Tokudome, M. Zhong, C. Wang, Z. Pan, T. Takata, M. Nakabayashi, N. Shibata, *Nat. Mater.* **2016**, *15*, 611.
[40] R. Zhang, L. Zhang, Q. Zheng, P. Gao, J. Zhao, J. Yang, *J. Phys. Chem. Lett.* **2018**, *9*, 5419.
[41] Y. Sasaki, H. Nemoto, K. Saito, A. Kudo, *J. Phys. Chem. C* **2009**, *113*, 17536.
[42] G. Liu, L. Wang, H. G. Yang, H.-M. Cheng, G. Q. M. Lu, *J. Mater. Chem.* **2010**, *20*, 831.
[43] K. R. Tolod, S. Hernández, N. Russo, *Catalysts* **2017**, *7*, 13.
[44] a) J. Zhuang, C. He, K. Wang, K. Teng, Z. Ma, S. Zhang, L. Lu, X. Li, Y. Zhang, Q. An, *Appl. Surf. Sci.* **2021**, *537*, 148055; b) L. Guo, Z. Yang, K. Marcus, Z. Li, B. Luo, L. Zhou, X. Wang, Y. Du, Y. Yang, *Energy Environ. Sci.* **2018**, *11*, 106.
[45] Y. Wang, B. Ren, J. Z. Ou, K. Xu, C. Yang, Y. Li, H. Zhang, *Sci. Bull.* **2021**, *66*, 1228.
[46] a) A. Kudo, *MRS Bull.* **2011**, *36*, 32; b) H. J. Yun, H. Lee, N. D. Kim, D. M. Lee, S. Yu, J. Yi, *ACS Nano* **2011**, *5*, 4084.
[47] A. Iwase, Y. H. Ng, Y. Ishiguro, A. Kudo, R. Amal, *J. Am. Chem. Soc.* **2011**, *133*, 11054.
[48] K. Sayama, K. Mukasa, R. Abe, Y. Abe, H. Arakawa, *J. Photochem. Photobiol. A: Chem.* **2002**, *148*, 71.
[49] A. Nakada, A. Saeki, M. Higashi, H. Kageyama, R. Abe, Kyoto University, Japan **2018**.
[50] K. Maeda, D. Lu, K. Domen, *ACS Catal.* **2013**, *3*, 1026.
[51] K. Maeda, M. Higashi, D. Lu, R. Abe, K. Domen, *J. Am. Chem. Soc.* **2010**, *132*, 5858.
[52] R. Abe, K. Sayama, H. Sugihara, *J. Phys. Chem. B* **2005**, *109*, 16052.
[53] K. Maeda, *J. Photochem. Photobiol., C* **2011**, *12*, 237.
[54] R. Abe, M. Higashi, K. Domen, *ChemSusChem* **2011**, *4*, 154.
[55] K. Sayama, R. Abe, H. Arakawa, H. Sugihara, *Catal. Commun.* **2006**, *7*, 96.
[56] A. Kumar, G. Sharma, A. Kumari, C. Guo, M. Naushad, D.-V. N. Vo, J. Iqbal, F. J. Stadler, *Appl. Catal., B* **2021**, *284*, 119808.
[57] Y. Sasaki, H. Kato, A. Kudo, *J. Am. Chem. Soc.* **2013**, *135*, 5441.
[58] M. Higashi, R. Abe, T. Takata, K. Domen, *Chem. Mater.* **2009**, *21*, 1543.
[59] K. Sayama, K. Mukasa, R. Abe, Y. Abe, H. Arakawa, *Chem. Commun.* **2001**, 2416.
[60] R. Abe, T. Takata, H. Sugihara, K. Domen, *Chem. Commun.* **2005**, 3829.
[61] M. Higashi, R. Abe, A. Ishikawa, T. Takata, B. Ohtani, K. Domen, *Chem. Lett.* **2008**, *37*, 138.
[62] T. Oshima, S. Nishioka, Y. Kikuchi, S. Hirai, K.-i. Yanagisawa, M. Eguchi, Y. Miseki, T. Yokoi, T. Yui, K. Kimoto, *J. Am. Chem. Soc.* **2020**, *142*, 8412.
[63] Z. Wang, Y. Luo, T. Hisatomi, J. J. M. Vequizo, S. Suzuki, S. Chen, M. Nakabayashi, L. Lin, Z. Pan, N. Kariya, *Nat. Commun.* **2021**, *12*, 1005.
[64] M. Tabata, K. Maeda, M. Higashi, D. Lu, T. Takata, R. Abe, K. Domen, *Langmuir* **2010**, *26*, 9161.
[65] W. Zhao, K. Maeda, F. Zhang, T. Hisatomi, K. Domen, *Phys. Chem. Chem. Phys.* **2014**, *16*, 12051.
[66] Y. Miseki, S. Fujiyoshi, T. Gunji, K. Sayama, *Catal. Sci. Technol.* **2013**, *3*, 1750.
[67] S. Tanigawa, H. Irie, *Appl. Catal., B* **2016**, *180*, 1.
[68] R. Abe, K. Shinmei, K. Hara, B. Ohtani, *Chem. Commun.* **2009**, 3577.
[69] R. Abe, K. Shinmei, N. Koumura, K. Hara, B. Ohtani, *J. Am. Chem. Soc.* **2013**, *135*, 16872.
[70] D. J. Martin, P. J. T. Reardon, S. J. Moniz, J. Tang, *J. Am. Chem. Soc.* **2014**, *136*, 12568.
[71] S. Chen, Y. Qi, T. Hisatomi, Q. Ding, T. Asai, Z. Li, S. S. K. Ma, F. Zhang, K. Domen, C. Li, *Angew. Chem.* **2015**, *127*, 8618.
[72] A. Nakada, S. Nishioka, J. J. M. Vequizo, K. Muraoka, T. Kanazawa, A. Yamakata, S. Nozawa, H. Kumagai, S.-i. Adachi, O. Ishitani, *J. Mater. Chem. A* **2017**, *5*, 11710.
[73] H. Kato, M. Hori, R. Konta, Y. Shimodaira, A. Kudo, *Chem. Lett.* **2004**, *33*, 1348.
[74] Y. Sasaki, A. Iwase, H. Kato, A. Kudo, *J. Catal.* **2008**, *259*, 133.
[75] H. Kato, Y. Sasaki, N. Shirakura, A. Kudo, *J. Mater. Chem. A* **2013**, *1*, 12327.
[76] R. Niishiro, S. Tanaka, A. Kudo, *Appl. Catal., B* **2014**, *150*, 187.
[77] H. Suzuki, O. Tomita, M. Higashi, R. Abe, *Chem. Lett.* **2015**, *44*, 1134.
[78] H. Fujito, H. Kunioku, D. Kato, H. Suzuki, M. Higashi, H. Kageyama, R. Abe, *J. Am. Chem. Soc.* **2016**, *138*, 2082.
[79] W. Chen, M. Liu, X. Li, L. Mao, *Appl. Surf. Sci.* **2020**, *512*, 145782.
[80] Y.-R. Lin, G. V. C. Dizon, K. Yamada, C.-Y. Liu, A. Venault, H.-Y. Lin, M. Yoshida, C. Hu, *J. Colloid Interface Sci.* **2020**, *567*, 202.
[81] Y. Zou, J.-W. Shi, D. Ma, Z. Fan, C. Niu, L. Wang, *ChemCatChem* **2017**, *9*, 3752.
[82] W.-K. Jo, N. C. S. Selvam, *Chem. Eng. J.* **2017**, *317*, 913.
[83] X. Chen, J. Wang, Y. Chai, Z. Zhang, Y. Zhu, *Adv. Mater.* **2021**, *33*, 2007479.
[84] Q. Xu, L. Zhang, J. Yu, S. Wageh, A. A. Al-Ghamdi, M. Jaroniec, *Mater. Today* **2018**, *21*, 1042.
[85] S. S. K. Ma, K. Maeda, T. Hisatomi, M. Tabata, A. Kudo, K. Domen, *Chem. A Eur. J.* **2013**, *19*, 7480.
[86] J. Wang, Y. Zhang, X. Wang, W. Su, *Appl. Catal., B* **2020**, *268*, 118444.
[87] H. Yoo, S. Kahng, J. H. Kim, *Sol. Energy Mater. Sol. Cells* **2020**, *204*, 110211.
[88] H. Xie, Y. Zhao, H. Li, Y. Xu, X. Chen, *J. Mater. Sci.* **2019**, *54*, 10836.
[89] Y. You, S. Wang, K. Xiao, T. Ma, Y. Zhang, H. Huang, *ACS Sustainable Chem. Eng.* **2018**, *6*, 16219.
[90] Z. Mo, H. Xu, Z. Chen, X. She, Y. Song, J. Lian, X. Zhu, P. Yan, Y. Lei, S. Yuan, *Appl. Catal., B* **2019**, *241*, 452.
[91] G. QingáLu, *Chem. Commun.* **2009**, 3452.
[92] H. Katsumata, Y. Tachi, T. Suzuki, S. Kaneco, *RSC Adv.* **2014**, *4*, 21405.
[93] F. Xu, W. Xiao, B. Cheng, J. Yu, *Int. J. Hydrogen Energy* **2014**, *39*, 15394.
[94] W. Chen, T.-Y. Liu, T. Huang, X.-H. Liu, G.-R. Duan, X.-J. Yang, S.-M. Chen, *RSC Adv.* **2015**, *5*, 101214.
[95] Y. Ma, X. Jiang, R. Sun, J. Yang, X. Jiang, Z. Liu, M. Xie, E. Xie, W. Han, *Chem. Eng. J.* **2020**, *382*, 123020.
[96] F. Liu, R. Shi, Z. Wang, Y. Weng, C. M. Che, Y. Chen, *Angew. Chem.* **2019**, *131*, 11917.
[97] J. Shi, S. Li, F. Wang, Y. Li, L. Gao, X. Zhang, J. Lu, *Catal. Sci. Technol.* **2018**, *8*, 6458.
[98] Z.-F. Huang, J. Song, X. Wang, L. Pan, K. Li, X. Zhang, L. Wang, J.-J. Zou, *Nano Energy* **2017**, *40*, 308.
[99] H.-L. Guo, H. Du, Y.-F. Jiang, N. Jiang, C.-C. Shen, X. Zhou, Y.-N. Liu, A.-W. Xu, *J. Phys. Chem. C* **2017**, *121*, 107.
[100] A. Kudo, Y. Miseki, *Chem. Soc. Rev.* **2009**, *38*, 253.
[101] K. Maeda, K. Domen, *J. Phys. Chem. C* **2007**, *111*, 7851.
[102] R. Nakamura, T. Tanaka, Y. Nakato, *J. Phys. Chem. B* **2005**, *109*, 8920.
[103] a) T. Wei, Z. Jin, F. Li, D. Yan, L. Xu, *Photochem. Photobiol. Sci.* **2020**, *19*, 80; b) S. R. Lingampalli, K. Manjunath, in *Heterostructured Photocatalysts for Solar Energy Conversion*, Elsevier, New York **2021**, p. 109; c) Y. Iwase, O. Tomita, M. Higashi, A. Nakada, R. Abe, *Sustainable Energy Fuels* **2019**, *3*, 1501.
[104] C. D. Windle, H. Kumagai, M. Higashi, R. Brisse, S. Bold, B. Jousselme, M. Chavarot-Kerlidou, K. Maeda, R. Abe, O. Ishitani, *J. Am. Chem. Soc.* **2019**, *141*, 9593.
[105] H. Kumagai, G. Sahara, K. Maeda, M. Higashi, R. Abe, O. Ishitani, *Chem. Sci.* **2017**, *8*, 4242.

[106] G. Natu, P. Hasin, Z. Huang, Z. Ji, M. He, Y. Wu, *ACS Appl. Mater. Interfaces* **2012**, *4*, 5922.
[107] M. Higashi, R. Abe, K. Teramura, T. Takata, B. Ohtani, K. Domen, *Chem. Phys. Lett.* **2008**, *452*, 120.
[108] a) A. Yamakata, M. Kawaguchi, N. Nishimura, T. Minegishi, J. Kubota, K. Domen, *J. Phys. Chem. C* **2014**, *118*, 23897; b) J. Kosco, M. Sachs, R. Godin, M. Kirkus, L. Francas, M. Bidwell, M. Qureshi, D. Anjum, J. R. Durrant, I. McCulloch, *Adv. Energy Mater.* **2018**, *8*, 1802181.
[109] K. Maeda, H. Terashima, K. Kase, M. Higashi, M. Tabata, K. Domen, *Bull. Chem. Soc. Jpn.* **2008**, *81*, 927.
[110] J. Yang, D. Wang, H. Han, C. Li, *Acc. Chem. Res.* **2013**, *46*, 1900.
[111] K. Maeda, R. Abe, K. Domen, *J. Phys. Chem. C* **2011**, *115*, 3057.
[112] K. Maeda, *Phys. Chem. Chem. Phys.* **2013**, *15*, 10537.
[113] S. S. K. Ma, K. Maeda, K. Domen, *Catal. Sci. Technol.* **2012**, *2*, 818.
[114] a) G. Xie, K. Zhang, B. Guo, Q. Liu, L. Fang, J. R. Gong, *Adv. Mater.* **2013**, *25*, 3820; b) P. Wen, Y. Sun, H. Li, Z. Liang, H. Wu, J. Zhang, H. Zeng, S. M. Geyer, L. Jiang, *Appl. Catal., B* **2020**, *263*, 118180.
[115] H. Shen, G. Liu, Y. Zhao, D. Li, J. Jiang, J. Ding, B. Mao, H. Shen, K.-S. Kim, W. Shi, *Fuel* **2020**, *259*, 116311.
[116] A. Samal, D. Das, K. Nanda, B. Mishra, J. Das, A. Dash, *Chem. Asian J.* **2016**, *11*, 584.
[117] A. Iwase, S. Yoshino, T. Takayama, Y. H. Ng, R. Amal, A. Kudo, *J. Am. Chem. Soc.* **2016**, *138*, 10260.
[118] S. Yoshino, A. Iwase, Y. H. Ng, R. Amal, A. Kudo, *ACS Appl. Energy Mater.* **2020**, *3*, 5684.
[119] S. Wan, M. Ou, Q. Zhong, S. Zhang, F. Song, *Chem. Eng. J.* **2017**, *325*, 690.
[120] T. Mahvelati-Shamsabadi, B.-K. Lee, *Renewable Sustainable Energy Rev.* **2020**, *130*, 109957.
[121] W. Yu, J. Chen, T. Shang, L. Chen, L. Gu, T. Peng, *Appl. Catal., B* **2017**, *219*, 693.
[122] R. Marschall, *Adv. Funct. Mater.* **2014**, *24*, 2420.
[123] F. Shi, L. Chen, M. Chen, D. Jiang, *Chem. Commun.* **2015**, *51*, 17144.
[124] a) Z. Jin, N. Murakami, T. Tsubota, T. Ohno, *Appl. Catal., B* **2014**, *150*, 479; b) Y. He, L. Zhang, X. Wang, Y. Wu, H. Lin, L. Zhao, W. Weng, H. Wan, M. Fan, *RSC Adv.* **2014**, *4*, 13610; c) N. Tian, H. Huang, Y. He, Y. Guo, T. Zhang, Y. Zhang, *Dalton Trans.* **2015**, *44*, 4297.
[125] J. Yu, S. Wang, J. Low, W. Xiao, *Phys. Chem. Chem. Phys.* **2013**, *15*, 16883.
[126] R. Ye, H. Fang, Y.-Z. Zheng, N. Li, Y. Wang, X. Tao, *ACS Appl. Mater. Interfaces* **2016**, *8*, 13879.
[127] E. Blanchet, F. Duquenne, Y. Rafrafi, L. Etcheverry, B. Erable, A. Bergel, *Energy Environ. Sci.* **2015**, *8*, 3731.
[128] R. Shen, L. Zhang, X. Chen, M. Jaroniec, N. Li, X. Li, *Appl. Catal., B* **2020**, *266*, 118619.
[129] X. Li, K. Xie, L. Song, M. Zhao, Z. Zhang, *ACS Appl. Mater. Interfaces* **2017**, *9*, 24577.
[130] D. Liu, S. Zhang, J. Wang, T. Peng, R. Li, *ACS Appl. Mater. Interfaces* **2019**, *11*, 27913.
[131] D. Zhao, Y. Wang, C.-L. Dong, Y.-C. Huang, J. Chen, F. Xue, S. Shen, L. Guo, *Nat. Energy* **2021**, *6*, 388.
[132] Z. Yu, F. Li, L. Sun, *Energy Environ. Sci.* **2015**, *8*, 760.
[133] L. Tong, A. Iwase, A. Nattestad, U. Bach, M. Weidelener, G. Götz, A. Mishra, P. Bäuerle, R. Amal, G. G. Wallace, *Energy Environ. Sci.* **2012**, *5*, 9472.
[134] A. M. Brown, L. J. Antila, M. Mirmohades, S. Pullen, S. Ott, L. Hammarström, *J. Am. Chem. Soc.* **2016**, *138*, 8060.
[135] L. Xie, X. Li, X. Wang, W. Ge, J. Zhang, J. Jiang, G. Zhang, *J. Phys. Chem. C* **2018**, *123*, 1846.
[136] Q. Xu, B. Zhu, C. Jiang, B. Cheng, J. Yu, *Sol. RRL* **2018**, *2*, 1800006.
[137] X. Yang, Z. Chen, J. Xu, H. Tang, K. Chen, Y. Jiang, *ACS Appl. Mater. Interfaces* **2015**, *7*, 15285.
[138] C. Yang, Z. Xue, J. Qin, M. Sawangphruk, S. Rajendran, X. Zhang, R. Liu, *J. Phys. Chem. C* **2019**, *123*, 4795.
[139] H. Zhao, X. Ding, B. Zhang, Y. Li, C. Wang, *Sci. Bull.* **2017**, *62*, 602.
[140] Y. Yang, M. Qiu, Q. Qi, F. Chen, J. Chen, Y. Liu, L. Yang, *ACS Appl. Nano Mater.* **2020**, *3*, 10296.
[141] W. Wang, M. O. Tadé, Z. Shao, *Chem. Soc. Rev.* **2015**, *44*, 5371.
[142] W. Wang, M. Xu, X. Xu, W. Zhou, Z. Shao, *Angew. Chem., Int. Ed.* **2020**, *59*, 136.
[143] B. Dong, Y. Qi, J. Cui, B. Liu, F. Xiong, X. Jiang, Z. Li, Y. Xiao, F. Zhang, C. Li, *Dalton Trans.* **2017**, *46*, 10707.
[144] R. Wang, C. Ye, H. Wang, F. Jiang, *ACS Omega* **2020**, *5*, 30373.
[145] H. P. Duong, T. Mashiyama, M. Kobayashi, A. Iwase, A. Kudo, Y. Asakura, S. Yin, M. Kakihana, H. Kato, *Appl. Catal., B* **2019**, *252*, 222.
[146] J. Han, Y. Gao, Y. Li, Z. Chen, X. Liu, X. Xiong, X. Zhang, Y. Jiang, Q. Luo, Y. Song, *J. Phys. Chem. C* **2020**, *124*, 24164.
[147] X. Tao, Y. Zhao, L. Mu, S. Wang, R. Li, C. Li, *Adv. Energy Mater.* **2018**, *8*, 1701392.
[148] X. Du, T. Zhao, Z. Xiu, Z. Xing, Z. Li, K. Pan, S. Yang, W. Zhou, *Appl. Mater. Today* **2020**, *20*, 100719.
[149] A. Nakada, M. Higashi, T. Kimura, H. Suzuki, D. Kato, H. Okajima, T. Yamamoto, A. Saeki, H. Kageyama, R. Abe, *Chem. Mater.* **2019**, *31*, 3419.
[150] T. Yin, L. Long, X. Tang, M. Qiu, W. Liang, R. Cao, Q. Zhang, D. Wang, H. Zhang, *Adv. Sci.* **2020**, *7*, 2001431.
[151] J. Hu, D. Chen, Z. Mo, N. Li, Q. Xu, H. Li, J. He, H. Xu, J. Lu, *Angew. Chem., Int. Ed.* **2019**, *58*, 2073.
[152] a) F. Guo, L. Wang, H. Sun, M. Li, W. Shi, *Inorg. Chem. Front.* **2020**, *7*, 1770; b) A. Mukherji, R. Marschall, A. Tanksale, C. Sun, S. C. Smith, G. Q. Lu, L. Wang, *Adv. Funct. Mater.* **2011**, *21*, 126; c) M. P. Kumar, R. Jagannathan, S. Ravichandran, *Energy Fuels* **2020**, *34*, 9030.
[153] a) C. Kalaiselvi, T. Senthil, M. Shankar, V. Sasirekha, *Appl. Organomet. Chem.* **2021**, *35*, e6207; b) C. Kalaiselvi, P. Ravi, T. Senthil, M. Sathish, M. Kang, *Mater. Lett.* **2020**, *275*, 128166.
[154] J. Cui, Y. Qi, B. Dong, L. Mu, Q. Ding, G. Liu, M. Jia, F. Zhang, C. Li, *Appl. Catal., B* **2019**, *241*, 1.
[155] F. Yang, Q. Zhang, J. Zhang, L. Zhang, M. Cao, W.-L. Dai, *Appl. Catal., B* **2020**, *278*, 119290.
[156] J. Zhu, J. Xu, X. Du, Q. Li, Y. Fu, M. Chen, *Dalton Trans.* **2020**, *49*, 8891.
[157] S. Kumar, N. Yadav, P. Kumar, A. K. Ganguli, *Inorg. Chem.* **2018**, *57*, 15112.
[158] C. Li, H. Che, Y. Yan, C. Liu, H. Dong, *Chem. Eng. J.* **2020**, *398*, 125523.
[159] L. J. Zhang, S. Li, B. K. Liu, D. J. Wang, T. F. Xie, *ACS Catal.* **2014**, *4*, 3724.
[160] Y. Huang, Y. Liu, D. Zhu, Y. Xin, B. Zhang, *J. Mater. Chem. A* **2016**, *4*, 13626.
[161] X. Jia, M. Tahir, L. Pan, Z.-F. Huang, X. Zhang, L. Wang, J.-J. Zou, *Appl. Catal., B* **2016**, *198*, 154.
[162] D. P. Kumar, S. Hong, D. A. Reddy, T. K. Kim, *J. Mater. Chem. A* **2016**, *4*, 18551.
[163] P. Li, X. Yan, S. Gao, R. Cao, *Chem. Eng. J.* **2021**, *421*, 129870.
[164] S. Wang, B. Y. Guan, X. Wang, X. W. D. Lou, *J. Am. Chem. Soc.* **2018**, *140*, 15145.
[165] B. Qiu, Q. Zhu, M. Du, L. Fan, M. Xing, J. Zhang, *Angew. Chem., Int. Ed.* **2017**, *56*, 2684.
[166] T. Zhang, F. Meng, Y. Cheng, N. Dewangan, G. W. Ho, S. Kawi, *Appl. Catal., B*, *286*, 119853.
[167] a) Y. Tian, X. Yang, L. Li, Y. Zhu, Q. Wu, Y. Li, F. Ma, Y. Yu, *Chemosphere* **2021**, *279*, 130882; b) K. Yu, H.-B. Huang, J.-T. Wang, G.-F. Liu, Z. Zhong, Y.-F. Li, H.-L. Cao, J. Lü, R. Cao, *J. Mater. Chem. A* **2021**, *9*, 7759; c) Y. Liu, Y. Sun, J. Xu, M. Mao, X. Li, *New J. Chem.* **2021**, *45*, 7781.
[168] J. Murillo-Sierra, A. Hernández-Ramírez, Z.-Y. Zhao, A. Martínez-Hernández, M. Gracia-Pinilla, *J. Environ. Chem. Eng.* **2021**, *9*, 105111.

[169] Y. Nosaka, *J. Phys. Chem.* **1991**, *95*, 5054.
[170] a) Y. Tian, T. Tatsuma, *J. Am. Chem. Soc.* **2005**, *127*, 7632; b) A. Tanaka, K. Hashimoto, H. Kominami, *J. Am. Chem. Soc.* **2012**, *134*, 14526; c) Y. Nishijima, K. Ueno, Y. Yokota, K. Murakoshi, H. Misawa, *J. Phys. Chem. Lett.* **2010**, *1*, 2031; d) Y. Nishijima, K. Ueno, Y. Kotake, K. Murakoshi, H. Inoue, H. Misawa, *J. Phys. Chem. Lett.* **2012**, *3*, 1248.
[171] X. Wang, S. Li, Y. Ma, H. Yu, J. Yu, *J. Phys. Chem. C* **2011**, *115*, 14648.
[172] L. Ye, J. Liu, C. Gong, L. Tian, T. Peng, L. Zan, *ACS Catal.* **2012**, *2*, 1677.
[173] K. Sekizawa, K. Maeda, K. Domen, K. Koike, O. Ishitani, *J. Am. Chem. Soc.* **2013**, *135*, 4596.
[174] L. Guo, H. Huang, L. Mei, M. Li, Y. Zhang, *Mater. Chem. Front.* **2021**, *5*, 2484.
[175] a) S. Shinde, C. Bhosale, K. Rajpure, *Catal. Rev.* **2013**, *55*, 79; b) S. Gligorovski, R. Strekowski, S. Barbati, D. Vione, *Chem. Rev.* **2015**, *115*, 13051.
[176] W. Yu, D. Xu, T. Peng, *J. Mater. Chem. A* **2015**, *3*, 19936.
[177] P. Zhang, T. Wang, J. Gong, *Chem* **2018**, *4*, 223.
[178] C. Wu, S. Xue, Z. Qin, M. Nazari, G. Yang, S. Yue, T. Tong, H. Ghasemi, F. C. R. Hernandez, S. Xue, *Appl. Catal., B* **2021**, *282*, 119557.
[179] Y. Mao, Y. Gao, W. Dong, H. Wu, Z. Song, X. Zhao, J. Sun, W. Wang, *Appl. Energy* **2020**, *267*, 114860.
[180] H. Li, H. Yu, X. Quan, S. Chen, Y. Zhang, *ACS Appl. Mater. Interfaces* **2016**, *8*, 2111.
[181] E. Jiang, N. Song, G. Che, C. Liu, H. Dong, L. Yang, *Chem. Eng. J.* **2020**, *399*, 125721.
[182] Y. Goto, T. Hisatomi, Q. Wang, T. Higashi, K. Ishikiriyama, T. Maeda, Y. Sakata, S. Okunaka, H. Tokudome, M. Katayama, *Joule* **2018**, *2*, 509.
[183] Z. Wang, C. Li, K. Domen, *Chem. Soc. Rev.* **2019**, *48*, 2109.
[184] M. Cao, L. Ni, Z. Wang, J. Liu, Y. Tian, Y. Zhang, X. Wei, T. Guo, J. Fan, L. Duan, *Appl. Surf. Sci.* **2021**, *551*, 149364.
[185] a) W. Xu, W. Tian, L. Meng, F. Cao, L. Li, *Adv. Energy Mater.* **2021**, *11*, 2003500; b) M. Humayun, H. Ullah, J. Cao, W. Pi, Y. Yuan, S. Ali, A. A. Tahir, P. Yue, A. Khan, Z. Zheng, *Nano-Micro Lett.* **2020**, *12*, 7.
[186] K. Ren, W. Tang, M. Sun, Y. Cai, Y. Cheng, G. Zhang, *Nanoscale* **2020**, *12*, 17281.
[187] L. Ju, Y. Dai, W. Wei, M. Li, B. Huang, *Appl. Surf. Sci.* **2018**, *434*, 365.
[188] Y. Miseki, K. Fujita, S. Iguchi, O. Kitao, T. Gunji, K. Sayama, *Sustainable Energy Fuels* **2020**, *4*, 2686.
[189] K. Burke, *J. Chem. Phys.* **2012**, *136*, 150901.
[190] G. Vignale, M. Rasolt, *Phys. Rev. Lett.* **1987**, *59*, 2360.
[191] a) R. Car, M. Parrinello, *Phys. Rev. Lett.* **1985**, *55*, 2471; b) Z. Zhou, X. Niu, Y. Zhang, J. Wang, *J. Mater. Chem. A* **2019**, *7*, 21835.
[192] a) M. Sulpizi, M. Salanne, M. Sprik, M.-P. Gaigeot, *J. Phys. Chem. Lett.* **2013**, *4*, 83; b) P. Huang, T. A. Pham, G. Galli, E. Schwegler, *J. Phys. Chem. C* **2014**, *118*, 8944.
[193] D. Prendergast, G. Galli, *Phys. Rev. Lett.* **2006**, *96*, 215502.
[194] a) T. Anh Pham, T. Li, H.-V. Nguyen, S. Shankar, F. Gygi, G. Galli, *Appl. Phys. Lett.* **2013**, *102*, 241603; b) T. A. Pham, C. Zhang, E. Schwegler, G. Galli, *Phys. Rev. B* **2014**, *89*, 060202; c) A. Singh, M. Jain, S. Bhattacharya, arXiv preprint arXiv:2010.13819 2020.
[195] a) A. Walsh, Y. Yan, M. N. Huda, M. M. Al-Jassim, S.-H. Wei, *Chem. Mater.* **2009**, *21*, 547; b) J. Yang, D. Wang, X. Zhou, C. Li, *Chem.–A Eur. J.* **2013**, *19*, 1320.
[196] R. Li, F. Zhang, D. Wang, J. Yang, M. Li, J. Zhu, X. Zhou, H. Han, C. Li, *Nat. Commun.* **2013**, *4*, 1432.
[197] J. Liu, B. Cheng, J. Yu, *Phys. Chem. Chem. Phys.* **2016**, *18*, 31175.
[198] W. Xu, W. Tian, L. Meng, F. Cao, L. Li, *Adv. Energy Mater.* **2021**, *11*, 2003500.
[199] J. Low, B. Dai, T. Tong, C. Jiang, J. Yu, *Adv. Mater.* **2019**, *31*, 1802981.
[200] X. Yu, J. Xie, Q. Liu, H. Dong, Y. Li, *J. Colloid Interface Sci.* **2021**, *593*, 133.
[201] S. Bai, J. Jiang, Q. Zhang, Y. Xiong, *Chem. Soc. Rev.* **2015**, *44*, 2893.
[202] Z. Zhang, J. T. YatesJr, *Chem. Rev.* **2012**, *112*, 5520.
[203] a) Y. Chen, T. Shi, P. Liu, X. Ma, L. Shui, C. Shang, Z. Chen, X. Wang, K. Kempa, G. Zhou, *J. Mater. Chem. A* **2018**, *6*, 19167; b) M. Zhu, Z. Sun, M. Fujitsuka, T. Majima, *Angew. Chem., Int. Ed.* **2018**, *57*, 2160.
[204] X. Niu, X. Bai, Z. Zhou, J. Wang, *ACS Catal.* **2020**, *10*, 1976.
[205] K. Wu, Y. Du, H. Tang, Z. Chen, T. Lian, *J. Am. Chem. Soc.* **2015**, *137*, 10224.
[206] L. Ju, Y. Dai, W. Wei, M. Li, Y. Liang, B. Huang, *Phys. Chem. Chem. Phys.* **2018**, *20*, 1904.
[207] S. X. Tao, X. Cao, P. A. Bobbert, *Sci. Rep.* **2017**, *7*, 14386.
[208] K. Wang, L. Jiang, X. Wu, G. Zhang, *J. Mater. Chem. A* **2020**, *8*, 13241.
[209] Y. Chao, P. Zhou, N. Li, J. Lai, Y. Yang, Y. Zhang, Y. Tang, W. Yang, Y. Du, D. Su, *Adv. Mater.* **2019**, *31*, 1807226.
[210] C.-H. Shen, X.-J. Wen, Z.-H. Fei, Z.-T. Liu, Q.-M. Mu, *J. Colloid Interface Sci.* **2020**, *579*, 297.
[211] a) H. J. Chung, G. Y. Jae, I. A. Lee, M. J. Liu, Y. F. Shen, S. P. Sharma, M. A. Jamal, J. H. Yoo, H. J. Kim, S. T. Hong, *FEBS Open Bio* **2016**, *6*, 64; b) Z. Wang, K. Dai, L. Lu, C. Liang, L. Geng, *Mater. Lett.* **2016**, *169*, 250; c) X. Lin, X. Guo, W. Shi, H. Zhai, Y. Yan, Q. Wang, *J. Solid State Chem.* **2015**, *229*, 68.
[212] J. Lv, J. Zhang, J. Liu, Z. Li, K. Dai, C. Liang, *ACS Sustainable Chem. Eng.* **2018**, *6*, 696.
[213] a) F. Majumder, H.-E. Swoboda, K. Kempf, C. Klingshirn, *Phys. Rev. B* **1985**, *32*, 2407; b) M. Naseri, *Chem. Phys. Lett.* **2017**, *685*, 310; c) J. Chang, L. Jiang, G. Wang, Y. Huang, H. Chen, *New J. Chem.* **2021**, *45*, 4393.
[214] Y. Benallou, B. Soudini, K. Amara, *Int. J. Mod. Phys. B* **2014**, *28*, 1450121.
[215] Z. Suo, J. Dai, S. Gao, H. Gao, *Results Phys.* **2020**, *17*, 103058.
[216] B. P. Mishra, K. Parida, *J. Mater. Chem. A* **2021**, *9*, 10039.
[217] a) J. J. Concepcion, J. W. Jurss, J. L. Templeton, T. J. Meyer, *J. Am. Chem. Soc.* **2008**, *130*, 16462; b) L.-P. Wang, T. Van Voorhis, *J. Phys. Chem. Lett.* **2011**, *2*, 2200; c) M. G. Walter, E. L. Warren, J. R. McKone, S. W. Boettcher, Q. Mi, E. A. Santori, N. S. Lewis, *Chem. Rev.* **2010**, *110*, 6446.
[218] A. Imanishi, T. Okamura, N. Ohashi, R. Nakamura, Y. Nakato, *J. Am. Chem. Soc.* **2007**, *129*, 11569.
[219] M. G. Mavros, T. Tsuchimochi, T. Kowalczyk, A. McIsaac, L.-P. Wang, T. V. Voorhis, *Inorg. Chem.* **2014**, *53*, 6386.
[220] Y. Li, Q. Wu, Q. Bu, K. Zhang, Y. Lin, D. Wang, X. Zou, T. Xie, *Chin. J. Catal.* **2021**, *42*, 762.
[221] X. Yang, L. Tian, X. Zhao, H. Tang, Q. Liu, G. Li, *Appl. Catal., B* **2019**, *244*, 240.
[222] Y. Bai, K. Nakagawa, A. J. Cowan, C. M. Aitchison, Y. Yamaguchi, M. A. Zwijnenburg, A. Kudo, R. S. Sprick, A. I. Cooper, *J. Mater. Chem. A* **2020**, *8*, 16283.
[223] I. C. Man, H. Y. Su, F. Calle-Vallejo, H. A. Hansen, J. I. Martinez, N. G. Inoglu, J. Kitchin, T. F. Jaramillo, J. K. Nørskov, J. Rossmeisl, *ChemCatChem* **2011**, *3*, 1159.
[224] a) I. C. Man, H. Y. Su, F. Calle-Vallejo, H. A. Hansen, J. I. Martínez, N. G. Inoglu, J. Kitchin, T. F. Jaramillo, J. K. Nørskov, J. Rossmeisl, *ChemCatChem* **2011**, *3*, 1159; b) Q. Wang, K. Domen, *Chem. Rev.* **2019**, *120*, 919.
[225] H. Dau, C. Limberg, T. Reier, M. Risch, S. Roggan, P. Strasser, *ChemCatChem* **2010**, *2*, 724.
[226] a) T. Shinagawa, A. T. Garcia-Esparza, K. Takanabe, *ChemElectroChem* **2014**, *1*, 1497; b) B. Owens-Baird, Y. V. Kolen'ko, K. Kovnir, *Chem. Eur. J.* **2018**, *24*, 7298; c) T. Hisatomi, K. Takanabe, K. Domen, *Catal. Lett.* **2015**, *145*, 95.

[227] S. Trasatti, *J. Electroanal. Chem. Interfacial Electrochem.* **1972**, *39*, 163.
[228] E. Skúlason, V. Tripkovic, M. E. Björketun, S. Gudmundsdottir, G. Karlberg, J. Rossmeisl, T. Bligaard, H. Jónsson, J. K. Nørskov, *J. Phys. Chem. C* **2010**, *114*, 18182.
[229] A. Malathi, J. Madhavan, M. Ashokkumar, P. Arunachalam, *Appl. Catal., A* **2018**, *555*, 47.
[230] J. H. Kim, J. S. Lee, *Energy Environ. Focus* **2014**, *3*, 339.
[231] Q. Wang, Y. Lin, P. Li, M. Ma, V. Maheskumar, Z. Jiang, R. Zhang, *Int. J. Hydrogen Energy* **2021**, *46*, 247.
[232] J. Safaei, H. Ullah, N. A. Mohamed, M. F. M. Noh, M. F. Soh, A. A. Tahir, N. A. Ludin, M. A. Ibrahim, W. N. R. W. Isahak, M. A. M. Teridi, *Appl. Catal., B* **2018**, *234*, 296.
[233] C. Ai, J. Li, L. Yang, Z. Wang, Z. Wang, Y. Zeng, R. Deng, S. Lin, C. Z. Wang, *ChemSusChem* **2020**, *13*, 4985.
[234] J.-X. Sun, Y.-P. Yuan, L.-G. Qiu, X. Jiang, A.-J. Xie, Y.-H. Shen, J.-F. Zhu, *Dalton Trans.* **2012**, *41*, 6756.
[235] J.-C. Wang, L. Zhang, W.-X. Fang, J. Ren, Y.-Y. Li, H.-C. Yao, J.-S. Wang, Z.-J. Li, *ACS Appl. Mater. Interfaces* **2015**, *7*, 8631.
[236] a) Q. Sun, K. Lv, Z. Zhang, M. Li, B. Li, *Appl. Catal., B* **2015**, *164*, 428; b) W.-K. Jo, T. S. Natarajan, *Chem. Eng. J.* **2015**, *281*, 549.
[237] a) A. Zunger, *Nat. Rev. Chem.* **2018**, *2*, 0121; b) R. Ramprasad, R. Batra, G. Pilania, A. Mannodi-Kanakkithodi, C. Kim, *npj Comput. Mater.* **2017**, *3*, 54; c) A. Agrawal, A. Choudhary, *APL Mater.* **2016**, *4*, 053208; d) Q. Tao, T. Lu, Y. Sheng, L. Li, W. Lu, M. Li, *J. Energy Chem.* **2021**, *60*, 351.
[238] R. K. Lindsay, *Applications of Artificial Intelligence for Organic Chemistry: The DENDRAL Project*, McGraw-Hill Companies, New York **1980**.
[239] J. M. Stokes, K. Yang, K. Swanson, W. Jin, A. Cubillos-Ruiz, N. M. Donghia, C. R. MacNair, S. French, L. A. Carfrae, Z. Bloom-Ackermann, *Cell* **2020**, *180*, 688.
[240] a) R. Gómez-Bombarelli, J. Aguilera-Iparraguirre, T. D. Hirzel, D. Duvenaud, D. Maclaurin, M. A. Blood-Forsythe, H. S. Chae, M. Einzinger, D.-G. Ha, T. Wu, *Nat. Mater.* **2016**, *15*, 1120; b) M. Sumita, X. Yang, S. Ishihara, R. Tamura, K. Tsuda, *ACS Cent. Sci.* **2018**, *4*, 1126.
[241] C. Kunkel, C. Schober, J. T. Margraf, K. Reuter, H. Oberhofer, *Chem. Mater.* **2019**, *31*, 969.
[242] A. Govind Rajan, J. M. P. Martirez, E. A. Carter, *ACS Catal.* **2020**, *10*, 11177.
[243] J. M. Ripalda, J. Buencuerpo, I. García, *Nat. Commun.* **2018**, *9*, 5126.
[244] J. Greeley, J. K. Nørskov, *Surf. Sci.* **2007**, *601*, 1590.
[245] I. E. Castelli, D. D. Landis, K. S. Thygesen, S. Dahl, I. Chorkendorff, T. F. Jaramillo, K. W. Jacobsen, *Energy Environ. Sci.* **2012**, *5*, 9034.
[246] D. D. Landis, J. S. Hummelshøj, S. Nestorov, J. Greeley, M. Dułak, T. Bligaard, J. K. Nørskov, K. W. Jacobsen, *Comput. Sci. Eng.* **2012**, *14*, 51.
[247] W. T. Hong, R. E. Welsch, Y. Shao-Horn, *J. Phys. Chem. C* **2016**, *120*, 78.
[248] R. B. Wexler, J. M. P. Martirez, A. M. Rappe, *J. Am. Chem. Soc.* **2018**, *140*, 4678.
[249] K. Tran, Z. W. Ulissi, *Nat. Catal.* **2018**, *1*, 696.
[250] S. Back, K. Tran, Z. W. Ulissi, *ACS Catal.* **2019**, *9*, 7651.
[251] T. Xie, J. C. Grossman, *Phys. Rev. Lett.* **2018**, *120*, 145301.
[252] A. J. Cohen, P. Mori-Sánchez, W. Yang, *Chem. Rev.* **2012**, *112*, 289.
[253] M. J. Gillan, D. Alfè, A. Michaelides, *J. Chem. Phys.* **2016**, *144*, 130901.
[254] a) Y. Ping, D. Rocca, G. Galli, *Chem. Soc. Rev.* **2013**, *42*, 2437; b) Y. Li, Y.-L. Li, B. Sa, R. Ahuja, *Catal. Sci. Technol.* **2017**, *7*, 545.
[255] R. Nashed, W. M. Hassan, Y. Ismail, N. K. Allam, *Phys. Chem. Chem. Phys.* **2013**, *15*, 1352.
[256] Y.-N. Wu, L. Li, H.-P. Cheng, *Phys. Rev. B* **2011**, *83*, 144105.
[257] J. C. Grossman, E. Schwegler, E. W. Draeger, F. Gygi, G. Galli, *J. Chem. Phys.* **2004**, *120*, 300.
[258] a) R. A. DiStasioJr, B. Santra, Z. Li, X. Wu, R. Car, *J. Chem. Phys.* **2014**, *141*, 084502; b) H. L. Zhuang, R. G. Hennig, *Chem. Mater.* **2013**, *25*, 3232.
[259] J. Wang, G. Román-Pérez, J. M. Soler, E. Artacho, M.-V. Fernández-Serra, *J. Chem. Phys.* **2011**, *134*, 024516.
[260] a) A. K. Singh, K. Mathew, H. L. Zhuang, R. G. Hennig, *J. Phys. Chem. Lett.* **2015**, *6*, 1087; b) P. Niu, L. Zhang, G. Liu, H. M. Cheng, *Adv. Funct. Mater.* **2012**, *22*, 4763; c) C. Ataca, H. Sahin, S. Ciraci, *J. Phys. Chem. C* **2012**, *116*, 8983.
[261] a) A. Janotti, J. Varley, P. Rinke, N. Umezawa, G. Kresse, C. G. Van de Walle, *Phys. Rev. B* **2010**, *81*, 085212; b) J. Wróbel, K. J. Kurzydłowski, K. Hummer, G. Kresse, J. Piechota, *Phys. Rev. B* **2009**, *80*, 155124.
[262] W. Dawson, F. Gygi, *J. Chem. Theory Comput.* **2015**, *11*, 4655.
[263] a) A. V. Akimov, A. J. Neukirch, O. V. Prezhdo, *Chem. Rev.* **2013**, *113*, 4496; b) X. Ma, C. Chen, J. Hu, M. Zheng, H. Wang, S. Dong, C. Huang, X. Chen, *J. Alloys Compd.* **2019**, *788*, 1.
[264] M. Marsman, J. Paier, A. Stroppa, G. Kresse, *J. Phys.: Condens. Matter* **2008**, *20*, 064201.
[265] V. I. Anisimov, F. Aryasetiawan, A. Lichtenstein, *J. Phys.: Condens. Matter* **1997**, *9*, 767.
[266] J. H. Skone, M. Govoni, G. Galli, *Phys. Rev. B* **2014**, *89*, 195112.
[267] N. J. Mosey, P. Liao, E. A. Carter, *J. Chem. Phys.* **2008**, *129*, 014103.
[268] K. Yang, B. Yang, *Faraday Discuss.* **2021**, *229*, 50.
[269] B.-J. Ng, L. K. Putri, L.-L. Tan, P. Pasbakhsh, S.-P. Chai, *Chem. Eng. J.* **2017**, *316*, 41.
[270] Q. Wang, T. Hisatomi, Y. Suzuki, Z. Pan, J. Seo, M. Katayama, T. Minegishi, H. Nishiyama, T. Takata, K. Seki, *J. Am. Chem. Soc.* **2017**, *139*, 1675.
[271] V. Atalla, M. Yoon, F. Caruso, P. Rinke, M. Scheffler, *Phys. Rev. B* **2013**, *88*, 165122.

Jamal Abdul Nasir obtained his M.Sc. and M.Phil. degree in Inorganic/Analytical Chemistry from Quaid-i-Azam University, Islamabad, Pakistan in 2014 and 2016, respectively. He joined the same institute as a Ph.D. student in September 2016 and completed his research under the supervision of Dr. Zia-ur-Rehman. He has published several research articles in well-reputed journals. Currently, he is a part of Prof. Richard Catlow's group at UCL. His research interests are in the field of the chemistry of complex materials, including those for applications in photocatalytic and energy/environmental areas, investigated by a combination of computational and experimental techniques. He holds a keen interest in the field of computational modeling employing DFT and using hybrid QM/MM methodology for inorganic-based materials to investigate important reaction mechanisms.

Akhtar Munir did his M.Sc./M.Phil. from Quaid-I-Azam University of Islamabad (2012–2016) and Ph.D. from Lahore University of Management Sciences (LUMS) under a fully-funded scholarship. Since last year, he is working as an assistant professor in the department of chemistry (acting HOD), University of Sialkot (USKT). He is interested in the chemical and electrical aspects of energy and sustainability. During his Ph.D., he mainly focused to develop facile and scalable protocols for the synthesis of transition metal (Ni, Cu, Co, Fe, and Mn) nanoclusters/nanomaterials (size ≈ 2 nm), their alloys/thin films, and surface assembling on various conducting support (graphene, CNTs, TiO_2, Au, and porous materials) for photo/electro-assisted water splitting. He has a very decent research background with research published in well-reputed journals.

Naveed Ahmad received his Pharm. D and M.Phil. degree in Pharmacy from the University of Malakand, Chakdara Dir Lower, Khyber Pakhtunkhwa, Pakistan, in 2012 and 2015, respectively. He has a decent research background in the field of pharmaceutical and material sciences and published worthy research articles in international journals of well repute. Currently, he is working towards a Ph.D. at the Institute of Pharmaceutical Sciences, King's College, London, UK. He holds a keen research interest in material sciences especially polymers and nanoparticles for biomedical, energy, and environmental applications.

Tanveer ul Haq received his B.S. (Hons.) in 2016 from the University of Sargodha and master's degree from the Lahore University of Management and Science (LUMS), Lahore, in 2018 with chemistry as the major subject. His master thesis was focused on the development of nanocluster for photo/electrochemical water splitting. He joined the same institute as a Research Assistant in July 2018. Since 2019, he is a Ph.D. student in the group of Prof. Yousef Haik at Texas A&M University-Kingsville. His current research interest includes engineering functional self-supported nanomaterials for seawater electrolysis and direct methanol fuel cell. He has published over 13 research articles in various journals of international repute. He has been awarded a merit scholarship (LUMS) and Dean's Honor award (LUMS).

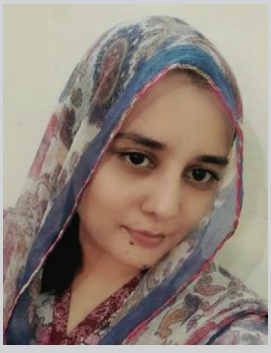

Zaibunisa Khan received her M.Sc. and M.Phil. degree in Inorganic/Analytical Chemistry from Quaid-i-Azam University, Islamabad, Pakistan, in 2016 and 2018, respectively. She joined Prof. Jawwad Arshad Darr's Clean Materials Technology Group (CMTG), University College London as a Ph.D. student in 2021. She has published several research articles in various international journals. She has expertise in the synthesis of novel materials for biomedical, batteries, and energy applications.

Zia-ur-Rehman is working as a Professor at Quaid-i-Azam University, Islamabad, Pakistan. His group is involved in the synthesis of new materials for biomedical, clean energy production and storage, and environmental applications. He has published more than 140 research articles in various journals of international repute, and is a co-author of a book entitled "DNA Binding and DNA Extraction: Methods, Applications, and Limitations." In his short academic carrier, 9 Ph.D. and 42 M.Phil. students obtained their degrees in his direction. His teaching and research efforts have been recognized by the Dr. Abus Salam Award from TWAS and Pakistan Academy of Sciences (PAS), Dr. Atta-ur-Rahman Gold Medal (PAS), and CSP Gold Medal (The Chemical Society of Pakistan). He is a young member of the PAS and International Committee Member of ACCC.